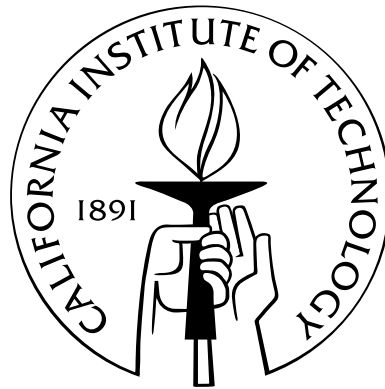# Mechanics of Viscoelastic Thin-Walled Structures

Thesis by

Kawai Kwok

In Partial Fulfillment of the Requirements

for the Degree of

Doctor of Philosophy

California Institute of Technology

Pasadena, California

2013

(Defended May 24, 2012)

Acknowledgements

First and foremost, I am deeply indebted to my parents, Hon Yuen Kwok and Wai Ying Chan, my sister Man Fong Kwok, and my fiancee Kei Yau Sin, for their unconditional support and trust. They have always encouraged me to pursue my dreams. They are always by my side even though we are physically apart.

The research work presented in this thesis would not have been possible without the guidance of my advisor, Professor Sergio Pellegrino. He has demonstrated many good examples of research practices to me. I am especially impressed by his close attention to details, emphasis on clarity of arguments, and effectiveness in explaining complicated ideas in a physical and intuitive manner.

I am grateful for the valuable comments and suggestions from the members of my thesis and candidacy committees, Professors Guruswami Ravichandran, Kaushik Bhattacharya, Chiara Daraio, Jose Andrade, and Dennis Kochmann. I need to specially thank Professor Wolfgang Knauss for sharing with me his knowledge and experience on theoretical and experimental aspects of viscoelasticity.

My gratitude goes to Dr. James Rand (Winzen Engineering) and Dr. David Wakefield (Tensys) for their constructive comments regarding the work on balloon film modeling. I also need to extend my appreciation to Gary Patz (Patz Materials Technologies) for providing materials for my study on viscoelastic composites.

I would like to thank Dr. Laurence Bodelot for taking me through the setup of digital image correlation. I am amazed by her rigor in experimental science. I am thankful to Petros Arakelian for his technical expertise and assistance in many of my experimental setups. I have learned many hands-on skills from him.

My colleagues and friends at Caltech have made my life much easier. They are always there to help me with any difficulties. I need to particularly mention Chinthaka Mallikarachchi, Francisco Lopez Jimenez, Tobias Gerngross, Xiaowei Deng, Keith Patterson, John Steeves, Markus Schatz, Michio Inoue, Adrianus Indrat Aria, and Esperanza C. Linares Guerrero.

Finally, I would like to express my sincere appreciation to the Croucher Foundation in Hong Kong for granting me a doctoral fellowship. This research is also funded by the NASA Balloon Program Office and the Northrop Grumman Corporation. Their support is gratefully acknowledged.

Abstract

Thin-walled structures made of polymers and reinforced polymer composites are prominent candidates for constructing large lightweight structures. A major challenge in designing polymer-based thin-walled structures is their time and temperature dependent behavior originating from material viscoelasticity and its interaction with the highly geometrically nonlinear response due to thinness of the walls. Although polymer viscoelasticity and geometric nonlinearity have been extensively studied, the mechanics of structures exhibiting both phenomena are not well understood.

This thesis presents a combination of experimental, numerical, and analytical investigations of the behavior of viscoelastic thin-walled structures. The first goal of this research is to establish general methods of analysis for two types of structural components, namely composite shells and polymer membranes, that will serve as the basis for full-scale structural analysis. The second goal is to demonstrate the capability of the developed methods by analyzing time and temperature dependent behavior of deployable structures and balloon structures.

In the study of deployable structures, the deployment and shape recovery processes after stowage are investigated. Fundamental features of viscoelastic deployable structures are studied first with homogeneous polymer beams and shells. A simple closed-form solution describing the shape evolution of a beam after stowage is proposed. The effects of rate and temperature on the bending instability of shells are revealed. Building on the understanding gained from the analysis of homogeneous structures, modeling techniques are developed for polymer composite structures. A micromechanical viscoelastic model for carbon fiber reinforced polymer thin shells is established through finite element homogenization and applied to evaluate the effects of long-term stowage in a representative composite deployable structure.

In the study of balloon structures, a membrane model is developed to study polymer balloon films with stress concentrations due to thickness variation. A nonlinear viscoelastic constitutive model is first formulated for the film material. The wrinkling instability behavior is incorporated into the model through correction of stress and strain states in the presence of wrinkling. Stress concentration factors in balloon films are predicted and measured with the membrane model and full-field displacement measurement techniques, respectively.

Contents

List of Figures

List of Tables

Chapter 1

Introduction

1.1 Polymer and Composite Thin-walled Structures

Thin-walled structures are three-dimensional objects in which one dimension is much smaller than the other two. Because of their structural efficiency, thin-walled structures are widespread in many branches of engineering with areas of applications ranging from aircrafts, ships, and space vehicles to bridges, buildings, and storage vessels. A growing proportion of thin-walled structures is made of polymers and reinforced polymer composites, most notably in the construction of large lightweight structures, because of the significant weight benefits. Two outstanding types of such kind are composite shell structures and polymer membrane structures.

Composite shells are made from two or more constituent materials which are distinct at the microscopic scale. The most widely used composite shells are fiber reinforced polymer composites in which stiff reinforcing fibers are embedded in a polymer matrix. Common fiber reinforcements include carbon and glass fibers. For matrix material, thermosetting polymers such as epoxy are usually chosen due to their higher mechanical and thermal stability, even though there are renewed interests in thermoplastic matrix recently. Remarkable examples of fiber reinforced composite shell structures include the fuselage of Boeing 787 Dreamliner aircraft shown in Figure 1.1, and the lightweight deployable booms used by the German Aerospace Center (DLR) to unfold large solar sails, Figure 1.2.

Polymer membranes often appear in either fabric or film form. Nylon, polyester, and polyethylene are common materials for manufacturing membranes. The area of application is primarily in inflatable structures such as aerostats, airships, balloons, and radomes. The 30 m diameter sea-based inflatable radome in Figure 1.3 and the tethered aerostat with a volume of 11,893 m^3 shown in Figure 1.4 are two examples of polymer membrane structures.

The structures mentioned above are designed for long duration operation, during which temperature variations will occur. Whether a structure can perform its desired function under such conditions is in question because the polymeric materials that make up the structure have viscoelas-

tic properties that vary with time and temperature.

The design of viscoelastic thin-walled structures pose significant challenges in analysis because both geometry and material behavior play a key role. In particular, their response is highly geometrically nonlinear due to the thinness of the walls; and sensitive to time and temperature change as a result of the viscoelastic nature of polymers.

Figure 1.1. Carbon fiber composite fuselage section (courtesy of Boeing).

Figure 1.2. Composite deployable booms: (a) Snapshots during deployment, and (b) solar sail unfolded by four deployable booms (courtesy of DLR).

Figure 1.3. Sea-based inflatable radome (courtesy of ILC Dover).

Figure 1.4. Tethered aerostat (courtesy of ILC Dover).

1.2 Motivation

The research presented in this thesis is motivated by recent developments in space structures and balloon structures that are made of thin composite laminates and polymer films, respectively. Specifically, the focus is on long-term stowage effects in deployable spacecrafts and stress concentrations in superpressure balloons. These two problems have notable similarities in the theoretical, experimental, and computational tools required.

1.2.1 Stowage Effects in Deployable Spacecraft

For designing large space structures such as reflectors, antennas, and solar sails, the payload and stowage capacity of launch vehicles are the main limiting factors. A routinely employed solution is to design large space structures as deployable structures which can be packaged into a much smaller volume for stowage and deployed in space for operation. Inflatables, motorized and mechanically jointed structures, elastically deformed structures, and structures with shape memory are common packaging and deployment schemes.

Packaging a structure by recoverable deformation is a particularly attractive solution because the structure is able to self-deploy upon releasing the packing constraint. Thin shell structures are extensively used for this packaging scheme because they can undergo large shape reconfiguration with relatively small deformation by virtue of geometrically nonlinear behavior. To increase mass efficiency, there is rising interest in designing deployable structures with fiber reinforced polymer composite materials (Yee and Pellegrino, 2005; Soykasap et al., 2008). Notable examples of composite deployable structures include the Springback Antennas on the Mobile Satellite System (Seizt, September 4, 1994) and the Flattenable Foldable Tubes forming the Mars Advanced Radar for Subsurface and Ionospheric Sounding (MARSIS) antenna on the Mars Express Spacecraft (Mobrem and Adams, 2009). The antenna consisted of two 20 m dipoles and a 7 m monopole. Slots were introduced into the antenna tubes at several intervals for packaging and stowage in a 1.7 m x 0.3 m x 0.2 m cradle as shown in Figure 1.5.

One important issue in designing composite deployable structures is the inherent creep behavior of the polymer matrix, which often limits the amount of deployment force and the shape precision that can be achieved. The MARSIS antenna, for instance, was found to have a reduction in deployment moment after a long period of stowage (Adams and Mobrem, 2009). As space structures are often stowed for extended periods and subject to varying temperature environments, realistic predictions on, for instance, the loss in deployment force during stowage and the time required for a complete shape recovery are required for robust designs. It is necessary to gain a fundamental understanding of the viscoelastic behavior of the structure during the folding, stowage, deployment, and shape recovery processes.
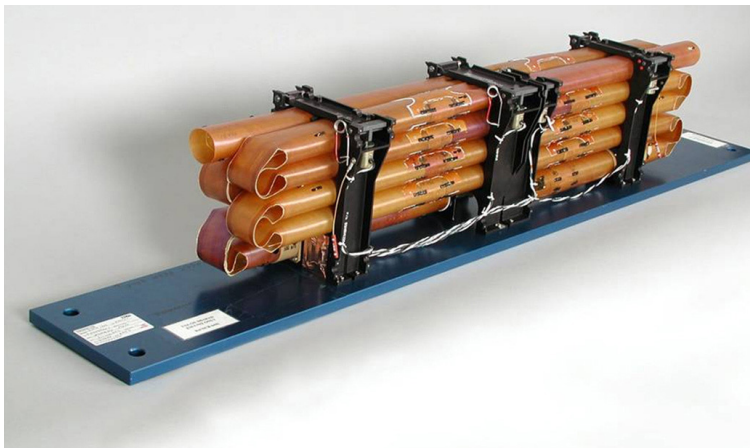
Figure 1.5. Flattenable foldable tubes used on MARSIS (courtesy of Astro Aerospace).

1.2.2 Stress Concentrations in Superpressure Balloons

Balloon systems provide a potential low-cost platform for telecommunication and scientific observation in the stratosphere. However, no balloon systems today are able to carry large payloads for long duration. The Superpressure Balloon (SPB) program started by NASA, originally known as Ultra Long Duration Balloon program, aims to develop a general purpose platform that can carry payloads of several tonnes for up to 100 days at constant altitudes above 99% of the Earth's atmosphere (Smith, 2004).

Zero-pressure balloons which have an opening at the bottom are not able to maintain a constant altitude because the volume of the balloon is free to expand and contract as a result of heating and cooling of the gas inside the balloon during the day-night cycle. To minimize altitude variation, lobed superpressure balloons with a closed envelope are currently employed for SPB. The balloon is assembled from a number of identical gores by sealing neighboring lobes together and incorporating a tendon along the common boundary in the meridional direction as shown in Figure 1.6. The tendons are hollow-braided cords made of high strength fibers intended for carrying meridional stress. Hoop stress is primarily taken up by the polymer gore films and can be reduced by increasing the local lobe curvature. This design has the advantage of decreased self-weight by using thin membranes to construct the lobes (Smith and Rainwater, 2004).

A limiting factor in designing these balloons is the presence of local stress concentrations in relatively small regions of the balloon film, for example, at the junction of the end-fitting and the balloon film. To enable the estimation of realistic factors of safety, the actual stress concentrations in these regions need to be predicted, which requires a detailed understanding of the balloon film behavior. The balloon film is made of linear low density polyethylene (LLDPE) with thicknesses ranging from 20 μm to 38 μm. This film exhibits nonlinear viscoelastic and anisotropic behavior
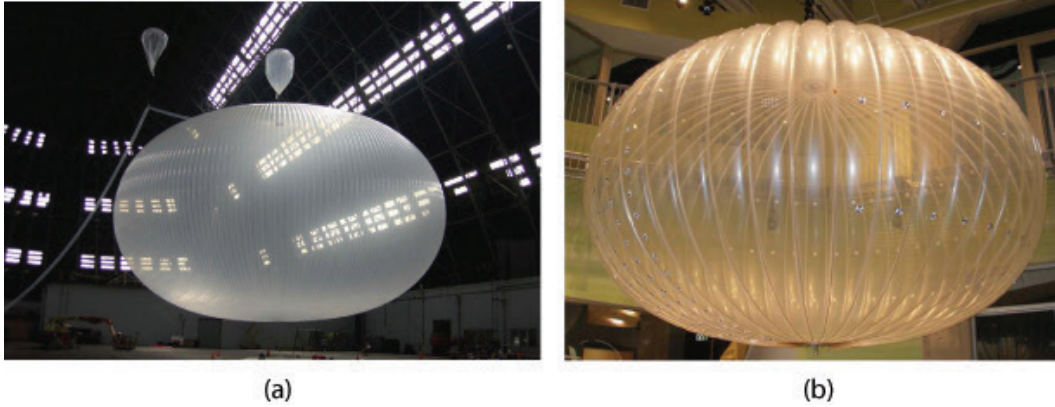
Figure 1.6. Lobed superpressure balloon: (a) inflated configuration during indoor test (courtesy of NASA), and (b) laboratory scale model.

(Rand and Sterling, 2006), and is prone to wrinkling due to its small thickness. Accounting for these effects and their interaction in design analysis is critical for successful balloon flights.

1.3 Objectives

The overall objective of this thesis is to establish general methods of analysis to understand time and temperature dependent behavior of large thin-walled structures. The first goal of this research is to develop analytical, experimental, and modeling techniques for composite shells and polymer membranes that will serve as the basis for full-scale analysis of thin-walled structures exhibiting viscoelastic behavior. The second goal is to to investigate stowage effects in a representative composite deployable structure and stress concentrations in balloon films used in NASA superpressure balloons with the developed techniques.

1.4 Organization

This thesis is comprised of several self-contained studies performed on different types of viscoelastic thin-walled structures. The organization is intended to present the techniques and results specific to the topic at hand.

The detailed outline of the thesis is as follows. Chapter 2 reviews the essential elements in polymer viscoelasticity and provides an overview of the theoretical, experimental, and numerical tools relevant to the current research.

Chapters 3 to 5 are designated to studies on deployable structures. Each of them is focused on a specific aspect of the general problem. To understand the general features of viscoelastic deployable structures, the folding, stowage, deployment, and recovery sequence of a homogeneous

polymer beam is formulated as a quasi-static time-dependent boundary value problem and solved analytically in Chapter 3. This study provides insight into the effects of stowage temperature and duration. Chapter 4 investigates the behavior polymer tape-springs, which are cylindrical shells that often used as deployable actuator elements. The effects of rate and temperature on their highly geometrically nonlinear behavior are studied. Chapter 5 is focused on micromechanical modeling of woven composite shells and its application on dynamic deployment and shape recovery of composite tape-springs.

Chapter 6 is devoted to the study of superpressure balloons. A membrane model that captures both the anisotropic, nonlinear viscoelastic material behavior, as well as the wrinkling response of the LLDPE balloon film is presented. The free volume nonlinear viscoelasticity theory is generalized for orthotropic membranes. A wrinkling criterion and a correction algorithm for stress and strain states due to the presence of wrinkles are incorporated into the viscoelastic model in finite element implementation. Experiments and simulations based on the developed model are performed to study a problem in which stress concentrations arise in the balloon film.

Chapter 7 concludes the thesis.

Chapter 2

Polymer Viscoelasticity

The viscoelastic behavior exhibited by the structures studied in this thesis originates from the response of the constituent polymer materials. This chapter describes the general mechanical characteristics of polymers and provides an overview of the theoretical, experimental, and numerical tools employed.

2.1   Mechanical Properties of Solid Polymers

Most solid polymers can be broadly classified into either thermoplastics or thermosets. The basic physical difference between the two is related to the bonding between molecular chains. Thermoplastics only have secondary bonds between chains while primary bonds exist between chains in thermosets. Because of differences in the molecular structures, the two types of polymers exhibit different material behavior. Generally speaking, thermoplastics can be repeatedly melted and remolded while thermosets cannot. Thermoplastics and thermosets are sometimes referred to as uncrosslinked and crosslinked, respectively.

The mechanical properties of polymers are dependent on rate and temperature. If uniaxial tests are performed under various constant strain rates and temperatures, stress-strain response similar to Figure 2.1 will be observed. The rate and temperature dependence of the stress-strain response is typical of many polymers. As seen in Figure 2.1, polymers have increased stiffness at faster rates or lower temperatures. Such mechanical response is a result of the unique deformation mechanism of the molecular structure. When subject to a load, a polymer responds not only by bond stretching (as in the case of metals), but also by molecular chain rearrangement to bring the macromolecular structure to a state of energy minimum. Bond stretching is relatively fast while chain rearrangement is a long-term process. At fast loading rates, polymers deform mostly by bond stretching and the observed stiffness is therefore higher. Chain reconfiguration is heavily influenced by chain mobility. At high temperatures, the volume of a polymer expands, which creates more room for molecular chains to reconfigure. The rearrangement process is sped up due to higher chain mobility, which

leads to a lower observed stiffness.

A polymer can be stiff like glass or flexible like rubber depending on its temperature as compared to the characteristic temperature known as the glass transition temperature T_g. Below the T_g, polymers are glassy solids with only a small amount of time-dependence. Near and slightly above the T_g, polymers become more viscoelastic and their moduli drastically decrease with time. This regime is often known as the transition region. As the temperature is raised well above the T_g, polymers exhibit rubbery like behavior. In the rubbery region, little time-dependence is again observed, but the modulus is significantly lower than the glassy modulus.

The glass transition temperature for different polymers span a wide range from well below to well above ambient temperature. Therefore, it is not unusual that two different polymers show dissimilar behavior at room temperature because they may either be in the glassy or rubbery regime. Thermoplastics are generally lighter, softer, and have lower glass transition temperatures than thermosets. They are used in engineering devices where low stresses are expected. For higher thermal and dimensional stability requirements, thermosets are employed. For instance, the LLDPE used in NASA superpressure balloons is a thermoplastic with a glass transition of approximately -50$°C$ while the epoxy resin in composite deployable structures studied in this thesis is a thermoset with a glass transition temperature of 130$°C$.
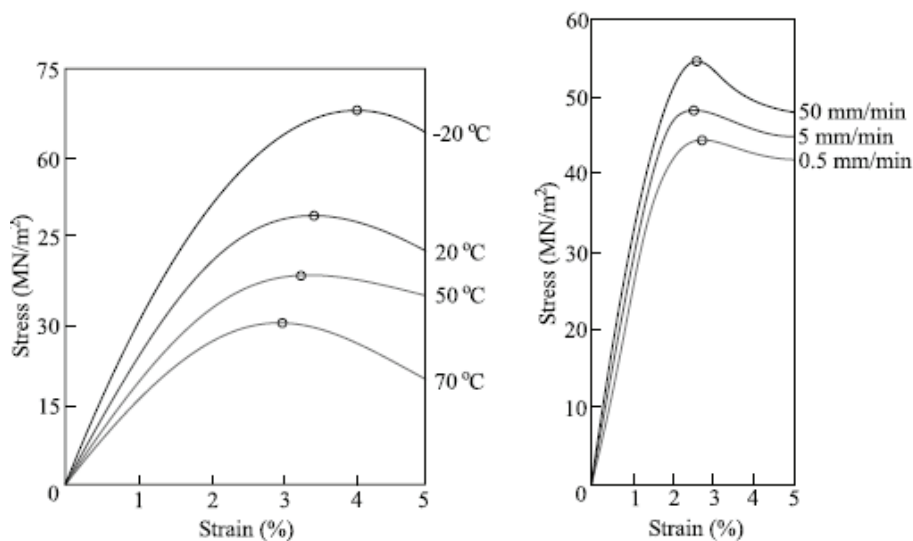
Figure 2.1. Typical stress-strain response for polymers (Brinson and Brinson, 2008).

2.2   Review of Phenomenological Theory

Even though it has been mentioned that the fundamental nature of viscoelastic behavior originates from unique molecular mechanisms in polymers, modeling molecular deformation is a complicated

task and still a subject of current research. For analysis of large structures such as those studied in this thesis, a phenomenological theory provides a satisfactory approximation.

The phenomenological theory of viscoelasticity is well established (Coleman and Noll, 1961; Flugge, 1975; Ferry, 1980; Christensen, 1982; Tschoegl, 1989). This section describes the definition of terms and outlines the basic principles involved in the theory.

2.2.1 Relaxation and Creep

The two fundamental attributes of viscoelastic behavior are relaxation and creep. In relaxation, a constant strain is applied to a specimen in a quasi-static manner at zero time. The stress required to maintain the imposed strain decreases over time. Eventually, the stress reduces to zero for uncrosslinked polymers but converges to a constant value for crosslinked polymers. The typical stress and strain profiles during relaxation are shown in Figure 2.2(a). The modulus obtained from such stress and strain variations is obviously a function of time and is defined as the relaxation modulus $E(t)$,

$$E(t) = \frac{\sigma(t)}{\epsilon_1}. \tag{2.1}$$

If instead a constant stress is applied, the strain will increase over time as shown in Figure 2.2(b). This situation is the inverse of relaxation and is known as creep. The creep compliance $D(t)$ so obtained is given by

$$D(t) = \frac{\epsilon(t)}{\sigma_1}. \tag{2.2}$$
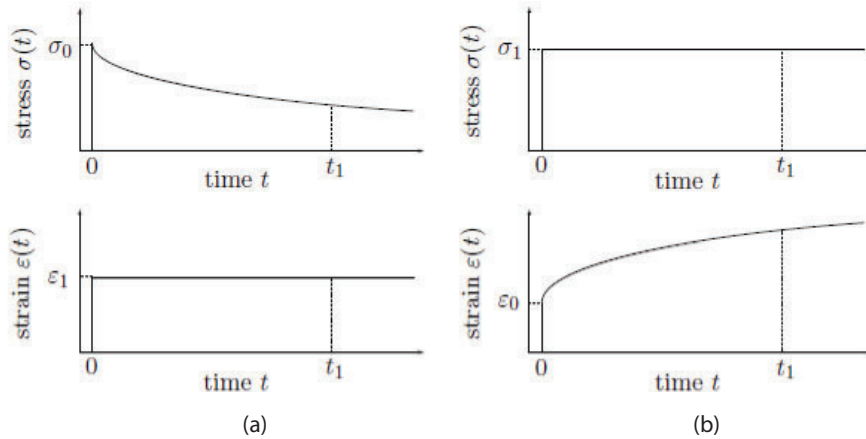
Figure 2.2. Stress and strain evolution over time in (a) relaxation, and (b) creep.

2.2.2 Boltzmann Superposition Principle

Relaxation and creep are relatively simple scenarios where either a constant strain or stress is applied. For problems with variable stress or strain inputs, the Boltzmann superposition principle is applicable. Consider the case of imposing an arbitrary time-varying strain to a polymer. The imposed strain profile is first thought of as a series of step strain inputs. Since the strain is constant within each step, the resulting effect in each step is represented by a relaxation response. It is assumed in the Boltzmann superposition principle that the relaxation responses are linearly independent and can therefore be superposed to give the final stress response (McCrum et al., 2003). The same holds for the case of applying a time-varying stress. The result of this principle is an integral representation for viscoelastic constitutive relations written as

$$\sigma(t) = \int_0^t E(t-s)\frac{d\epsilon(s)}{ds}ds, \tag{2.3}$$

$$\epsilon(t) = \int_0^t D(t-s)\frac{d\sigma(s)}{ds}ds. \tag{2.4}$$

2.2.3 Prony Series Representation

For practical stress analysis, it is necessary to know the actual viscoelastic properties of the materials. Hence a mathematical representation of the experimental data obtained from relaxation or creep tests is needed. The most frequently used mathematical form is an exponential series often referred to as a Prony series (Brinson and Brinson, 2008). The Prony series representation for relaxation modulus $E(t)$ or creep compliance $D(t)$ are given by

$$E(t) = E_\infty + \sum_{i=1}^{n} E_i e^{-t/\rho_i}, \tag{2.5}$$

$$D(t) = D_0 + \sum_{j=1}^{n} D_j(1 - e^{-t/\tau_j}), \tag{2.6}$$

where E_∞ is the long-term modulus, E_i are the relaxation coefficients, ρ_i are the relaxation times, D_0 is the instantaneous compliance, D_j are the retardation coefficients, τ_j are the retardation times. The Prony series can be derived from a mechanical model consisting of a network of springs and dashpots as shown in Figure 2.3. In this model, the elastic response is represented by the springs with spring constants E_i and the viscous response is provided by the dashpots with viscosity μ_i. Each leg of spring and dashpot gives rise to one exponential, which effectively models the time-dependent behavior within 1 decade of time. Exponential terms can be added or removed depending on the time span of interest. Figure 2.4 shows the typical behavior of relaxation modulus and creep compliance with respect to logarithmic time.
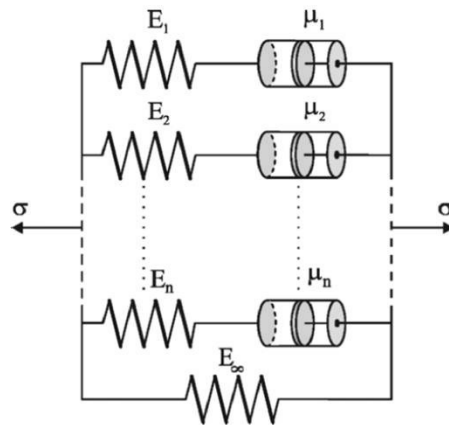
Figure 2.3. Mechanical model of Prony series (Brinson and Brinson, 2008).
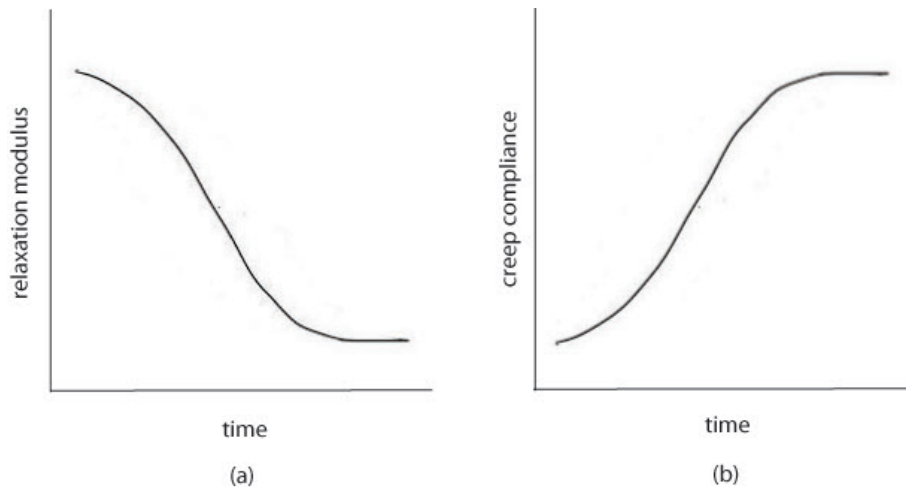
Figure 2.4. Typical viscoelastic property variation with time: (a) relaxation modulus, and (b) creep compliance.

2.2.4   Time-Temperature Superposition Principle

A particularly important function of engineering design is the ability to predict the performance of structures over their lifetime, which can range from several months for superpressure balloons to years for space structures. There is a huge advantage if methods of analysis are capable of predicting long term response of polymer-based structures from relatively short-term test data. For polymers, there exists a remarkable relationship between the dependence on time and temperature known as the time-temperature superposition principle.

To illustrate the time-temperature superposition principle, consider a creep compliance curve shown in Figure 2.5. If short-term creep tests are carried out at several temperatures, creep data similar to Figure 2.5(a) will be observed. The compliance curve in Figure 2.5(b) is obtained by shifting all curves above $-10°C$ to the right and those below $-10°C$ to the left in Figure 2.5(a) until a continuous line appears. Essentially, the data collected above $-10°C$ represent the longer time creep response at $-10°C$ while data below $-10°C$ represent the shorter time response. The total curve in Figure 2.5(b) is called the creep compliance master curve at $-10°C$. To obtain the master curve at a different temperature, the curves can be shifted with respect to the desired temperature. With this principle, the viscoelastic response for a wide time span can be determined by performing short-term tests for a range of temperatures.

The theoretical basis for time-temperature superposition principle is the kinetic theory of polymers, which has been extensively studied. The key result related to time-temperature superposition principle is the postulation of a shift factor a_T which expresses the ratio of relaxation times (or retardation times) at two different temperatures,

$$a_T = \frac{\rho(T)}{\rho(T_0)},$$
(2.7)

where ρ is the relaxation time and T_0 is some reference temperature. As indicated earlier, a polymer has many relaxation times. If the same shift factor applies to all relaxation times, the polymer is termed thermorheologically simple. A widely used empirical relation for a_T is called the Williams-Landel-Ferry (WLF) equation (Williams et al., 1955),

$$\log a_T = -\frac{c_1(T - T_0)}{c_2 + (T - T_0)},$$
(2.8)

in which c_1 and c_2 are material constants that depend on the particular polymer and the logarithm is of base ten.

To incorporate this temperature behavior into the integral constitutive equation, the concept of reduced time t' is introduced and is given by,

14

$$t' = \int_0^t \frac{ds}{a_T(T(s))}. \tag{2.9}$$

In the simple case of constant temperature over time, the reduced time becomes

$$t' = \frac{t}{a_T}, \tag{2.10}$$

and the following relations are obtained:

$$E_T(t) = E_{T_0}(t'), \tag{2.11}$$

$$D_T(t) = D_{T_0}(t'). \tag{2.12}$$

In other words, the relaxation modulus or creep compliance at one temperature is related to that at the reference temperature by a shift in time, which justifies the curve shifting procedure in forming the master curve illustrated earlier.

The constitutive equations, Equations 2.3 and 2.4 , are expressed in terms of reduced time as

$$\sigma(t) = \int_0^t E(t' - s') \frac{d\epsilon(s)}{ds} ds, \tag{2.13}$$

$$\epsilon(t) = \int_0^t D(t' - s') \frac{d\sigma(s)}{ds} ds. \tag{2.14}$$
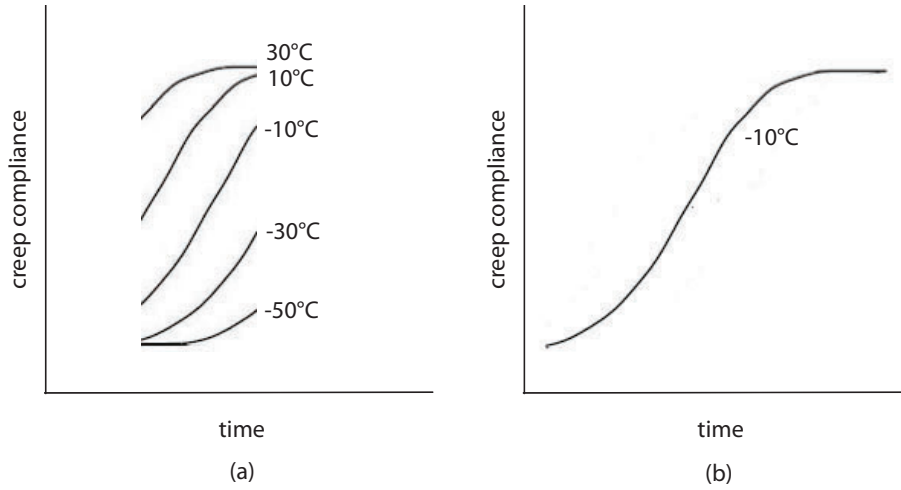
Figure 2.5. Creep compliance master curve: (a) short term creep data, and (b) shifted data.

The applicability of time-temperature superposition over long time scales has been studied by Capodagli and Lakes (2008). This study investigated the viscoelastic properties of PMMA and LDPE over 11 decades of time and reached the conclusion that time-temperature superposition is

acceptable for modulus curves, but not for damping curves. The sensitivity of the shift process with respect to thermal variations was studied by Knauss (2008). Results of the study showed that a one degree centigrade variation around a mean value limits the shift factor error to less than 4%, which translates into a misrepresentation of two weeks out of a year.

2.2.5 Multiaxial Behavior

The constitutive behavior of viscoelastic materials discussed so far has been limited to the case of uniaxial deformation. This section describes the equations, assumptions, and procedures employed in solving boundary value problems in two or three dimensions.

For isotropic materials, the constitutive equations can be written in terms of deviatoric and dilatational stress and strain components,

$$d_{ij}(t) = 2 \int_0^t G(t' - s') \frac{\partial e_{ij}(s)}{\partial s} ds \tag{2.15}$$

$$\sigma_{kk}(t) = 3 \int_0^t K(t' - s') \frac{\partial \epsilon_{kk}(s)}{\partial s} ds \tag{2.16}$$

where d_{ij} and e_{ij} are the deviatoric stress and strain, σ_{kk} and ϵ_{kk} are the dilatational stress and strain, G is the shear modulus and K is the bulk modulus. In practice, it is difficult to measure the viscoelastic bulk modulus because it varies with time only by a small amount. Therefore the usual practice is to infer the bulk modulus from Young's modulus and Poisson's ratio. Although such interconversion of material functions are routinely performed in elasticity, their implementation in viscoelastic solids present nontrivial theoretical and experimental difficulties due to the time-dependent nature of the viscoelastic Poisson's ratio.

In viscoelastic materials, the Poisson's ratio is not uniquely defined and most definitions presented in the literature are not compatible with each other (Hilton, 1998). A frequently cited definition of viscoelastic Poisson's ratio is the ratio of time-dependent transverse to time-dependent longitudinal strain in axial creep extension,

$$\nu(t) = -\frac{\epsilon_t(t)}{\epsilon_l(t)}, \tag{2.17}$$

where ϵ_t and ϵ_l are transverse and longitudinal strains. For comparison, the Poisson's ratio defined under relaxation conditions is

$$\nu(t) = -\frac{\epsilon_t(t)}{\epsilon_l}, \tag{2.18}$$

in which the applied longitudinal strain, ϵ_l, is restricted to be time-independent. As shown in Lakes (2006), the Poisson's ratios in creep and relaxation can be expressed as

$$\nu_c(t) = \frac{1}{2} - \frac{1}{6}B\frac{1}{D(t)}, \tag{2.19}$$

$$\nu_r(t) = \frac{1}{2} - \frac{1}{6}BE(t), \tag{2.20}$$

where ν_c is the Poisson's ratio in creep, ν_r is the Poisson's ratio in relaxation, and B is the bulk compliance taken to be constant. It is observed that the two definitions are in general different because

$$E(t) \neq \frac{1}{D(t)}. \tag{2.21}$$

Alternatively, the Poisson's ratio can be defined as the ratio of the Fourier transforms of the time-dependent strains, even though this does not admit a direct physical interpretation.

For simplicity of calculation, a time-independent Poisson's ratio is often assumed. A constant Poisson's ratio tacitly leads to the condition that shear and bulk moduli are synchronous (i.e., proportional), which is inconsistent with the behavior of real materials. Hilton (2001) also suggested that a constant Poisson's ratio is only valid for analysis of homogeneous materials at constant temperatures.

The experiment difficulty in converting material functions lies in the high precision required in property characterization tests. For example, it has been reported that the Poisson's ratio must be determined to four significant digits in order to reasonably infer the bulk modulus (Lu et al., 1997; Sane and Knauss, 2001). In general, viscoelastic properties in polymers depend on temperature, moisture, specimen preparation and conditioning. Therefore the material functions being sought need to be measured on the same specimen, in the same environment, and at the same time (Tschoegl et al., 2002). Because of experimental difficulties in measuring two material functions simultaneously, the assumption of constant Poisson's ratio is frequently made for isotropic materials despite the fact that the resulting material model may not describe real material behavior.

It is agreed that values of Poisson's ratios obtained depend on the type of tests conducted and should be used with caution. A more accurate approach is to avoid material function conversion and determine directly the relaxation or creep functions.

For anisotropic materials, the constitutive equations formulated in terms of creep compliance are

$$\epsilon_{ij}(t) = \int_0^t D_{ijkl}(t' - s')\frac{d\sigma_{kl}(s)}{ds}ds, \tag{2.22}$$

where D_{ijkl} is the relaxation modulus matrix. The use of Poisson's ratio has no advantage in this case as the material characterization procedure requires more than a single experiment. Direct measurements of entries in D_{ijkl} provide a complete material description and the controversy with Poisson's ratio can be avoided.

2.3   Experimental Characterization

The basic test configuration, procedure, and data analysis methods for uniaxial relaxation modulus or creep compliance characterization are described in this section. Only the relaxation test procedure is presented for illustration. Additional test procedures or assumptions employed for specific materials will be discussed in the respective chapters.

2.3.1   Test Configuration and Procedure

Uniaxial tension tests with rectangular test coupons were performed inside an environmental chamber (Instron Heatwave Model 3119-506) utilizing a built-in thermocouple to control the temperature with a precision of $\pm 1^\circ C$, Figure 2.6. A type-T thermocouple made of Copper/Constantan was attached to the surface of a dummy specimen close to the test specimen to monitor the actual specimen temperature. As a test for stable temperature conditioning inside the environmental chamber, a temperature impulse was imposed and the subsequent temperature variation over time measured by the built-in thermocouple and the dummy specimen thermocouple were recorded. It was found that the temperature readings from the two thermocouples became identical 30 minutes after the impulse. This indicates that thermal equilibrium can be established within such time frame, and this thermal conditioning time was allowed prior to each test.

Prior to each test, the temperature was brought to the specified value after the specimen was clamped onto the materials testing machine. The specimen was thermally conditioned for 30 minutes at the test temperature. To make sure the specimen was not prestressed due to thermal expansion or contraction, the position of the crosshead of the load frame was adjusted to obtain a zero axial preload. Because of the viscoelastic nature of the specimen, the observed load on the specimen changes over time after each crosshead adjustment. Therefore, before an adjustment was made, the specimen was first allowed to rest until the observed load converged to a steady value. This step was repeated until a steady zero axial preload was eventually reached.

Relaxation tests were carried out at several different temperatures. At each temperature, test coupons were stretched to a strain of 0.005 in 1 second and held constant for 3 hours. The longitudinal and transverse strains were measured using two laser extensometers (Electronic Instrument Research Ltd LE-05) with a recording rate of 5 Hz for polymer sheet specimens. The laser extensometers measure the average strains over relatively large gage lengths. For film specimens which easily wrinkle under uniaxial tension, extensometers are not suitable because the transverse strains would be overestimated due to specimen wrinkling. For characterization of films, a three dimensional digital image correlation (DIC) system (Correlated Solutions Inc.) was employed. The DIC technique measures full-field strains on a surface arbitrarily oriented in three-dimensional space and hence avoids incorrect strain measurements.

Figure 2.6. Materials testing facility.

2.3.2 Data Analysis

The relaxation moduli at three different temperatures for low density polyethylene (LDPE) are shown in Figure 2.7 as an example. The initial portion of the relaxation test data after loading with a finite strain rate deviates from that in the case of ideal instantaneous straining. It has been demonstrated the difference becomes negligible in about 10 times the loading time (Lee and Knauss, 2000). For this reason, the data obtained during the first 10 s after loading were discarded. The individual relaxation moduli at $T = 0°C$ and $T = 10°C$ were shifted with respect to the reference temperature of $T_0 = 22°C$ to form a master curve. The corresponding shift factors were determined so that the shifted relaxation moduli and the unshifted one at T_0 lie along a single smooth curve. Figure 2.8 depicts the master curve of LDPE at the reference temperature. The long-term modulus, relaxation coefficients and relaxation times were determined by fitting the Prony series representation, Equation (2.5), to the experimental master curve using the Levenberg-Marquardt optimization algorithm (Levesque et al., 2007). In this fitting procedure, the long-term relaxation modulus was set to take the value at the end of the master curve. The number of Prony terms was chosen to be the same as the number of decades in time spanned by the master curve. The relaxation times could be fixed at equally spaced time intervals on the logarithmic scale, in which case only the Prony coefficients were computed, or left also as variables to be determined. Similarly, the material constants c_1 and c_2 were found by matching the temperature shift data to the WLF equation, Equation (2.8).

If creep compliance is desired for model formulation, it can be determined from the convolution relation between relaxation modulus and creep compliance,

$$\int_0^t E(t)D(t-s)ds = t. \tag{2.23}$$

2.4 Numerical Implementation

Finite element modeling is used extensively throughout this thesis. Hence, the material response needs to be computed in each time step during the solution procedure of a finite element structural analysis, which requires an integration over time and storage of information on the material states for all previous time steps. This section discusses an efficient recursive numerical algorithm that computes the constitutive integrals for viscoelastic materials.

A recursive algorithm was first proposed for linear viscoelastic integrals by Taylor et al. (1970). With this algorithm, only the material state variables at the previous time step are required for determining the current state. This approach minimizes the storage and arithmetic operations required to perform numerical integration. Similar algorithms have been extended to nonlinear
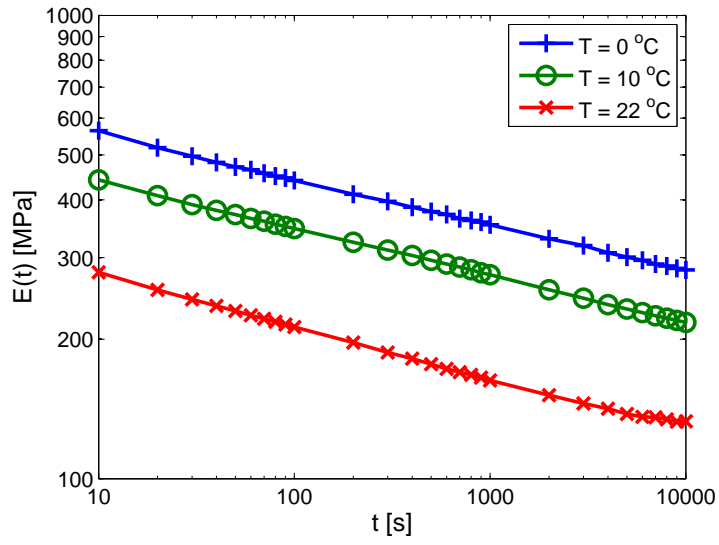
Figure 2.7. Relaxation test data for LDPE.
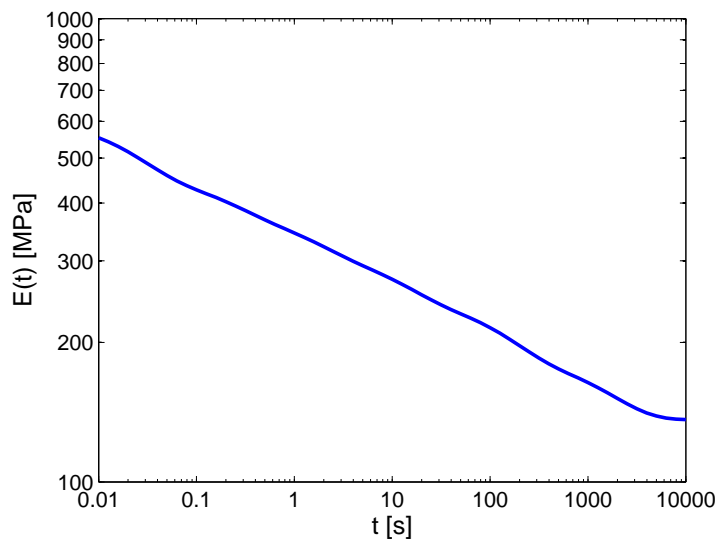
Figure 2.8. Relaxation modulus master curve.

viscoelastic integrals (Henriksen, 1984; Lai and Bakker, 1996; Haj-Ali and Muliana, 2004). Here the recursive algorithm for the case of linear viscoelastic uniaxial deformation is presented.

We begin by substituting the Prony series relaxation modulus, Equation 2.5 into the integral expression for current stress σ_t, Equation (2.13), to obtain

$$\sigma_t = E_\infty \epsilon_t + \sum_{i=1}^{n} E_i q_{i,t}, \tag{2.24}$$

where

$$q_{i,t} = \int_0^t e^{-(t'-s')/\rho_i} \frac{d\epsilon_s}{ds} ds. \tag{2.25}$$

The integral in Equation 2.25 can be divided into two parts. The first part is the integral from time zero up to the previous time step while the second is from the previous to the current time step. In other words,

$$q_{i,t} = \int_0^{t-\Delta t} e^{-(t'-s')/\rho_i} \frac{d\epsilon_s}{ds} ds + \int_{t-\Delta t}^t e^{-(t'-s')/\rho_i} \frac{d\epsilon_s}{ds} ds. \tag{2.26}$$

The first integral in Equation 2.26 can be expressed as

$$\int_0^{t-\Delta t} e^{-(t'-s')/\rho_i} \frac{d\epsilon_s}{ds} ds = e^{-\Delta t'/\rho_i} q_{i,t-\Delta t}, \tag{2.27}$$

where the reduced time increment is defined by

$$\Delta t' = \frac{\Delta t}{a_{T,t-\Delta t}}, \tag{2.28}$$

in which the shift factor is assumed to be constant over the current time step. Assuming that the strain varies linearly over the current time step, the second integral can be computed to be

$$\int_{t-\Delta t}^t e^{-(t'-s')/\rho_i} \frac{d\epsilon_s}{ds} ds = (\epsilon_t - \epsilon_{t-\Delta t}) \frac{1 - e^{-\Delta t'/\rho_i}}{\Delta t'/\rho_i}. \tag{2.29}$$

The integral $q_{i,t}$ can now be written as a recurrence relation with $q_{i,t-\Delta t}$

$$q_{i,t} = e^{-\Delta t'/\rho_i} q_{i,t-\Delta t} + (\epsilon_t - \epsilon_{t-\Delta t}) \frac{1 - e^{-\Delta t'/\rho_i}}{\Delta t'/\rho_i}. \tag{2.30}$$

By substituting Equation 2.30 into Equation 2.24, the current stress is finally expressed as

$$\sigma_t = E_\infty \epsilon_t + \sum_{i=1}^{n} E_i \left[e^{-\Delta t'/\rho_i} q_{i,t-\Delta t} + (\epsilon_t - \epsilon_{t-\Delta t}) \frac{1 - e^{-\Delta t'/\rho_i}}{\Delta t'/\rho_i} \right]. \tag{2.31}$$

The expression $q_{i,t-\Delta t}$ is the hereditary integral for each Prony term at the end of the previous time increment $t - \Delta t$ which has been computed in the last time increment. It should be noted that the

integration is performed in an explicit manner. Accuracy of the integration is controlled by a user defined tolerance that limits the allowed maximum strain rate.

This algorithm is implemented in the commercial finite element solvers Abaqus/Standard and Abaqus/Explicit through user defined subroutines UMAT and VUMAT, respectively. The code is validated against analytical solutions for the simple cases of relaxation and creep.

Chapter 3

Quasi-Static Shape Recovery of Polymer Beams

3.1   Introduction

The operation of deployable structures follows the sequence of folding, stowage, deployment, and shape recovery. For elastic structures, the stowage step is irrelevant because the equilibrium state is path independent. For viscoelastic structures, the stowage period changes the subsequent behavior. This chapter formulates and solves analytically the folding-stowage-deployment process of a model structure as a time-dependent boundary value problem with the aim of elucidating some of the general features of the long term behavior of viscoelastic structures after stowage.

The model problem is a homogeneous linear viscoelastic beam with a uniform temperature distribution under bending. The beam is first subject to a constant deflection for a given holding time, after which the prescribed deflection is reduced to zero quasi-statically. The beam is then allowed to recover under a load free condition. One feature common to both the shape recovery problem in composite deployable structures and the model problem is the switch of prescribed condition from constant displacement in the holding duration to constant (zero) traction in the recovery period. It is this aspect of the phenomenon that renders it of practical significance.

This chapter presents a closed-form solution for the shape recovery problem of a viscoelastic beam with experimentally measured material properties based on separation of variables. The results are validated against finite element simulations and experimental measurements. In particular, the effect of holding duration and temperature on shape recovery time is investigated. The analytical relation obtained allows easy comparison between different material systems and optimization of stowage conditions in practical applications.

3.2   Background

For quasi-static viscoelastic problems, Alfrey (1944) and Tsien (1950) were the first to obtain solutions that are separated into a temporal and a spatial part under the condition of constant Poisson's ratio. Either the surface traction or displacement was specified for the entire history in the cases discussed. Situations involving general viscoelastic materials are often tackled with integral transform methods. Since the governing equations in the transformed domain have a identical form with that of linear elasticity, it follows that the transformed viscoelastic solution can be obtained directly from the solution of the corresponding elastic problem. The final solution in the time domain will be realized upon inversion of the transformed solution. This analogy is known as the elastic-viscoelastic correspondence principle and was first formally recognized by Read (1950) through the Fourier transform. Lee (1955) and Lee et al. (1959) further developed the analogy in terms of Laplace transform and applied the procedure to a variety of problems. However, one limitation of integral transform methods is that the type of boundary condition at any point, whether it be prescribed traction or displacement, is required to be time-invariant.

Viscoelastic contact problems such as the indentation of a viscoelastic half-space (Hunter, 1960; Lee and Radok, 1960; Graham, 1965) and the rolling of a cylinder on a viscoelastic half-space (Hunter, 1961; Morland, 1962 1967) are practical examples involving changing boundary conditions. For these problems, the transform methods are inapplicable and no general methods of solution are available. Similarly, because the type of boundary condition switches from prescribed displacement to prescribed load over time, the shape recovery process belongs to the class of viscoelastic problems where integral transform methods and the elastic-viscoelastic correspondence principle are not applicable. The solution needs to be developed directly in the time domain.

3.3   Analysis

Consider a beam that is initially straight in the unloaded state with a length of $2L$. A uniform bending moment is applied such that the tip of the beam reaches the specified deflection w_0 at a constant rate C. The deflected shape of the beam is then maintained with the tip deflection w_0 constant for a given holding period. During the holding period, we seek to determine the evolution of the bending moment $M(t)$. At the end of the holding period, the moment is reduced quasi-statically to zero and we seek to find the change of deflected shape over time under zero moment. Figure 3.1 shows the beam geometry. The sequence of deformation is described by time-dependent traction and boundary conditions summarized as follows,

$$
\begin{aligned}
Loading &: \quad w(t) = Ct, \quad 0 < t \le t_l \\
Holding &: \quad w(t) = w_0, \quad t_l < t \le t_h \\
Unloading &: \quad w(t) = w_0 - C(t - t_h), \quad t_h < t \le t_u \\
Recovery &: \quad M(t) = 0, \quad t \ge t_u
\end{aligned}
$$

where $w(t)$ is the tip deflection, t_l is the time required for imposing deflection, t_h is at the end of the holding period, and t_u is the instant at which the moment reaches zero.

Under quasi-static conditions, the deflection of the beam is governed by the following equation,

$$
\frac{d^2 y(x,t)}{dx^2} = \frac{M(t)}{E(t)I}, \quad 0 \le x \le L \tag{3.1}
$$

where $y(x,t)$ is the vertical deflection, $E(t)$ is the relaxation modulus and I is the second moment of area of the beam cross section.

The temperature distribution is uniform throughout the beam but varies with time. We look for spatial-temporal separable variable solutions to Equation (3.1) for the moment $M(t)$ during holding and deflection $y(x,t)$ during recovery. The operational restrictions of employing separation of variables technique are well documented (Christensen, 1982; Hilton, 2001) and are followed in the present analysis.
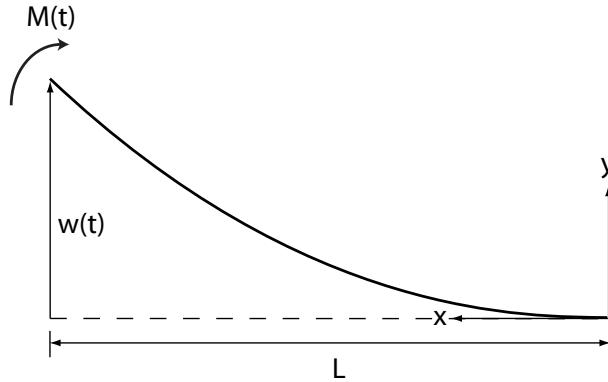
Figure 3.1. Beam geometry.

3.3.1   Constitutive Model

To provide a basis for analysis and comparison with experimental results later on, the linear viscoelastic material model of low density polyethylene (LDPE) is first described.

i	E_i $[MPa]$	ρ_i [s]
∞	136.2	——
1	150.6	2.43×10^{-2}
2	74.81	2.17×10^{-1}
3	68.26	1.52
4	65.22	1.24×10
5	62.85	1.49×10^2
6	49.83	1.69×10^3

Table 3.1. Prony series parameters for LDPE master curve.

The uniaxial constitutive equation for linear viscoelastic material is

$$\sigma(t) = \int_0^t E(t' - s') \frac{d\epsilon(s)}{ds} ds, \tag{3.2}$$

where σ is stress, ϵ is strain, E is the relaxation modulus, t' and s' are reduced times defined as

$$t' = \int_0^t \frac{du}{a_T(T)} \quad \text{and} \quad s' = \int_0^s \frac{du}{a_T(T)}. \tag{3.3}$$

The relaxation modulus is represented by a Prony series as

$$E(t) = E_\infty + \sum_{i=1}^n E_i e^{-(t/\rho_i)}, \tag{3.4}$$

where t is time, E_∞ is the long term modulus, E_i are the Prony coefficients, and ρ_i are the relaxation times. The temperature shift factor is expressed by the Williams-Landel-Ferry (WLF) equation,

$$\log a_T = -\frac{c_1(T - T_0)}{c_2 + (T - T_0)}, \tag{3.5}$$

in which c_1 and c_2 are material constants that depend on the particular polymer and the logarithm is of base ten.

The material properties of LDPE were characterized through a series of tensile relaxation tests on rectangular test coupons cut from LDPE sheet stock with a thickness of 1.59 mm obtained from United States Plastic Corporation. Figure 3.2 shows the relaxation modulus master curve of LDPE at the reference temperature. Table 3.1 lists the Prony series parameters. The material constants c_1 and c_2 were determined to be

$$c_1 = -8.74 \quad \text{and} \quad c_2 = -40.41.$$
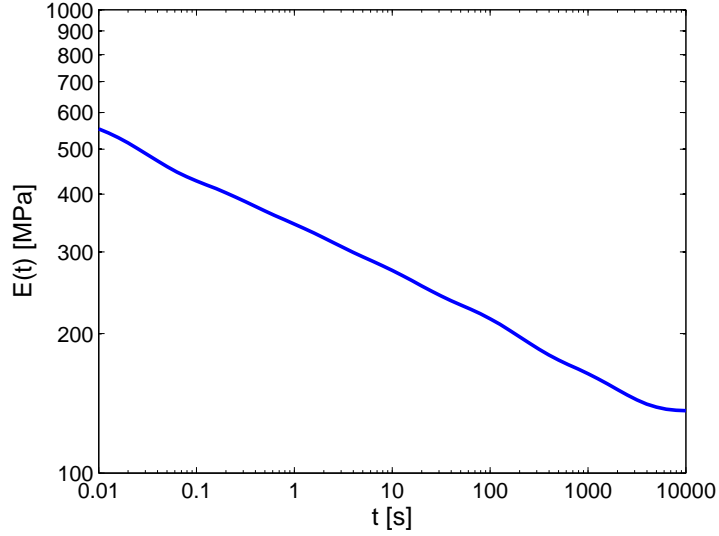
Figure 3.2. Master curve for LDPE at $22°$C.

3.3.2 Load Relaxation and Shape Recovery

Consider first the load response $M(t)$ over time under the applied deflection $w(t)$ for $0 \leq t \leq t_h$. Solving Equation (3.1) for $M(t)$, we obtain

$$M(t) = \frac{2I}{L^2} \int_0^{t_h} E(t - \tau) \frac{dw(\tau)}{d\tau} d\tau, \tag{3.6}$$

where t_h is the holding time. To generalize the solution for all temperatures, we carry out the analysis in the reduced time domain and write

$$M(t') = \frac{2I}{L^2} \int_0^{t'_h} E_{T_0}(t' - \tau') \frac{dw(\tau')}{d\tau'} d\tau', \tag{3.7}$$

where t'_h is the holding duration in the reduced time domain, E_{T_0} is the relaxation modulus master curve at the reference temperature. For an arbitrary temperature history, all time variables are first converted into reduced time variables through Equation (3.3) and inserted into Equation (3.7) for evaluating $M(t')$. In practice, the loading time is often a small fraction of holding time and hence the applied deflection $w(t')$ can be closely approximated by an instantaneous jump,

$$w(t') = w_0 H(t'), \quad 0 \leq t \leq t'_h \tag{3.8}$$

where $H(\tau')$ is the Heaviside step function. Equations (3.7) and (3.8) only provide the solution of $M(t')$ for $0 \leq t' \leq t'_h$. The final expression of $M(t')$ is obtained by stitching the solution with the imposed zero moment condition for $t' > t'_h$. This gives

$$M(t') = \frac{2I}{L^2} E_{T_0}(t') \left(1 - H(t' - t'_h)\right). \tag{3.9}$$

Note that the unloading is again approximated as an instantaneous event. Figure 3.3 plots the graphical solution of Equation (3.9) for $t'_h = 100$ s normalized by the instantaneous moment $M(0)$. The normalized moment demonstrates the expected relaxation behavior under a constant imposed deflection, and varies with time as the uniaxial relaxation modulus.

The beam deflection is obtained by solving Equation (3.1) for $y(x, t')$, which gives

$$y(x, t') = \frac{x^2}{2I} \int_0^{t'} D_{T_0}(t' - \tau') \frac{dM(\tau')}{d\tau'} d\tau', \quad a \leq x \leq b \tag{3.10}$$

where D_{T_0} is the creep compliance at the reference temperature. Inserting Equation (3.9) into Equation (3.10), the beam deflection is given by

$$y(x, t') = \frac{x^2}{L^2} w_0, \quad 0 \leq t \leq t'_h \tag{3.11}$$

$$y(x, t') = \frac{x^2}{L^2} w_0 \left(1 - D_{T_0}(t' - t'_h) E_{T_0}(t'_h) - \int_{t'_h}^{t'} D_{T_0}(t' - \tau') \frac{dE_{T_0}(\tau')}{d\tau'} d\tau'\right), \quad t' > t'_h \tag{3.12}$$

For $0 \leq t' \leq t'_h$, the beam deflection is constant over time. This result is consistent with the imposed condition of constant deflection during the holding stage. For $t' > t'_h$, the change of deflected shape over time depends on the reduced holding time t'_h. Figure 3.4 plots the deformed shapes at 10 s, 100 s, and 10000 s after a holding period of $t'_h = 100$ s with $2L = 20$ mm.

The first term in Equation (3.12) is the transient response to the moment $M(t')$ during the holding stage, whose effect continues beyond t'_h. The second term and the third term are respectively the instantaneous and transient response to the step change of $M(t')$ at t'_h. As t' tends to t'_h, the temporal part of Equation (3.12) reduces to $1 - D_{T_0}(0) E_{T_0}(t'_h)$, which indicates that the amount of instantaneous recovery is linearly dependent on the relaxation modulus at the unloading instant.

3.3.3 Effect of Temperature and Holding Duration

The tip deflection normalized by w_0 is plotted for different values of t'_h in Figure 3.5. The beam recovers to its original shape asymptotically and the recovery process takes longer when the t'_h increases. To establish a measure for recovery performance, we define the recovery time as follows. First denote by t'_f the time required to reach a prescribed final deflection by that satisfies the following relation,

$$\frac{w(t'_f)}{w_0} = e \tag{3.13}$$
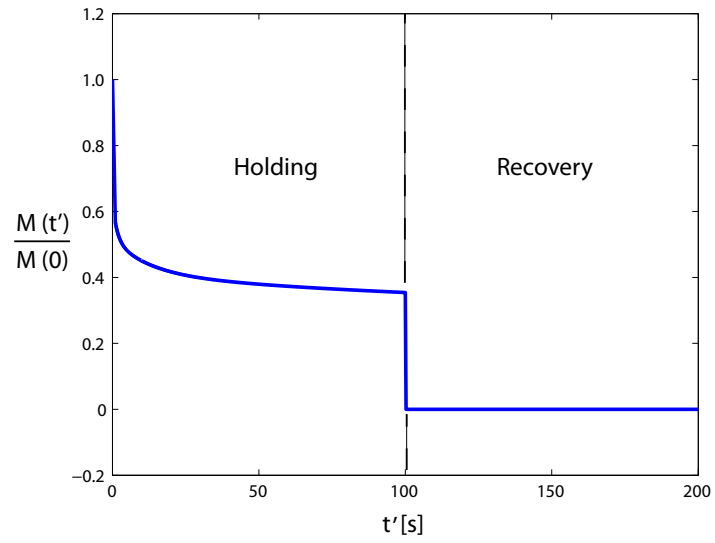
Figure 3.3. Load relaxation of LDPE beam during holding period.
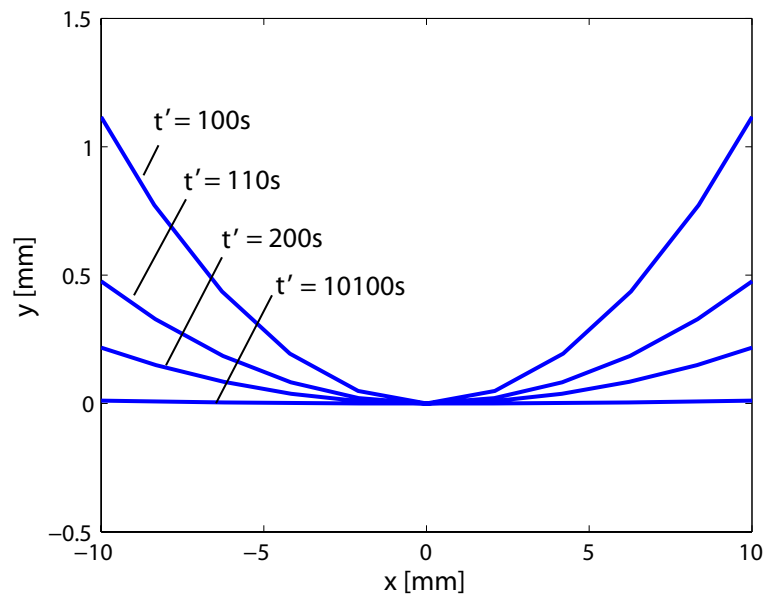
Figure 3.4. Deformed shapes at 0 s, 10 s, 100 s, and 10000 s after a holding period of 100 s.

in which e is a constant that depends on the required precision on the final deflection. The recovery time can then be defined to be $t'_r = t'_f - t'_h$. For $e = 0.1$, the relation between t'_r and t'_h is shown on a log-log plot in Figure 3.6. The straight line in this plot suggests that t'_r increases with t'_h in a manner that is similar to a creep response. Increase in time and temperature during holding will raise the recovery time, but the sensitivity reduces over time.

Since the time variables are expressed in the reduced time domain, Figure 3.6 can be regarded as a master curve relating recovery time and holding duration. Given a temperature history and holding duration in real time scale, the holding duration in reduced time scale can be determined through Equation (3.3). The corresponding recovery time in reduced time under the same temperature is then found from the master curve and the real recovery time is obtained by an inverse mapping of Equation (3.3).
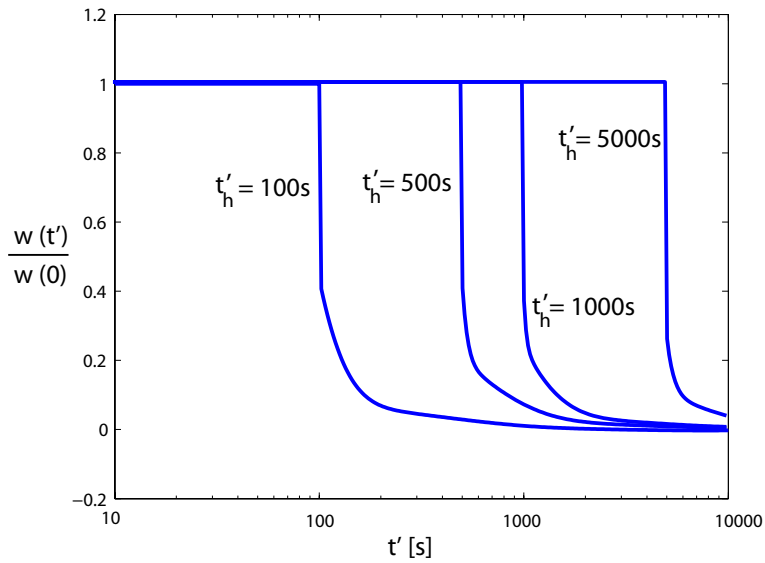
Figure 3.5. Beam deflection over time for different holding durations.

3.4   Experiments

The analytical results can be verified experimentally with a four-point bending test. The force diagram of the bending test is shown in Figure 3.7. Equal and opposite bending moments on the beam were applied through four vertical forces provided by a top and a bottom fixture. Rectangular LDPE beams with a length of 170 mm, a width of 13.0 mm, and a thickness of 1.59 mm were cut from the same sheet stock used for material characterization. The strip was placed between the fixtures and subject to the loading profile described in Section 3.3 at the reference temperature of $22°C$. Specific values of the prescribed conditions are summarized in Table 3.2.
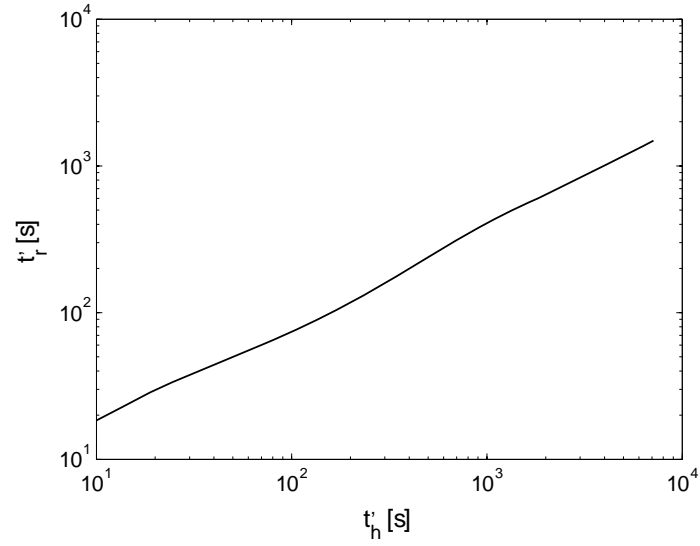
Figure 3.6. Master curve relating recovery time and holding duration.

t_l	8.0 $[s]$
t_h	1008.0 $[s]$
t_u	1012.5 $[s]$
C	1.0 $[mm/s]$
w_0	8.0 $[mm]$

Table 3.2. Prescribed condition definitions.

The load and shape measurements were taken respectively with an Instron load cell and a high definition camcorder. Prior to the experiment, the orientation of the camcorder was adjusted until there was no distortion in the image of a square taken by the camcorder. This ensured that the camcorder was parallel to the plane of motion of the beam. A resolution of 1920×1080 pixels and a frame rate of 30 frames per second were used. Figure 3.8 plots images of the beam during the loading, holding, and unloading stages, while Figure 3.9 plots the shape recovery of the beam over time under zero moment in a representative test.

The coordinates of the beam centerline were determined from the recorded images by first tracing the beam edges using the Canny edge detection algorithm in MATLAB and averaging the top and bottom edges. A cubic spline interpolation was used to reconstruct the continuous centerline coordinates from the sampled pixel coordinates. The measured load response and deformed shapes are presented in Section 3.6.
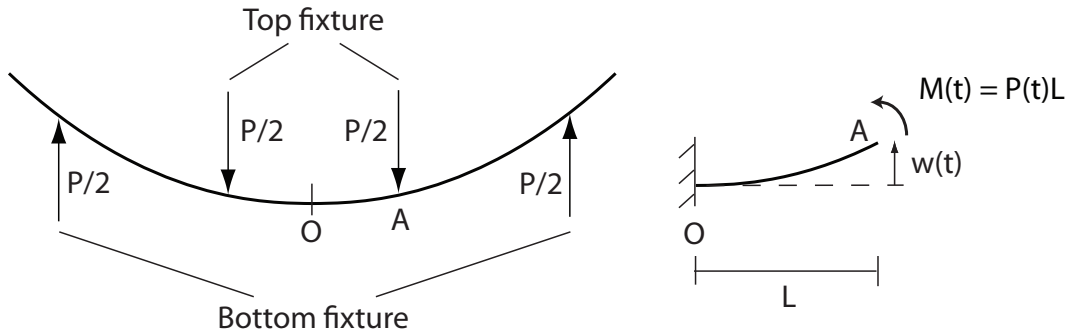
Figure 3.7. Free body diagram for four-point bending of a beam.
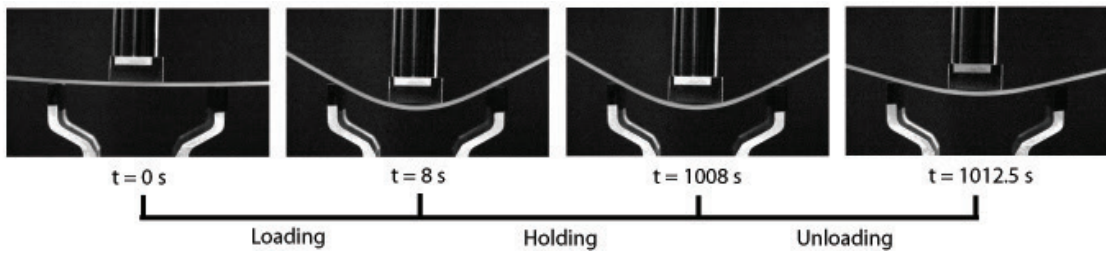
Figure 3.8. Images of beam under four-point bending at different stages.

3.5 Finite Element Simulations

The relatively simple analytical relations illustrated in Section 3.3 were obtained by approximating loading and unloading as instantaneous events. To account for the effects of finite loading and unloading times, a finite element simulation was carried out using the commercial simulation package
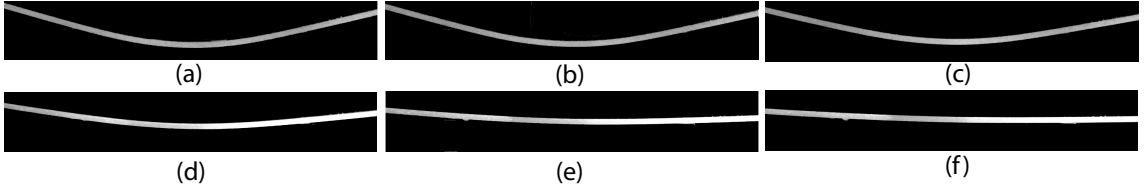
Figure 3.9. Shape recovery under zero moment: (a) during holding; (b) 1 s after unloading; (c) 10 s after unloading; (d) 100 s after unloading; (e) 1000 s after unloading; (f) 10000 s after unloading.

Abaqus/Standard. The finite element analysis aimed to quantitatively reproduce the beam behavior observed experimentally in Section 3.4. Hence the prescribed deflection and loading profiles were the same as described in Table 3.2.

The LDPE strip was modeled with 688 full integration quadrilateral shell elements (S4). The four loading points of the fixture in contact with the strip were modeled as rigid cylinders with a radius of 0.1 mm using the *RIGID BODY function. A frictionless contact interaction was enforced between the loading points and the beam through the *SURFACE INTERACTION command. Gravity load was included by the use of *GRAV.

Geometrically nonlinear, quasi-static analyses were carried out by means of *NLGEOM and *VISCO. All the rotational freedoms of the center node of the strip were constrained. Vertical displacements were applied to the two top cylinders to impose a deflection of the strip through the contact interaction while the all the degrees of freedom of the two bottom cylinders remained fixed throughout the analysis. All simulations started at a time of 10^{-3} s and proceeded until 10^5 s with automatic time incrementation. The size of the time increment was determined so that the creep strain rate change over an increment was within the accuracy tolerance parameter *CETOL. It was found that a tolerance limit of 10^{-4} was able to achieve accurate results with reasonable computational expense.

The viscoelastic properties of LDPE expressed in terms of the Prony series in Table 3.2 were assigned with the option *VISCOELASTIC, TIME=PRONY. The Abaqus/Standard implementation requires the specification of shear and bulk moduli, which are related to the uniaxial modulus through the equations

$$G(t) = \frac{E(t)}{2(1 + \nu)}, \tag{3.14}$$

$$K(t) = \frac{E(t)}{3(1 - 2\nu)}, \tag{3.15}$$

where ν is the Poisson's ratio, G is the shear modulus and K is the bulk modulus. To be consistent with the assumptions underlying the separation of variable solution developed in Section 3.3, a

constant Poisson's ratio was used. This assumption implicitly leads to the condition that bulk and shear moduli are synchronous (Hilton, 1998 2001). However, the measurement of time-dependent Poisson's ratio and its conversion to other material moduli are extremely sensitive to experimental errors (Lu et al., 1997; Tschoegl et al., 2002). As the bending behavior of beams is primarily one-dimensional, the effect of Poisson's ratio is expected to be minor. A Poisson's ratio of 0.49 was determined from relaxation tests and this value was assumed to be constant in the present study.

3.6   Results Comparison

Comparisons between analytical predictions, finite element simulations and experimental measurements for the vertical force acting at the top of the LDPE strip during the holding period are shown in Figure 3.10. All results are in close agreement except for the first 8 seconds, where the analytical prediction differs from the finite element simulation and experimental measurements. The discrepancy is due to the assumption that the deflection is applied as a step function in the theoretical analysis and therefore achieves its maximum value instantaneously. This transient effect produces no apparent difference in the load response beyond the loading period. The good agreement of the results also suggests that friction and gravity effects are insignificant.

The deformed shapes of the beam and the deflection at A during the recovery period are compared in Figures 3.11 and 3.12. Both the analytical prediction and finite element simulations have captured the details of the shape recovery process accurately.
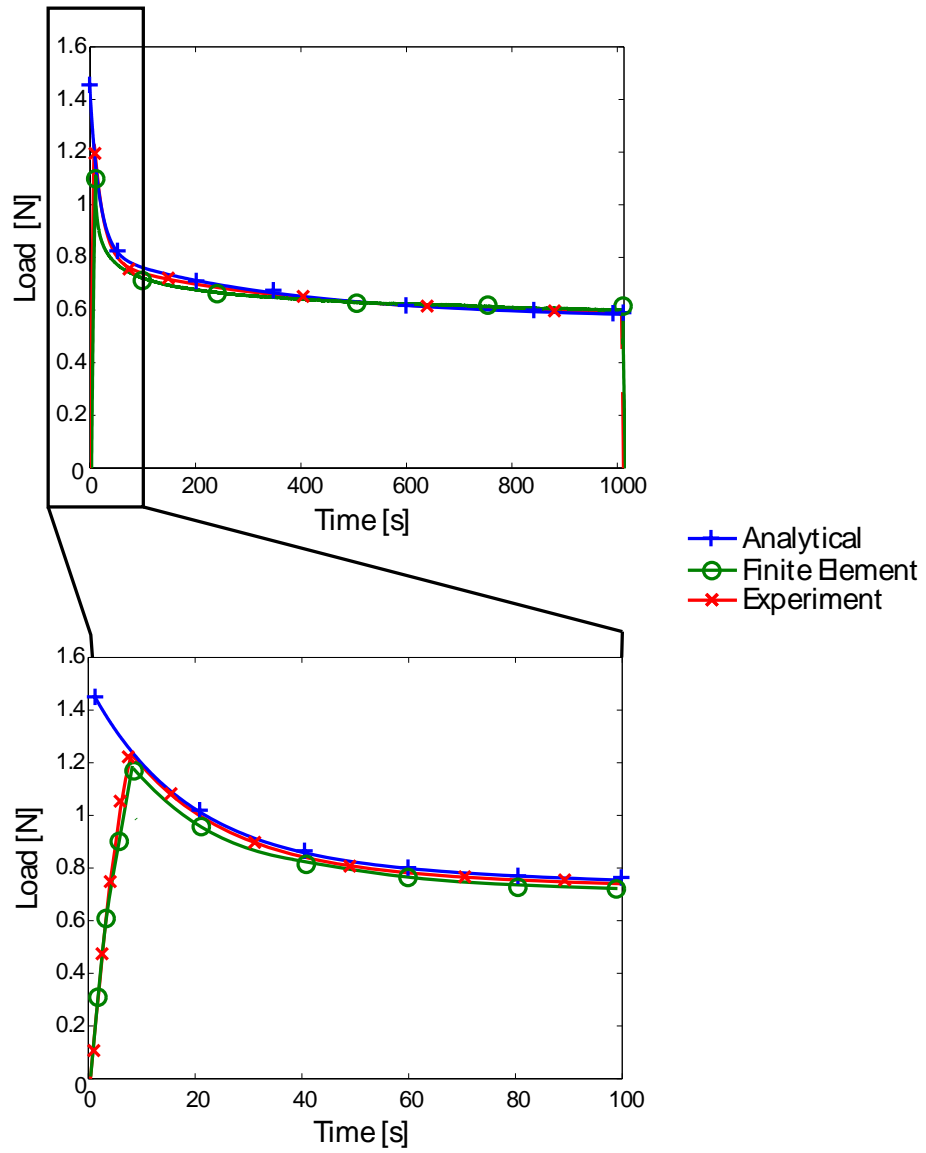
Figure 3.10. Load relaxation during holding period.
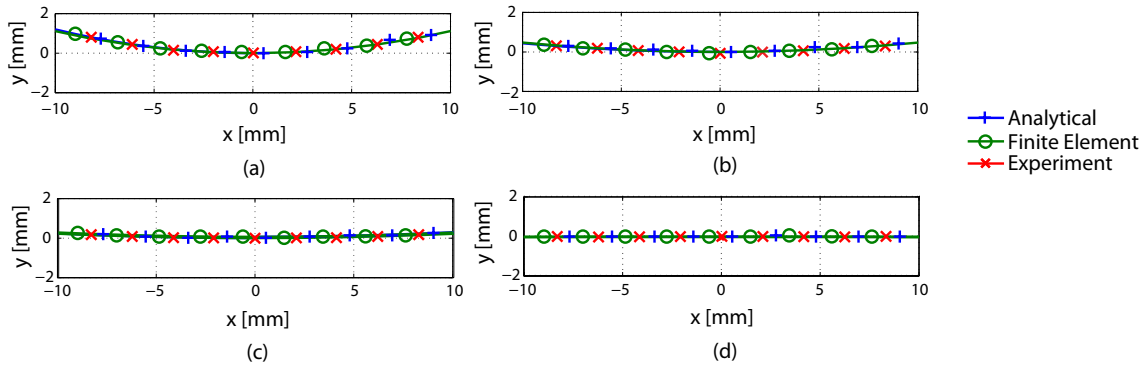
Figure 3.11. Deformed shapes during recovery: (a) during holding; (b) 10 s after unloading; (c) 100 s after unloading; (d) 10000 s after unloading.
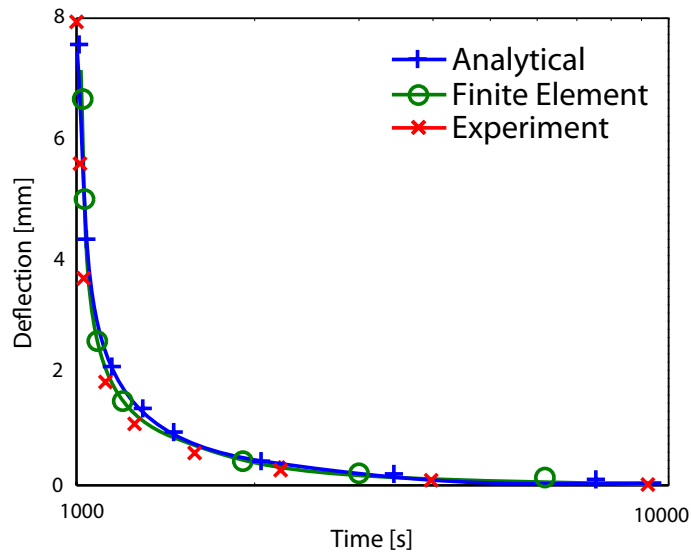
Figure 3.12. Deflection recovery for a holding period of 1000 seconds.

Chapter 4

Folding, Stowage, Deployment, and Shape Recovery of Polymer Shells

4.1 Introduction

In Chapter 3, stowage effects were studied analytically by solving an example problem of a homogeneous beam under bending. This chapter investigates the same type of stowage problem, but the focus is on homogeneous cylindrical shells.

Thin shells are used extensively to design deployable structures because they are able to undergo large shape reconfiguration with relatively small deformation by virtue of geometric nonlinear behavior. In particular, thin shells in the form of a partial cylindrical surface with radius R and subtended angle α as shown in Figure 4.1 can be bent extensively by buckling to form a localized fold (Figure 4.2). The structure is contained in this packaged state with minimal effort and self deploys to its original configuration upon release of any constraints. This structural form is often known as a tape-spring and is the working principle behind the storable tubular extensible member (Rimrott, 1965), which has been used as spacecraft antennas and to deploy solar arrays (Pellegrino, 1995).

Local buckling of elastic cylindrical shells under bending allows high longitudinal curvature to be achieved without permanent deformation. When the shell exhibits viscoelastic properties, the behavior is complicated by time and temperature dependence . The interaction between material behavior and structural instability gives rise to characteristics that are distinct from the elastic problem. This chapter specifically studies the effects of rate and temperature on the geometrically nonlinear behavior.
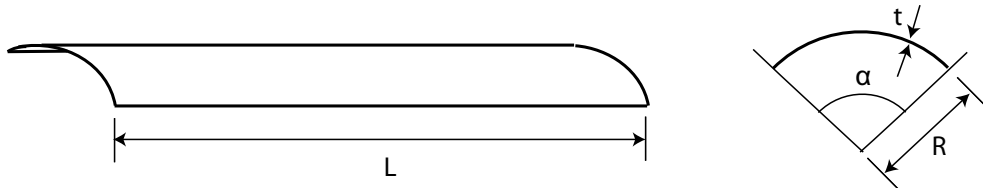
Figure 4.1. Geometry of open cylindrical shell (tape-spring).

Figure 4.2. Tape-spring made of LDPE having a radius of 19 mm and a subtended angle of 150°: (a) deployed and (b) folded.

4.2 Background

High curvature folding of open elastic cylindrical shells has been exploited in many deployable structures and is therefore well studied. Briefly, bending first induces ovalization of the shell cross section. The bending stiffness is gradually reduced as the ovalization progresses until the structure finally collapses by local buckling associated with a limit peak moment. The deformed configuration is characterized by three different regions as shown in Figure 4.3: a longitudinally curved region with zero transverse curvature, an almost straight region with the original transverse curvature, and a transition region connecting the two (Calladine, 1988). The fold can spread under a constant bending moment which has a value much lower than the peak (Seffen and Pellegrino, 1999). This is a characteristic feature in steady-state propagation of instabilities in elastic structures (Kyriakides, 1994) and can be captured using a simple but exact energy balance argument (Chater and Hutchinson, 1984). Throughout the entire bending process, the deformation remains elastic and is completely reversible upon removal of the applied moment.

4.3 Experiments

The experimental program consisted of two sets of tests. The first set was conducted to investigate the folding-stowage process with careful control and measurement of load and displacement with respect to time. This experiment helps to develop an understanding of the shell deformation prior
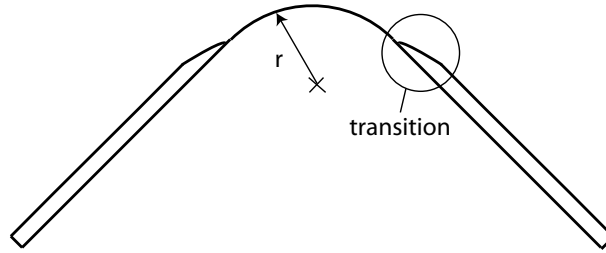
Figure 4.3. Configuration of a bent tape-spring with three distinct zones of deformation.

to deployment. The second set of tests measured continuously the response of the shell from folding, stowage to deployment over time, but focused on analyzing the final deployment and shape recovery behavior.

4.3.1 Fabrication of Cylindrical Shells

Cylindrical shell specimens were fabricated from flat LDPE sheets obtained from United States Plastic Corporation through a thermal remolding process. The LDPE sheet stock had a length of 610 mm, a width of 914 mm, and a thickness of 0.79 mm. Flat LDPE sheets were first cut to length, sandwiched between two release fabric layers, wrapped around a cylindrical steel mandrel, restrained with heat shrink tape, and subject to a thermal cycle. The assembly was heated to 120°C, maintained at this temperature for 4 hours, and then allowed to cool to room temperature in 8 hours at a constant cooling rate inside an oven with a temperature control precision of ±2°C. The long heating and cooling periods allowed enough time for LDPE to recrystallize and to minimize the effect of physical aging, respectively. To further eliminate the effect of physical aging, the fabricated specimens were kept at room temperature for another 24 hours before any tests were performed. After this procedure, it was assumed that temporally stable mechanical properties had been achieved in the remolded material.

The dimensions of two specimens are listed in Table 4.1, in which $\bar{t}$ denotes the average thickness of the shell. The measured shell radius is higher than that of the steel mandrel because the shells recoiled by a consistent amount after release from the mold. The thickness variation was measured using an Elcometer 456 coating thickness gauge with a resolution of 10 microns. A rectangular grid was drawn on each shell specimen and the thickness at the grid points was measured. The grid spacing is such that the distance between adjacent grid points is 16 mm along the length and 10 mm along the circumference of the shell. The thickness contours of the specimen used in the folding-stowage experiment are shown in Figure 4.4.

Experiment	L [mm]	R [mm]	$\bar{t}$ [mm]	α [deg]
Folding-Stowage	272.0	19.0	0.73	150
Deployment-Recovery	398.0	19.0	0.73	150

Table 4.1. Dimensions of tested specimens.
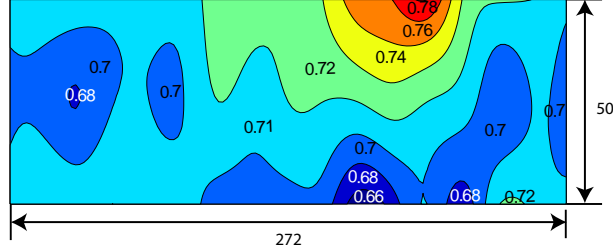
Figure 4.4. Thickness distribution, in millimeters, of a representative specimen. The vertical coordinate is the cross-sectional arc-length.

4.3.2 Folding-Stowage Experiment

The folding-stowage sequence was carried out by bending the specimen to a prescribed end rotation and holding the rotation angle fixed over time. The specimen was bent in an opposite sense (i.e. the longitudinal and transverse curvature changes have opposite signs) by applying eccentric compression on the end cross sections by means of an Instron testing machine. To allow the end cross sections to deform and rotate freely during folding, the connection between each end of the specimen and the load frame was established through the points of contact with thin aluminum plates attached to the Instron testing machine. The test configuration is schematically shown in Figure 4.5. The procedure adopted in the present experiment allows full control of the boundary conditions and also precise tracking of the load and displacement histories over time, which is important for achieving repeatable measurements in the present path dependent problem.

Tests were carried out in displacement-controlled mode inside an environmental chamber. Prior to testing, the specimen was preloaded with a small compression to secure contact. A downward displacement of 80 mm was applied to the specimen, which was then held in this configuration for 5000 s. Two temperatures (T), 15°C and 22°C; and two displacement rates ($\dot{u}$), 1 mm/s and 5 mm/s, were used. Full field views of the deforming shell were captured continuously using a high-resolution digital camcorder.

The measured load P and displacement u over time during folding are plotted in Figure 4.6. To provide a basis for discussion, the load response has been converted to a plot of moment M vs. rotation θ in Figure 4.7 for the case of $\dot{u} = 1$ mm/s at $T = 22$°C. The rotation is obtained from summing the end rotations measured from the images of the deformed specimen, while the moment is the product of the measured load and the horizontal distance from the line of load to the mid-span
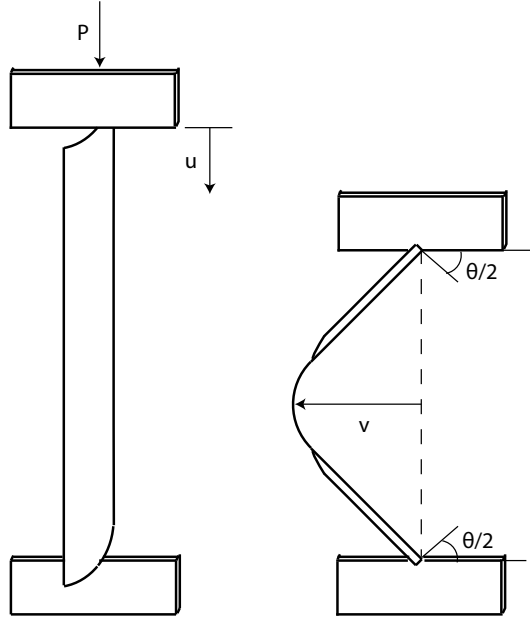
Figure 4.5. Schematic of folding-stowage test.

of the shell, also measured from the images. Images of the specimen at different stages of the test are shown in Figure 4.8. These shapes correspond to the points marked in Figure 4.7.

The initial part of the response shown in Figure 4.7 shows a stiff, softening behavior. The shell bends uniformly, as indicated in configurations A - C in Figure 4.8, with a bending stiffness EI, where I is the second moment of area of the shell cross section about the neutral axis. The nonlinearity is due to changes in both quantities in the bending stiffness: first the second moment of area reduces with rotation as a result of ovalization and second the longitudinal modulus relaxes with time because of viscoelasticity. In this uniform deformation stage, the longitudinal curvature is given simply by $\kappa_l = \theta/L$. Uniform bending ceases at configuration C, which is just past a local instability at which a maximum moment is attained. The buckle initiates on the compression side, in the middle of the shell. Although the applied loading is not completely symmetric due to gravity, this asymmetry is too small to have a significant impact on the location of the buckle. From configuration C to E, the moment drops sharply as the end rotations continue to increase. This corresponds to an expansion of the buckle in the transverse direction and unloading of the regions away from the buckle. The buckle has fully developed by configuration E, where a localized fold region with zero transverse curvature is formed and the deformation is as described in Figure 4.3, where longitudinally curved and straight phases coexist. From this point onwards, the moment stays constant with rotation and the fold length increases as shown in configurations E - G, as a result of the propagation of the localized fold into the straight portions of the shell. This fold propagation could be dynamic but occurs in a quasi-static manner in the present case because a

displacement-controlled loading mode has been adopted.

Viscoelastic effects in the folding shell are apparent in Figure 4.6. Similar types of nonlinear response are observed for the two different rates of folding and temperatures, but the maximum load values are different. It can be seen in Figure 4.6 that higher maximum loads are found at lower temperatures and faster rates. This is explained by the time and temperature dependence of viscoelastic materials. Their mechanical response is in general nonlinearly affected by rate and temperature, but the stresses are always higher at lower temperatures and faster rates. In Section 4.4 we will employ a viscoelastic constitutive model to analyze such effects in detail.

Load relaxation during stowage is evidenced by plotting the change in load over time on a semi-log scale in Figure 4.9. The linearity of the curves from 1000 s to 5000 s on a log time axis implies that the reduction in load is exponential in time. After 5000 s the load has dropped to about one-third of its value at the end of folding. At both rates, higher loads are measured at the lower temperature throughout the entire stowage period. The effect of folding rate on the load response during stowage diminishes as time progresses. This can be concluded from the observation that the load at the two different rates at the same temperature have similar values from $t = 1000$ s onwards.

4.3.3 Deployment-Recovery Experiment

For measuring the deployment and recovery dynamics, experiments were performed using the test configuration shown in Figure 4.10. The specimen was clamped at the bottom and positioned vertically. It was first folded to an angle of 87° in 9 s by manually applying a follower force on the free end and was then held stowed for 983 s. While in the stowed configuration, the force at the free end was measured by connecting the specimen to a load cell through a string. Deployment was initiated by cutting the string at the end of the stowage period. The entire process was carried out at 22°C. In this procedure, the exact rate of folding was not precisely known, but its effect was found in Section 4.3.2 to be transient only and therefore it had negligible impact on the deployment behavior.

To characterize the deformation, a target point P near the free end was marked (Figure 4.10) and its lateral displacement x_p was tracked during deployment. Values of x_p larger than 20 mm were extracted from images taken using a high resolution camcorder with a frame rate of 30 fps. A laser displacement sensor (Keyence LK-G87) was used to measure the values of x_p below 20 mm that could not be measured accurately from the images.

Figure 4.11 shows the deployed shapes over time with different time steps. The corresponding values of x_p and time are marked in Figure 4.12, which includes three detailed views of the displacement response over time, each highlighting a particular feature. The process can be divided into three stages with distinctive characteristics. A dynamic response is seen during the first 5 s, Figure 4.12(b). A low vibration magnitude with a period of about 0.8 s about a finite displacement
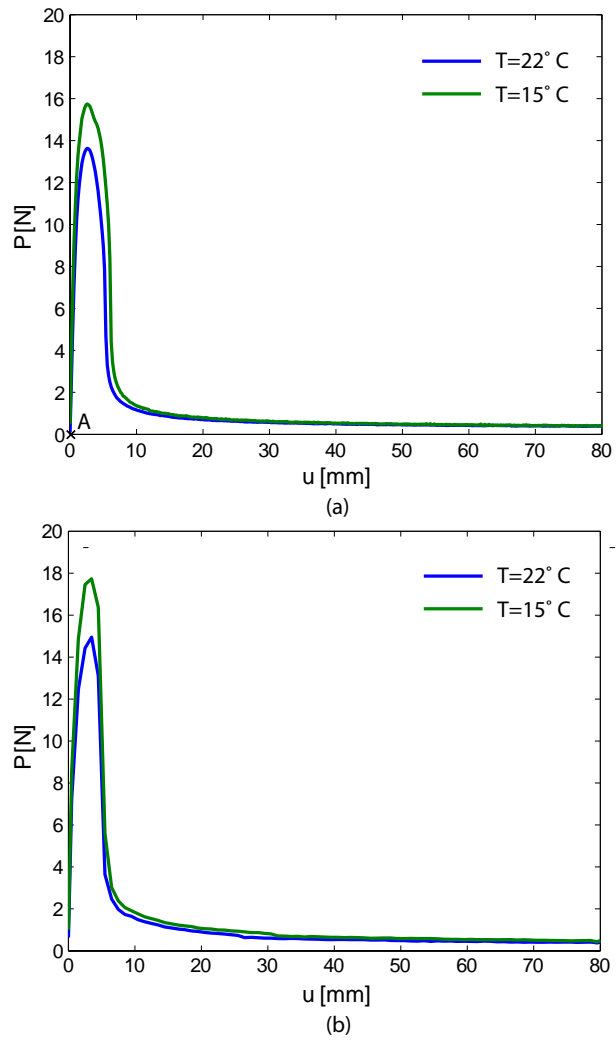
Figure 4.6. Measured load response during folding: (a) $\dot{u} = 1$ mm/s and (b) $\dot{u} = 5$ mm/s.
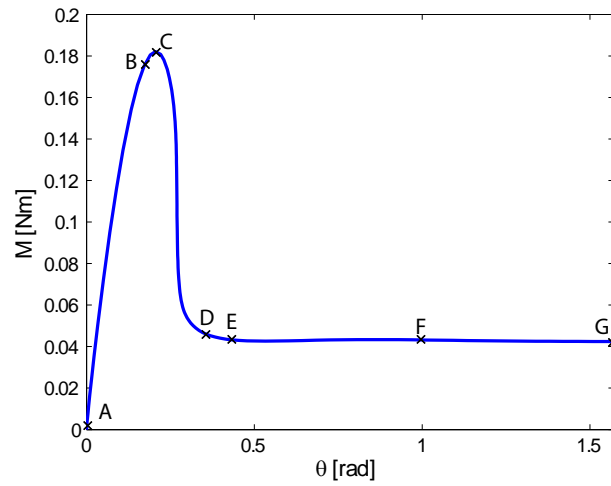
Figure 4.7. Measurements of moment vs. rotation for $\dot{u} = 1$ mm/s and $T = 22°$C.
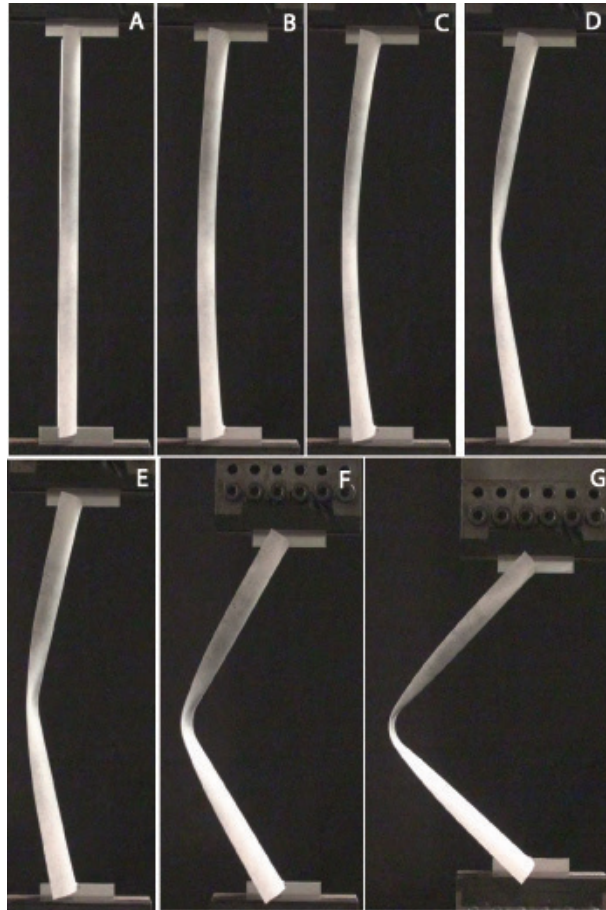
Figure 4.8. Sequence of deformed shapes corresponding to the response in Figure 4.7.
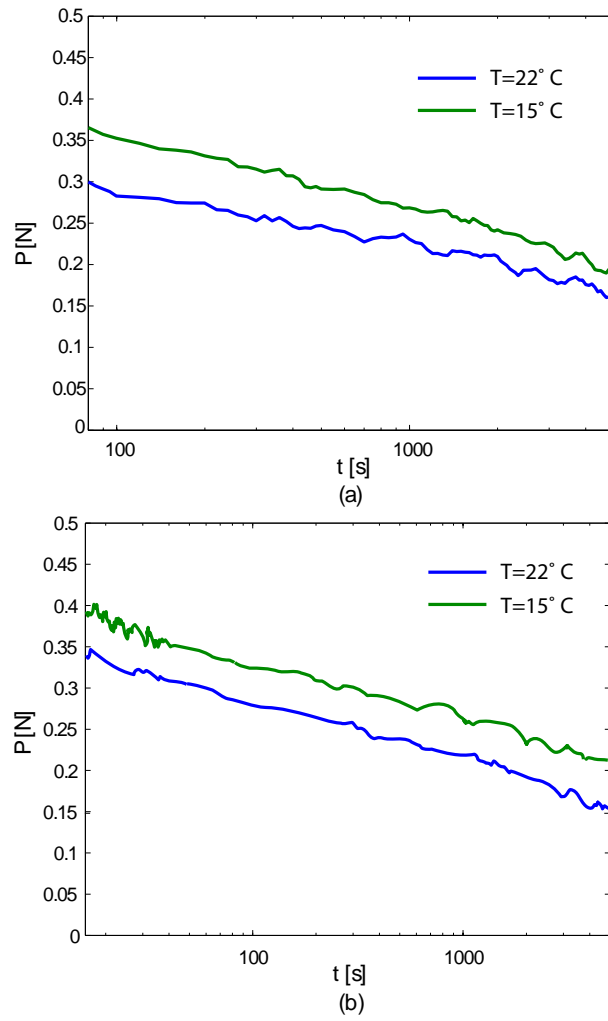
Figure 4.9. Measured load relaxation in stowed configuration: (a) $\dot{u} = 1$ mm/s and (b) $\dot{u} = 5$ mm/s.

that decreases with time is observed. The next phase involves a steady deployment that occurs between 5 s and 55 s, with the lateral displacement actually overshooting the deployed configuration by 11 mm, Figure 4.12(c). An interesting feature in these first two stages is that the fold location is constant: this behavior is different from that of a linear elastic shell in which deployment is accompanied by the fold traveling towards the fixed end (Seffen and Pellegrino, 1999). Finally, a slow creep recovery of the fold cross section leads to a nearly zero lateral displacement over a period of 3000 s, Figure 4.12(d). After the test was terminated, a close examination of the shell revealed that the cross section geometry had not completely recovered, but the magnitude of deformation was too small to be measured precisely with the present experimental setup. The test specimens were monitored visually over three months and the cross section of the fold was found to continue recovering in an asymptotic manner.
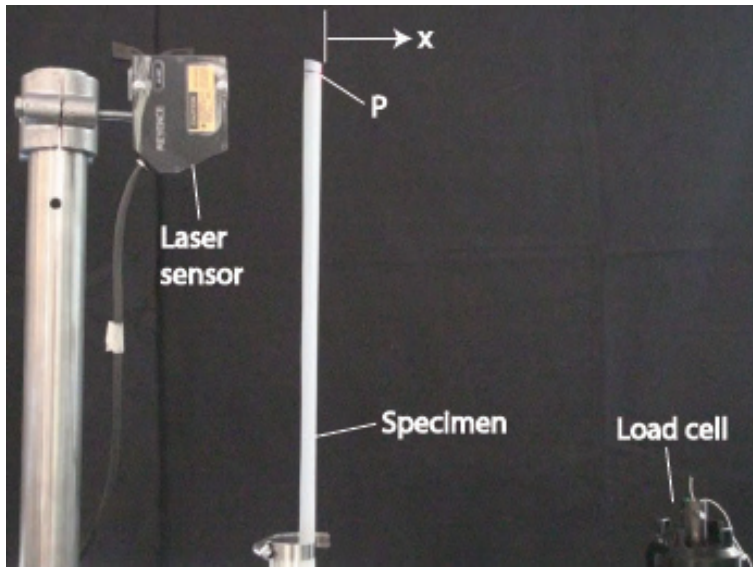
Figure 4.10. Deployment test configuration.

4.4   Finite Element Analysis

Bending of open cylindrical shells is a highly nonlinear phenomenon. To investigate their nonlinear behavior including the effects of rate and temperature in the present problem, we employ the finite element method with a linear viscoelastic constitutive model for the shell. The analysis is conducted with Abaqus/Standard using experimentally determined viscoelastic properties for the material under study.
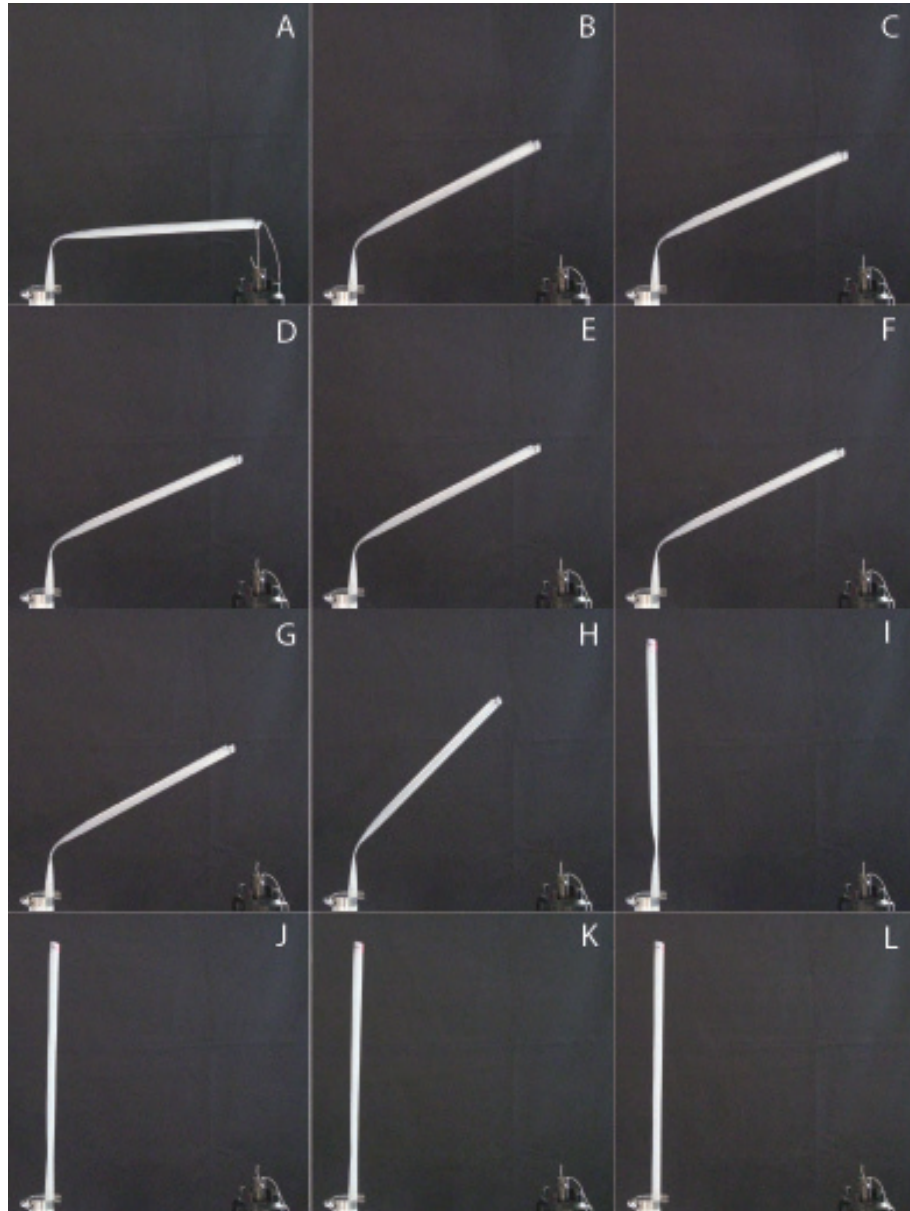
Figure 4.11. Deployment sequence: (A)-(F) from 0 s to 2.5 s in steps of 0.5 s, (G)-(I): from 5 s to 55 s in steps of 25 s, and (J)-(L): from 1000 s to 3000 s in steps of 1000 s.
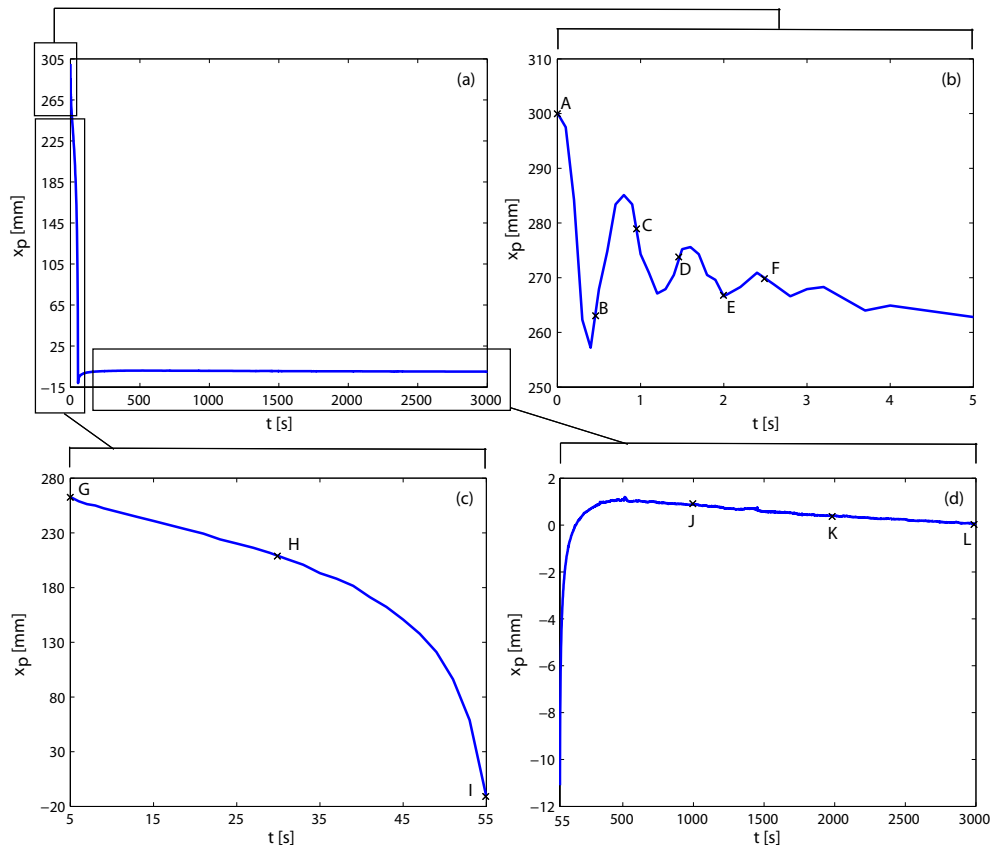
Figure 4.12. Measured lateral displacement of point P during deployment.

4.4.1 Finite Element Model

The two shells tested in Section 4.3 were modeled as cylindrical surfaces as shown in Figure 4.13. The model dimensions are as defined in Table 4.1. Thickness variation was included in the model by specifying the thickness of each element. The thickness at all node positions was first determined from the measured distribution, with spline interpolation, and then within each element, the thickness was linearly interpolated from its node values.

For simulating the folding-stowage experiment in Section 4.3.2, a mesh with 6800 quadrilateral shell elements S4 with a maximum dimension of 2 mm was used. The mesh density in the circumferential direction was twice that in the longitudinal direction for precise computation of the localized fold. Displacement boundary conditions were defined on two nodes A and B, one on each end section of the shell and coinciding with the mid-point of the cross section. All the translational degrees of freedom of node B were constrained and gravity load was defined to act in the positive z direction throughout the analysis. A quasi-static analysis was carried out in two steps, as follows. During the folding step, a displacement u_z of 80 mm was imposed on node A, at the same rates and temperatures used in the experiments. In the stowage step, the degrees of freedom of node A take their values at the end of the folding step and were held constant for 5000 s. The accuracy of integration in quasi-static analysis was controlled by specifying the tolerance parameter *CETOL which puts a limit on the maximum change in creep strain rate allowed over a time increment. A value of 1×10^{-4} was found to be adequate for obtaining accurate solutions.

The deployment-recovery test in Section 4.3.3 was analyzed using a mesh with 2500 elements and a maximum dimension of 4 mm. For this simulation, all nodes on the section CC' was fixed. The analysis steps were carried out as follows. In the folding step, a displacement u_x of 300 mm was imposed over 9 s to node A. The degrees of freedom of node A remained unchanged for 983 s in the stowage step. These two steps were carried out quasi-statically. The degrees of freedom at node A were instantaneously removed at the end of stowage. The analysis was run for 3000 s with a dynamic analysis procedure.
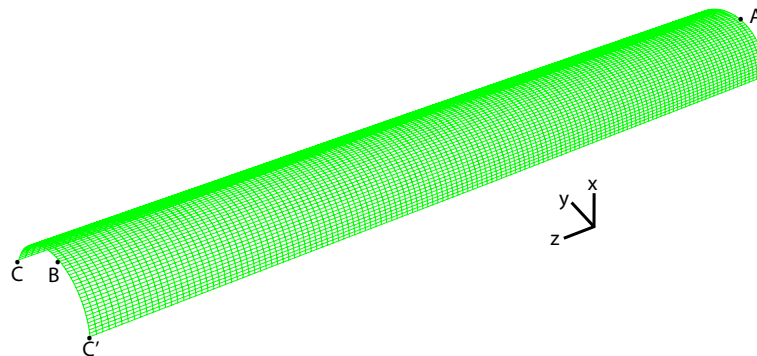
Figure 4.13. Finite element model.

i	E_i [MPa]	ρ_i [s]
∞	136.2	——
1	150.6	2.43×10^{-2}
2	74.81	2.17×10^{-1}
3	68.26	1.52
4	65.22	1.24×10
5	62.85	1.49×10^2
6	49.83	1.69×10^3

Table 4.2. Prony series parameters for LDPE master curve.

4.4.2   Constitutive Model

The uniaxial constitutive equation for linear viscoelastic material is

$$\sigma(t) = \int_0^t E(t' - s') \frac{d\epsilon(s)}{ds} ds, \tag{4.1}$$

where σ is stress, ϵ is strain, E is the relaxation modulus, t' and s' are reduced times defined as

$$t' = \int_0^t \frac{du}{a_T(T)} \quad \text{and} \quad s' = \int_0^s \frac{du}{a_T(T)}. \tag{4.2}$$

The relaxation modulus is represented by a Prony series as

$$E(t) = E_\infty + \sum_{i=1}^n E_i e^{-(t/\rho_i)}, \tag{4.3}$$

where t is time, E_∞ is the long term modulus, E_i are the Prony coefficients, and ρ_i are the relaxation times. The temperature shift factor is expressed by the Williams-Landel-Ferry (WLF) equation,

$$\log a_T = -\frac{c_1(T - T_0)}{c_2 + (T - T_0)}, \tag{4.4}$$

in which c_1 and c_2 are material constants that depend on the particular polymer and the logarithm is of base ten.

The material properties of LDPE were characterized through a series of tensile relaxation tests on rectangular test coupons that had been subject to the same thermal cycle as the shell specimens. Figure 4.14 shows the relaxation modulus master curve of LDPE at the reference temperature. Table 4.2 summarizes the Prony series parameters. The material constants c_1 and c_2 were determined to be

$$c_1 = -8.74 \quad \text{and} \quad c_2 = -40.41.$$
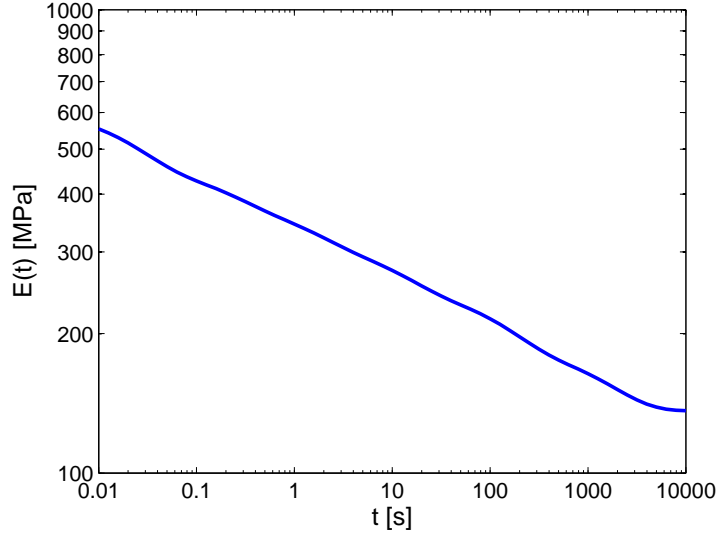
Figure 4.14. Master curve for LDPE at 22°C.

Implementation of viscoelastic behavior in Abaqus/Standard requires the specification of shear and bulk moduli, which are related to the uniaxial modulus through the equations

$$G(t) = \frac{E(t)}{2(1+\nu)}, \tag{4.5}$$

$$K(t) = \frac{E(t)}{3(1-2\nu)}, \tag{4.6}$$

where ν is the Poisson's ratio, G is the shear modulus and K is the bulk modulus. A Poisson's ratio of 0.49 was determined from relaxation tests and this value was assumed to be constant in the present study. This assumption implicitly leads to the condition that bulk and shear moduli are synchronous (Hilton, 2001). In general, this is not a realistic description for most materials, however, as shown in Section 4.5, this condition does not seem to have a significant effect on the behavior of the shell.

4.4.3 Results

The evolution of the stress distributions over time can be studied with the finite element model. The longitudinal bending stress on the outer shell surface in folding at $T = 22$°C and $\dot{u} = 1$ mm/s is shown in Figure 4.15. The shell has a relatively uniform stress state with tension on the longitudinal edges. After the instability is initiated, the longitudinal bending stress starts localizing in the middle of the shell with increasing variation in stress between the edges and the center. The buckle subsequently spreads transversely to form a complete fold, which is in uniform compression but rises

rapidly to tension towards the edges. The longitudinal bending stress reduces away from the fold as localization takes place.

Stress relaxation in the stowed state is evidenced in Figure 4.16, which plots the longitudinal stress at the beginning and the end of the stowage period. The longitudinal bending stress on the outer shell surface decreases drops over time. At the same time, the fold region slightly extends in the longitudinal direction. A reduction in the longitudinal curvature of the fold is also predicted by the simulation as the fold region increases in length.

Three deformed shapes with their corresponding stress gradients during deployment are shown in Figure 4.17. In the steady deployment phase, the arclength of the fold reduces while the transverse curvature remains zero. This process is the reverse of buckle propagation during folding. As the shell passes through the position with $x_p = 0$ and overshoots, the longitudinal bending stress on the two edges gradually reduces to zero. The longitudinal curvature is practically zero after the overshoot and the remaining part of the deployment is controlled by the transverse curvature recovery in the fold. The fold stays stationary throughout the entire deployment, which agrees with experimental observation.
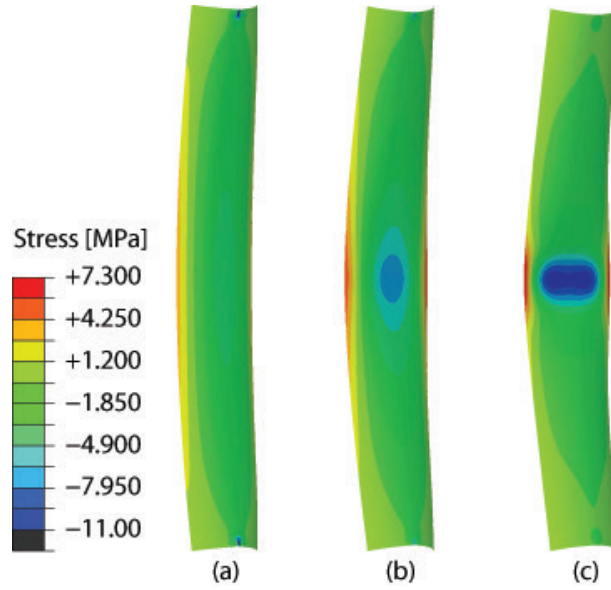
Figure 4.15. Longitudinal bending stress on the outer shell surface: (a) during initial uniform bending, (b) after instability is initiated and (c) as buckle develops.

4.5   Results Comparison

Results from analysis and experiments are compared for the folding, stowage, deployment, and recovery processes. The calculated load versus time responses during folding for the case of $\dot{u} =$
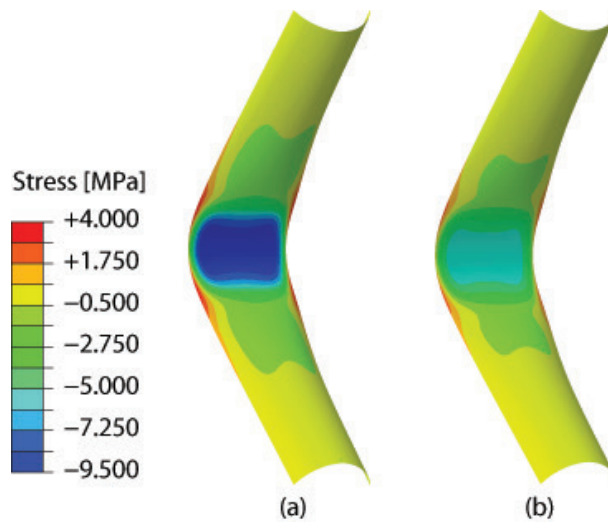
Figure 4.16. Relaxation of longitudinal bending stress on the outer shell surface: (a) beginning of stowage and (b) end of stowage.
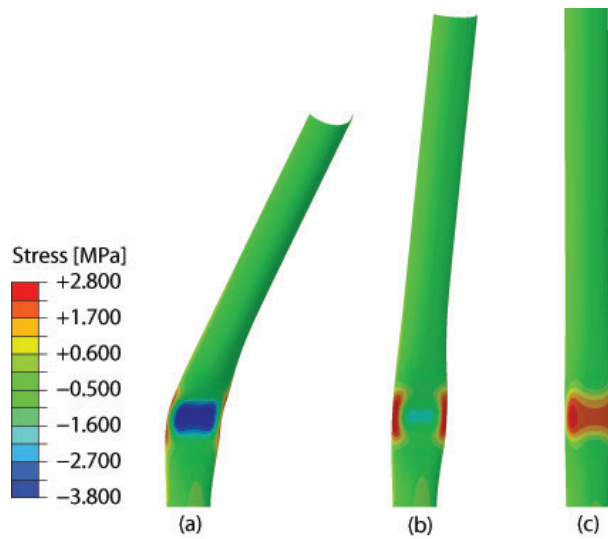
Figure 4.17. Longitudinal bending stress on the outer shell surface: (a) steady deployment (b) passing through the $x_p = 0$ position and (c) overshoot.

1 mm/s is plotted along with the corresponding experimental measurements in Figure 4.18. The predicted response is found to be in good agreement with the observed response in all aspects. The initial stiffness, onset of limit load instability, and postbuckling load plateau are well reproduced. Minor discrepancies are found for the calculation of the buckling load, which are overpredicted by 0.9 N and 0.3 N for temperatures of 15°C and 22°C respectively. The errors are likely due to other forms of geometric imperfections not characterized in the study, such as non-uniformity of the cross section shape along the length of the shell. The discrepancies are however insignificant in magnitude.

Four deformed configurations of the shell in the folding stage from experiments and analysis are compared in Figure 4.19. Both the evolution of the overall deformed geometry and the localized fold are closely captured as seen in this qualitative comparison. Load relaxation responses in the stowed configuration for the folding rate of $\dot{u} = 1$ mm/s are plotted in Figure 4.20. The agreement of the predicted and measured responses indicates the accuracy of the finite element model in long term simulations.

The lateral displacement x_p during deployment of the shell are compared in Figure 4.21. All features of the response have been reproduced by the analysis with minor discrepancies. In the initial dynamic phase shown in Figure 4.21(a), the predicted oscillations are essentially over in 4 s, which end earlier than the measured response. Slightly larger discrepancy is found in the steady deployment phase shown in Figure 4.21(b), where the simulation overpredicts the overshoot by 20 mm, occurring about 2.5 s earlier than in the experiment. Nonetheless, the long term creep recovery is reasonably well predicted, as shown in Figure 4.21(c). The discrepancy is less than 1 mm by the end of the simulation at 3000 s. A comparison of the deployed shapes is shown in Figure 4.22, which demonstrates good correlation in the dynamics of the fold. The main source of discrepancy is believed to be variations in environmental conditions in the deployment experiments.
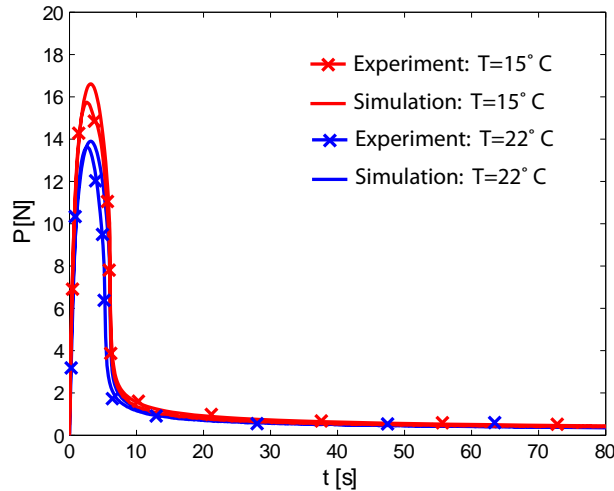
Figure 4.18. Comparison of load vs. time during folding, for $\dot{u} = 1$ mm/s.
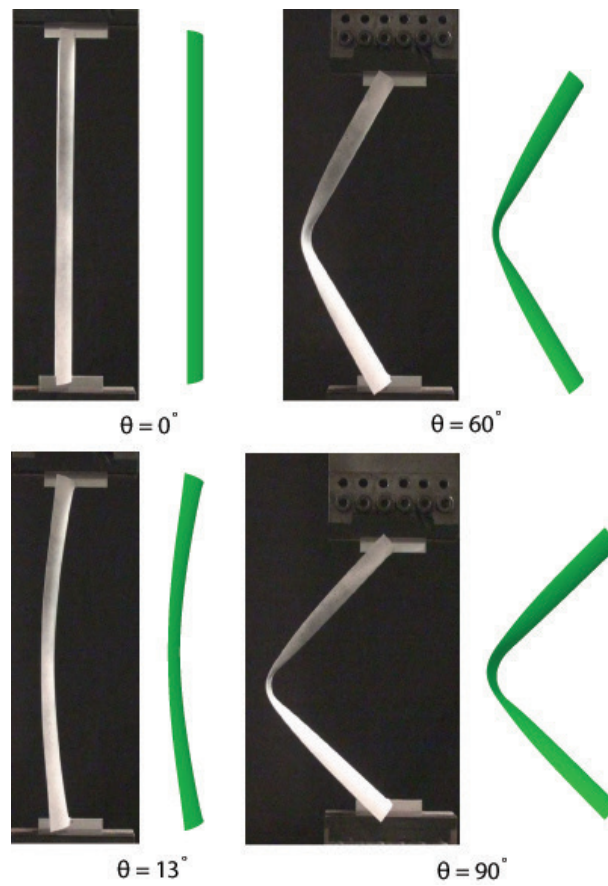
Figure 4.19. Comparison of deformed shapes during folding and stowage.
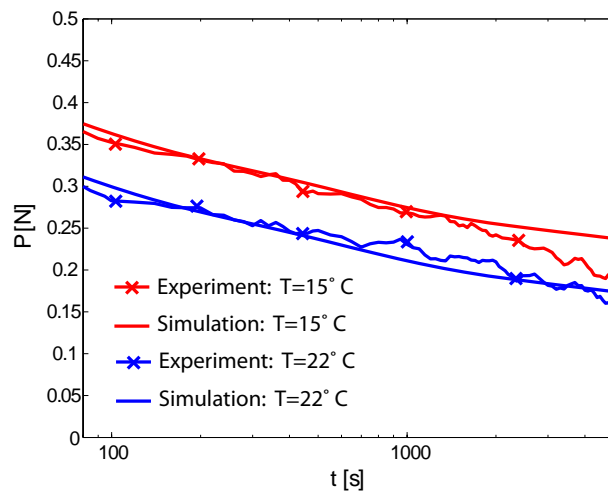
Figure 4.20. Comparison of load vs. time during stowage, for $\dot{u} = 1$ mm/s.
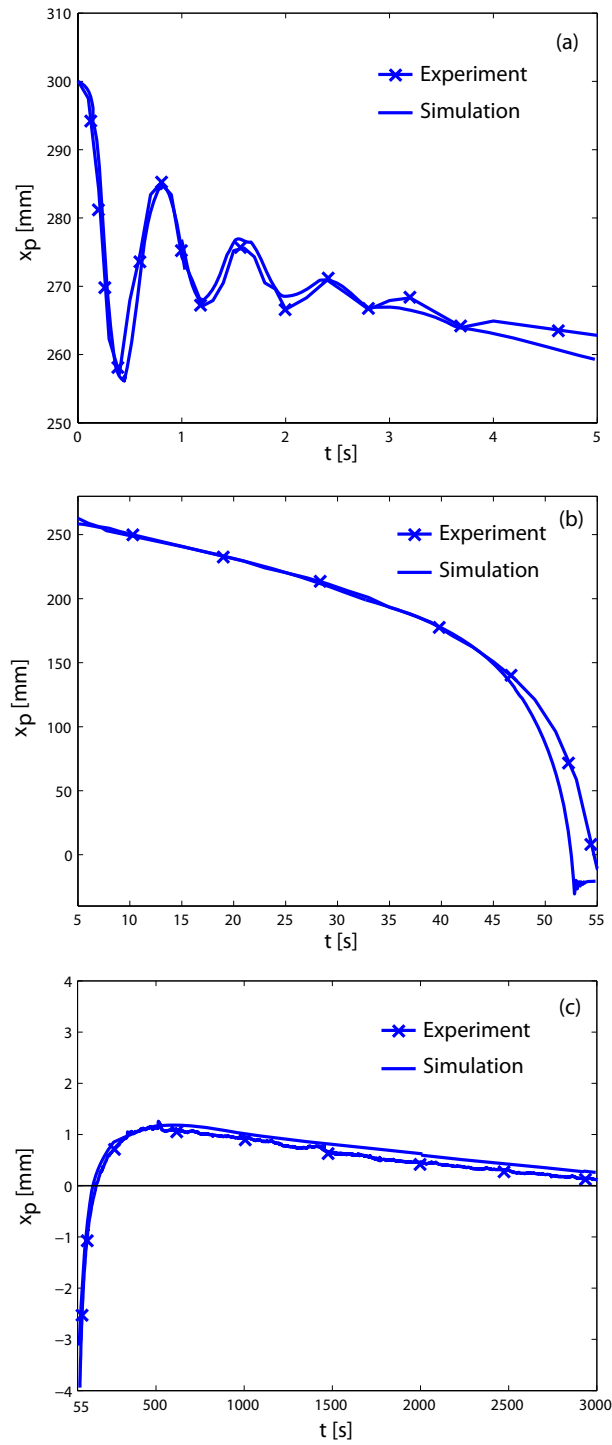
Figure 4.21. Comparison of lateral displacement of shell free end: (a)transient dynamic response, (b) steady deployment and (c) long term creep recovery.
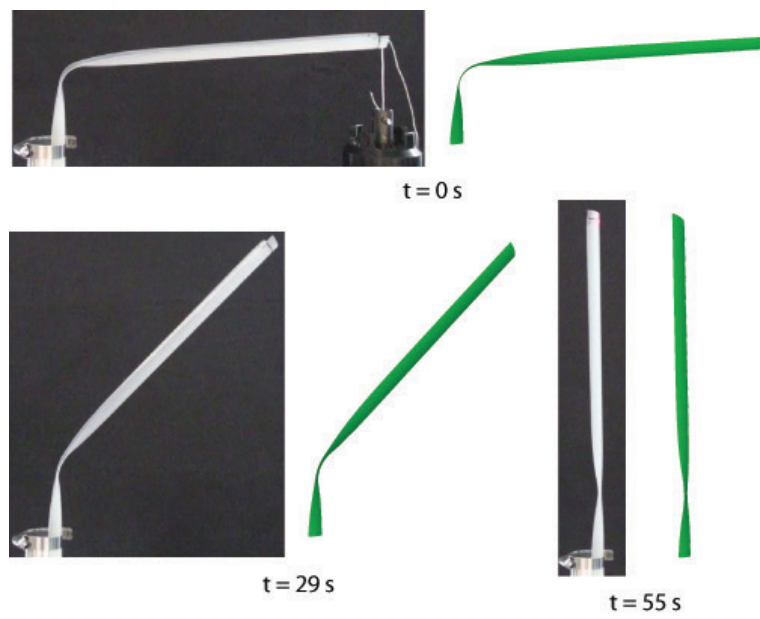
Figure 4.22. Comparison of deployed shapes.

Chapter 5

Deployment and Shape Recovery of Composite Shells

5.1 Introduction

The general features of stowage effects have been identified in Chapters 3 and 4 by studying homogeneous beams and shells. This chapter develops micromechanical modeling techniques for viscoelastic composite shells and applies these models to a composite deployable structure.

Viscoelastic behavior of composite deployable structures has started to be addressed only recently. While experimental results on recovery time and vibration characteristics of composite tubes after stowage have been reported (Domber et al., 2002; Soykasap, 2009), a general method of analysis is lacking. A detail material model that accurately computes viscoelastic composite properties can effectively guide the design process of composite deployable structures.

This chapter presents a detailed study of a particular structure that poses the general challenges typical of thin-walled deployable structures with viscoelastic properties. The particular structure selected is a composite tape-spring made of epoxy matrix reinforced with plain-weave woven carbon fabric. Tape-springs are thin shells with curved section, typically of uniform curvature and subtending an angle typically smaller than 180°, Figure 5.1. This structural form can be folded by forming a local buckle and is therefore routinely employed as self-deployable hinges on spacecraft. In the current study, carefully controlled experiments on deployment and shape recovery of composite tape-springs are presented along with numerical predictions using a finite-element based micromechanical model for thin composites consisting of linear viscoelastic matrix and linear elastic fibers.

5.2 Background

In the area of micromechanical modeling of viscoelastic composites, many analytical approaches were proposed for determining the viscoelastic moduli of unidirectional composites from constituent
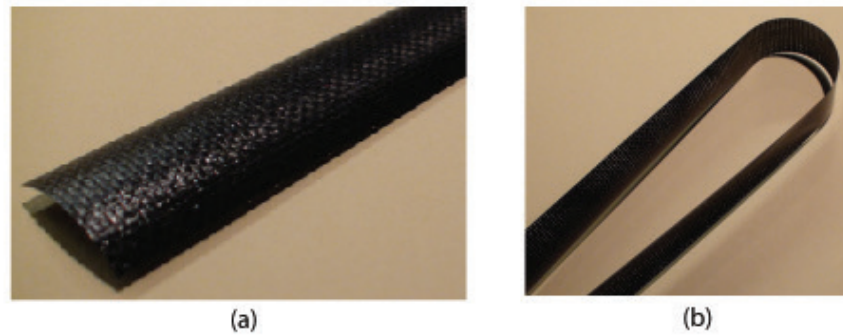
Figure 5.1. Composite tape-spring: (a) deployed and (b) folded.

fiber and matrix properties. The underlying approach is to extend existing micromechanical models for elastic composites to viscoelastic composites by exploiting the elastic-viscoelastic correspondence principle (Hashin, 1965 1966). Viscoelastic moduli were also obtained numerically through direct finite element analysis (Brinson and Knauss, 1992) assuming a uniform distribution of fibers.

For woven composites, Govindarajan et al. (1996) and Shrotriya and Sottos (2005) considered analytical models based on simplified weave geometries, but the flexural deformation of the fiber tows was not accounted for and was believed to be the source of significant discrepancy between predicted and measured viscoelastic responses. Predictions were improved when two-dimensional (Shrotriya and Sottos, 2005) and three-dimensional (Zhu et al., 2003) finite element based methods were utilized to incorporate the influence of weave geometry. However, only in-plane properties were considered in these studies.

5.3   Micromechanical Modeling

The effective viscoelastic response of a woven composite lamina consisting of elastic carbon fibers embedded in a viscoelastic epoxy matrix depends on factors such as the matrix relaxation moduli, weave geometry and tow size. To model material and geometric effects at lower length scales, a finite element homogenization approach is proposed in the present study. In particular, homogenization of the viscoelastic properties is carried out both at the tow level and at the lamina level using the properties of its constituents. A woven composite made from ± 45 plain-weave fabric with 1 k tows of T300 carbon fibers impregnated with PMT-F4 epoxy resin is assumed. The unit cell finite element analyses are carried out in the commercial package Abaqus/Standard.

5.3.1 Constituent Properties

The epoxy matrix is treated as an isotropic, linear viscoelastic solid and its time and temperature dependent mechanical properties are modeled using a Prony series. The Prony series representation of the relaxation modulus is written as

$$E(t) = E_\infty + \sum_{i=1}^{n} E_i e^{-(t/\rho_i)}, \tag{5.1}$$

where t is time, E_∞ is the long term modulus, E_i are the Prony coefficients, and ρ_i are the relaxation times. The temperature shift factor is expressed in terms of the Williams-Landel-Ferry (WLF) equation,

$$\log a_T = -\frac{c_1(T - T_0)}{c_2 + (T - T_0)}, \tag{5.2}$$

in which c_1 and c_2 are material constants that depend on the particular polymer and the logarithm is of base ten.

The material properties of PMT-F4 epoxy were characterized through a series of tensile creep tests on rectangular test coupons with a length of 100 mm, a width of 12.7 mm, and a thickness of 3.2 mm. The epoxy specimens were made by curing neat PMT-F4 resin under vacuum at 120°C and 400 kPa for 2 hours. Tensile creep tests were conducted at temperatures ranging from 20°C to 90°C, with 10°C intervals. Figure 5.2 shows the relaxation modulus master curve of PMT-F4 at the reference temperature of $T_0 = 40$°C. Table 5.1 lists the Prony series parameters. A Poisson's ratio of 0.33 was determined from relaxation tests and this value was assumed to be constant in the present study. The material constants c_1 and c_2 were determined to be

$$c_1 = 28.3816 \quad \text{and} \quad c_2 = 93.291.$$

Carbon fibers are regarded as a transversely isotropic elastic solid (Daniel and Ishai, 2006). The T300 carbon fibers were manufactured by Cytec Industries Inc. The mechanical properties of T300 fibers obtained from the manufacturer are listed in Table 5.2.

5.3.2 Viscoelastic Behavior of Tows

The viscoelastic properties of a straight and transversely isotropic fiber tow were determined from the constituent properties by direct finite element analysis of a unit cell. This approach was first adopted by Brinson and Knauss (1992) to compute the effective viscoelastic properties of a unidirectional fiber composite. Using a two-dimensional unit cell finite element analysis, they determined the plain-strain relaxation modulus. In the present work, the unit cell is treated as a three dimensional
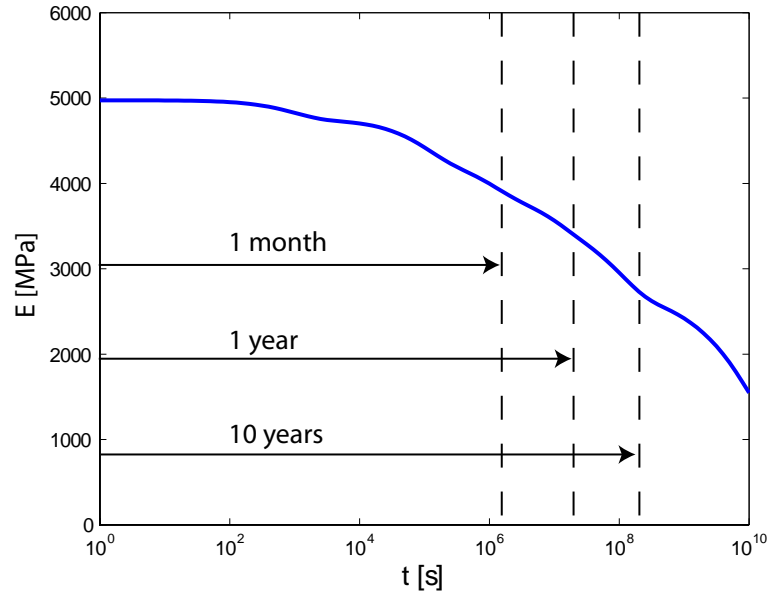
Figure 5.2. Master curve of PMT-F4 at a reference temperature of $T_0 = 40°C$.

i	$E_i \ [MPa]$	$\rho_i \ [s]$
∞	1000	——
1	224.1	$1.0e+3$
2	450.8	$1.0e+5$
3	406.1	$1.0e+6$
4	392.7	$1.0e+7$
5	810.4	$1.0e+8$
6	203.7	$1.0e+9$
7	1486.0	$1.0e+10$

Table 5.1. Relaxation times and relaxation coefficients for PMT-F4.

Properties	Value
$E_1 \ [MPa]$	$233,000$
$E_2 \ [MPa]$	$23,100$
$G_{12} \ [MPa]$	$8,963$
ν_{12}	0.2
ν_{23}	0.4

Table 5.2. Elastic properties of T300 carbon fibers.

continuum solid and all effective viscoelastic moduli characterizing a transversely isotropic solid are computed. The generality of the current computational scheme is necessary for multi-scale unit cell homogenization.

The cross section of a representative tow is shown in Figure 5.3, from which the fiber diameter and volume fraction were determined to be $d_f = 7.0~\mu m$ and $v_f = 0.64$ respectively. The unit cell model is composed of a single fiber surrounded by matrix, which implicitly assumes a square array fiber arrangement. Hexagonal array and random array fiber arrangements were also implemented, but the difference between these configurations was found to be insignificant at this volume fraction.

The particular finite element model shown in Figure 5.4 is a cube with edge length of $\ell = 7.7~\mu m$ and is composed of 16800 8-node brick elements (C3D8) and 800 6-node triangular prism elements (C3D6). The material properties defined in Section 5.3.1 were assigned to the fiber and matrix elements accordingly. Periodic displacement boundary conditions were enforced between each pair of opposite boundary faces of the unit cell through the following constraint equations in terms of normal and shear strains of a homogeneous continuum solid:

$$u(\frac{\ell}{2}, y, z) - u(-\frac{\ell}{2}, y, z) = \epsilon_1 \ell \tag{5.3}$$

$$v(\frac{\ell}{2}, y, z) - v(-\frac{\ell}{2}, y, z) = \epsilon_6 \ell \tag{5.4}$$

$$w(\frac{\ell}{2}, y, z) - w(-\frac{\ell}{2}, y, z) = \epsilon_5 \ell \tag{5.5}$$

$$u(x, \frac{\ell}{2}, z) - u(x, -\frac{\ell}{2}, z) = \epsilon_6 \ell \tag{5.6}$$

$$v(x, \frac{\ell}{2}, z) - v(x, -\frac{\ell}{2}, z) = \epsilon_2 \ell \tag{5.7}$$

$$w(x, \frac{\ell}{2}, z) - w(x, -\frac{\ell}{2}, z) = \epsilon_4 \ell \tag{5.8}$$

$$u(x, y, \frac{\ell}{2}) - u(x, y, -\frac{\ell}{2}) = \epsilon_5 \ell \tag{5.9}$$

$$v(x, y, \frac{\ell}{2}) - v(x, y, -\frac{\ell}{2}) = \epsilon_4 \ell \tag{5.10}$$

$$w(x, y, \frac{\ell}{2}) - w(x, y, -\frac{\ell}{2}) = \epsilon_3 \ell, \tag{5.11}$$

where u, v, and w denote displacements in the x, y, and z directions respectively, and ϵ denotes strains expressed in Voigt notation.

The constitutive equation for a homogenized transversely isotropic solid with the coordinate directions defined in Figure 5.4 is written as

$$[\sigma(t)] = \int_0^t \Big([C(t-s)] [\dot{\epsilon}(s)] \Big) ds, \tag{5.12}$$

where $[\sigma(t)]$, $[C(t)]$, and $[\epsilon(t)]$ are respectively written as

$$[\sigma(t)] = \begin{bmatrix} \sigma_1(t) \\ \sigma_2(t) \\ \sigma_3(t) \\ \sigma_4(t) \\ \sigma_5(t) \\ \sigma_6(t) \end{bmatrix}, \tag{5.13}$$

$$C(t) = \begin{bmatrix} C_{11}(t) & C_{12}(t) & C_{12}(t) & 0 & 0 & 0 \\ C_{12}(t) & C_{22}(t) & C_{23}(t) & 0 & 0 & 0 \\ C_{12}(t) & C_{23}(t) & C_{22}(t) & 0 & 0 & 0 \\ 0 & 0 & 0 & C_{44}(t) & 0 & 0 \\ 0 & 0 & 0 & 0 & C_{55}(t) & 0 \\ 0 & 0 & 0 & 0 & 0 & C_{55}(t) \end{bmatrix}, \tag{5.14}$$

$$[\sigma(t)] = \begin{bmatrix} \epsilon_1(t) \\ \epsilon_2(t) \\ \epsilon_3(t) \\ \epsilon_4(t) \\ \epsilon_5(t) \\ \epsilon_6(t) \end{bmatrix}. \tag{5.15}$$

Because of transverse isotropy, the matrix $C(t)$ has only five independent terms, which are C_{11}, C_{22}, C_{12}, C_{23}, and C_{55}. The term C_{44} is related to C_{22} and C_{23} by

$$C_{44}(t) = \frac{C_{22}(t) - C_{23}(t)}{2}. \tag{5.16}$$

The minimum number of analyses needed to compute the independent time-varying functions in $C(t)$ is three because each analysis provides more than one function. In the present work, four analyses were conducted to determine all the functions without invoking Equation (5.16). In each analysis, a unit amplitude of one of the strain variables, ϵ_1, ϵ_2, ϵ_4, and ϵ_5, was applied to the unit cell in the form of a step function and the corresponding stresses were obtained as functions of time. Each entry in the $C(t)$ matrix was modeled by a Prony series having the same relaxation times as the matrix. The Prony coefficients were determined by numerical fitting using the computed stresses. The results are plotted with respect to time in Figure 5.5.
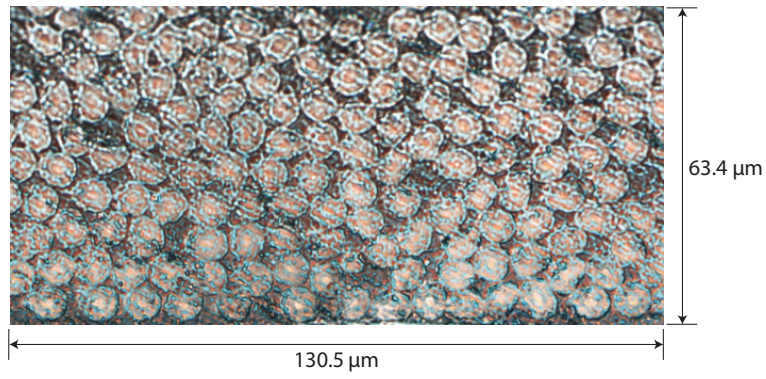
Figure 5.3. Cross section of a tow.
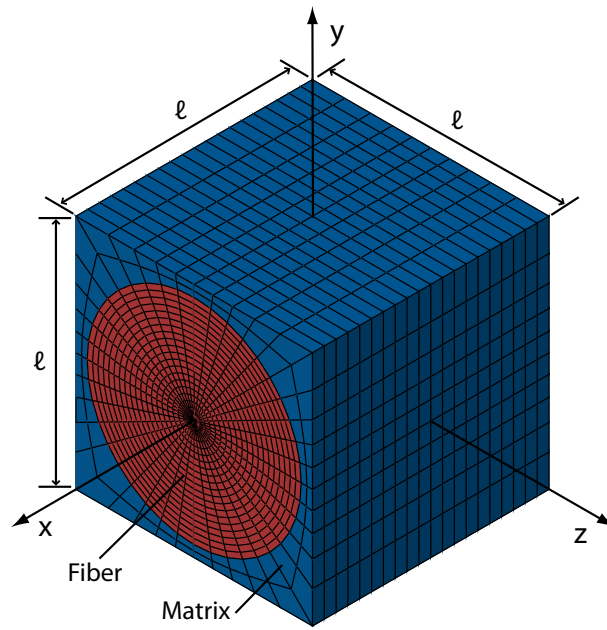
Figure 5.4. Finite element model for unidirectional fiber tow unit cell.
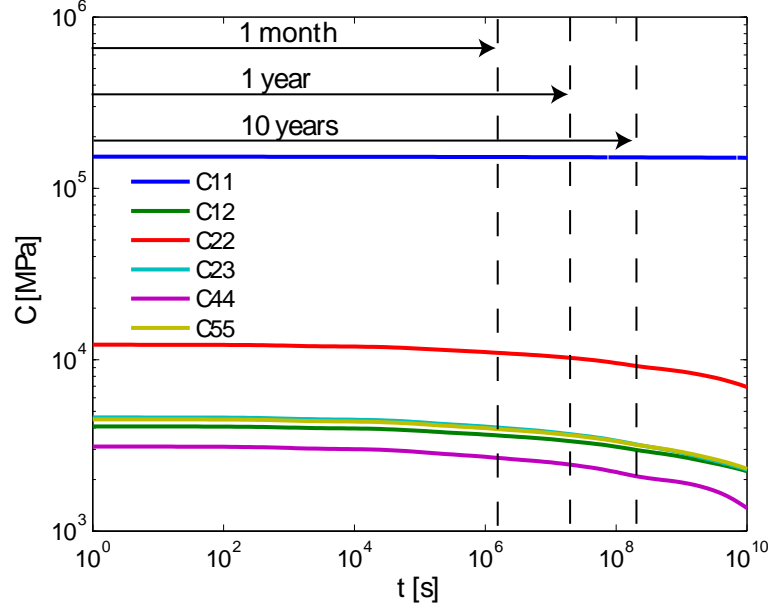
Figure 5.5. Viscoelastic properties of unidirectional fiber tow.

5.3.3 Viscoelastic Properties of Laminas

A single plain-weave composite lamina is modeled as a Kirchhoff plate consisting of viscoelastic tows and matrix. The cross section of the lamina is shown in Figure 5.6. The geometric properties of the lamina were measured from photomicrographs of several different cross sections. The lamina is characterized by a weave length of $L = 3.5$ mm, a maximum tow thickness of $h = 0.063$ mm, a tow width of $w = 1.05$ mm, and a tow-to-tow spacing of $g = 0.7$ mm. The overall fiber volume fraction was calculated to be $\nu_f = 0.52$ from weight of cured lamina and resin.

The lamina unit cell model is composed of four tows with gaps filled with pure matrix as shown in Figure 5.7. The unit cell was constructed by combining four identical bundles with different orientations in space. Each bundle consisted of a tow and pure matrix. The boundary surfaces of a bundle were defined by sinusoidal functions. For example, the boundaries of the bundle in Figure 5.7(a) are given by

$$z = \pm \frac{h}{2} sin\left(\frac{2\pi x}{L}\right) + \frac{h}{2} sin\left(\frac{2\pi y}{L}\right). \tag{5.17}$$

The remaining bundles were created by rotating this bundle by increments of 90° around the origin. This representation provides an exact geometric between all tows in the lamina.

Each tow consists of 960 8-node brick elements (C3D8) and the matrix is made up of 1920 8-node brick (C3D8) and 640 6-node triangular prism elements (C3D6). The material properties for the tows were defined by the relaxation moduli obtained in Section 5.3.2 through a user defined

material subroutine (UMAT). To impose the Kirchhoff constraint, nodes lying on the boundary faces of the unit cell were tied to nodes in the mid-plane through rigid connections. The displacements and rotations of each mid-plane node on one face were paired to the corresponding node on the opposite face by constraint equations that impose periodic boundary conditions in terms of mid-plane strains and out-of-plane curvatures of a homogenized Kirchhoff plate. The kinematic relations for a Kirchhoff plate are

$$\epsilon_x = \frac{\partial u}{\partial x} \tag{5.18}$$

$$\epsilon_y = \frac{\partial v}{\partial y} \tag{5.19}$$

$$\gamma_{xy} = \frac{\partial u}{\partial y} + \frac{\partial v}{\partial x} \tag{5.20}$$

$$\kappa_x = -\frac{\partial^2 w}{\partial x^2} \tag{5.21}$$

$$\kappa_y = -\frac{\partial^2 w}{\partial y^2} \tag{5.22}$$

$$\kappa_{xy} = -2\frac{\partial^2 w}{\partial x \partial y}. \tag{5.23}$$

The displacement constraints that impose periodic boundary conditions are written as

$$u(\frac{L}{2}, y) - u(-\frac{L}{2}, y) = \epsilon_x L \tag{5.24}$$

$$v(\frac{L}{2}, y) - v(-\frac{L}{2}, y) = \frac{1}{2}\gamma_{xy} L \tag{5.25}$$

$$w(\frac{L}{2}, y) - w(-\frac{L}{2}, y) = -\frac{1}{2}\kappa_{xy} y L \tag{5.26}$$

$$\theta_x(\frac{L}{2}, y) - \theta_x(-\frac{L}{2}, y) = -\frac{1}{2}\kappa_{xy} L \tag{5.27}$$

$$\theta_y(\frac{L}{2}, y) - \theta_y(-\frac{L}{2}, y) = \kappa_x L \tag{5.28}$$

$$\theta_z(\frac{L}{2}, y) - \theta_z(-\frac{L}{2}, y) = 0 \tag{5.29}$$

$$u(x, \frac{L}{2}) - u(x, -\frac{L}{2}) = \frac{1}{2}\gamma_{xy} L \tag{5.30}$$

$$v(x, \frac{L}{2}) - v(x, -\frac{L}{2}) = \epsilon_y L \tag{5.31}$$

$$w(x, \frac{L}{2}) - w(x, -\frac{L}{2}) = -\frac{1}{2}\kappa_{xy} x L \tag{5.32}$$

$$\theta_x(x, \frac{L}{2}) - \theta_x(x, -\frac{L}{2}) = -\kappa_y L \tag{5.33}$$

$$\theta_y(x, \frac{L}{2}) - \theta_y(x, -\frac{L}{2}) = \frac{1}{2}\kappa_{xy}L \tag{5.34}$$

$$\theta_z(x, \frac{L}{2}) - \theta_z(x, -\frac{L}{2}) = 0, \tag{5.35}$$

where θ are rotations and the subscripts denote the rotation directions.

The constitutive relationships for the homogenized plate are written as

$$[N(t)] = \int_0^t \Big([A(t-s)][\dot{\epsilon}(s)] + [B(t-s)][\dot{\kappa}(s)] \Big) ds, \tag{5.36}$$

$$[M(t)] = \int_0^t \Big([B(t-s)][\dot{\epsilon}(s)] + [D(t-s)][\dot{\kappa}(s)] \Big) ds, \tag{5.37}$$

where $[N]$ and $[M]$ denote force and moment resultants given by

$$[N(t)] = \begin{bmatrix} N_x(t) \\ N_y(t) \\ N_{xy}(t) \end{bmatrix}, \tag{5.38}$$

$$[M(t)] = \begin{bmatrix} M_x(t) \\ M_y(t) \\ M_{xy}(t) \end{bmatrix}. \tag{5.39}$$

The variables $[\epsilon]$ and $[\kappa]$ denote mid-plane strains and out-of-plane curvatures written as

$$[\epsilon(t)] = \begin{bmatrix} \epsilon_x(t) \\ \epsilon_y(t) \\ \epsilon_{xy}(t) \end{bmatrix}, \tag{5.40}$$

$$[\kappa(t)] = \begin{bmatrix} \kappa_x(t) \\ \kappa_y(t) \\ \kappa_{xy}(t) \end{bmatrix}. \tag{5.41}$$

The matrices $[A]$, $[B]$ and $[D]$ represent the in-plane stiffness, stretching-bending coupling, and bending stiffness matrices. They are combined to give the ABD stiffness matrix,

$$ABD(t) = \left[\begin{array}{ccc|ccc} A_{xx}(t) & A_{xy}(t) & A_{xs}(t) & B_{xx}(t) & B_{xy}(t) & B_{xs}(t) \\ A_{yx}(t) & A_{yy}(t) & A_{ys}(t) & B_{yx}(t) & B_{yy}(t) & B_{ys}(t) \\ A_{sx}(t) & A_{sy}(t) & A_{ss}(t) & B_{sx}(t) & B_{sy}(t) & B_{ss}(t) \\ \hline B_{xx}(t) & B_{xy}(t) & B_{xs}(t) & D_{xx}(t) & D_{xy}(t) & D_{xs}(t) \\ B_{yx}(t) & B_{yy}(t) & B_{ys}(t) & D_{yx}(t) & D_{yy}(t) & D_{ys}(t) \\ B_{sx}(t) & B_{sy}(t) & B_{ss}(t) & D_{sx}(t) & D_{sy}(t) & D_{ss}(t) \end{array} \right]. \tag{5.42}$$

Similar to the homogenization procedure conducted for the fiber tows, each entry in the $ABD(t)$ matrix was modeled by a Prony series having the same relaxation times as the matrix. Six separate analyses, each corresponding to a unit amplitude of the six deformation variables (ϵ_x, ϵ_x, ϵ_{xy}, κ_x, κ_x, κ_{xy}), were conducted to determine all the entries. The following ABD matrix was obtained:

$$
ABD(t) = \left[
\begin{array}{ccc|ccc}
A_{xx}(t) & A_{xy}(t) & 0 & 0 & 0 & 0 \\
A_{xy}(t) & A_{xx}(t) & 0 & 0 & 0 & 0 \\
0 & 0 & A_{ss}(t) & 0 & 0 & 0 \\
\hline
0 & 0 & 0 & D_{xx}(t) & D_{xy}(t) & 0 \\
0 & 0 & 0 & D_{xy}(t) & D_{xx}(t) & 0 \\
0 & 0 & 0 & 0 & 0 & D_{ss}(t)
\end{array}
\right] ,
\tag{5.43}
$$

where the non-zero entries are plotted with respect to time in Figure 5.8 and Figure 5.9. It is observed that $A_{xx} = A_{yy}$ and $D_{xx} = D_{yy}$ because the fill and warp tows have identical properties. Because $A_{xs} = A_{ys} = 0$, stretching and shearing are decoupled. Similarly, bending and twisting are also decoupled as $D_{xs} = D_{ys} = 0$. Note that $[B] = 0$, which suggests that there is no coupling between in-plane and out-of-plane behavior. The plain-weave lamina has stiffness properties resembling that of a symmetric crossply composite.
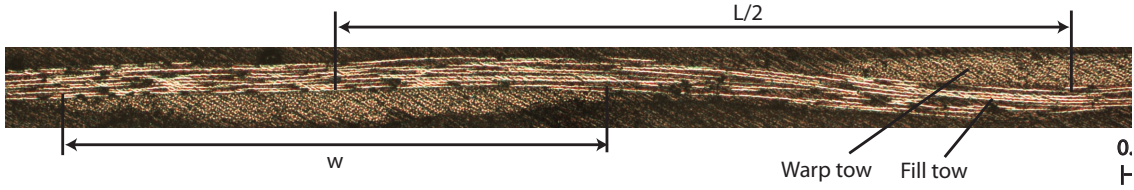
Figure 5.6. Cross section geometry of a plain-weave lamina. Warp and fill tows are perpendicular and parallel to the page respectively.

5.3.4 Model Validation

The homogenized viscoelastic model of Section 5.3.3 was verified by performing tension and four-point bending creep tests on single-ply ±45 laminas. Tension tests were carried out on a specimen with a length of 100 mm and a width of 20 mm. For bending tests, a 100 mm long and 50 mm wide specimen was used. Both tests were done at the temperatures of 50°C, 60°C, and 70°C. Each type of test was done twice.

The average axial and bending compliances at a 45° angle from the tow direction were obtained from the two tests conducted. The data from different temperatures were shifted to the reference temperature of 40°C and plotted in Figures 5.10 and 5.11. The model predictions were obtained by running uniaxial tension and bending creep analyses on the plain-weave lamina unit cell. The com-
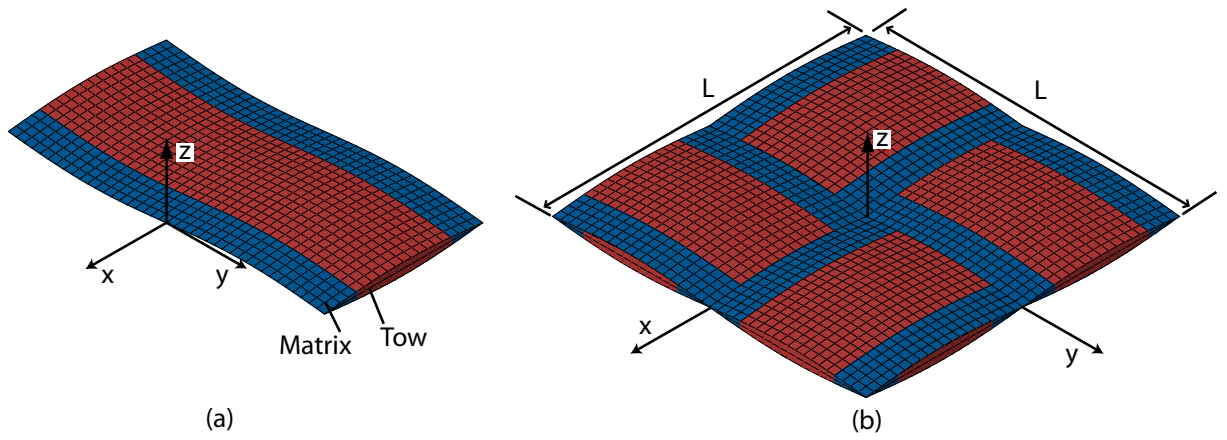
Figure 5.7. Finite element model for plain-weave lamina unit cell: (a) single bundle only, and (b) complete unit cell.
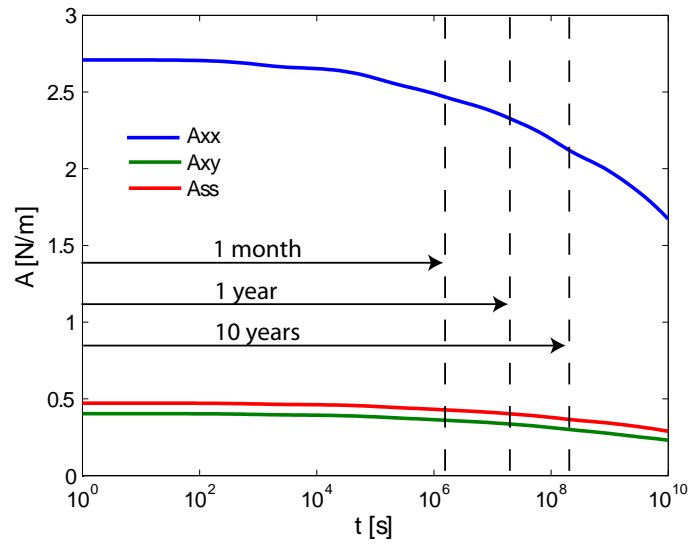
Figure 5.8. Viscoelastic in-plane stiffnesses of plain-weave lamina.
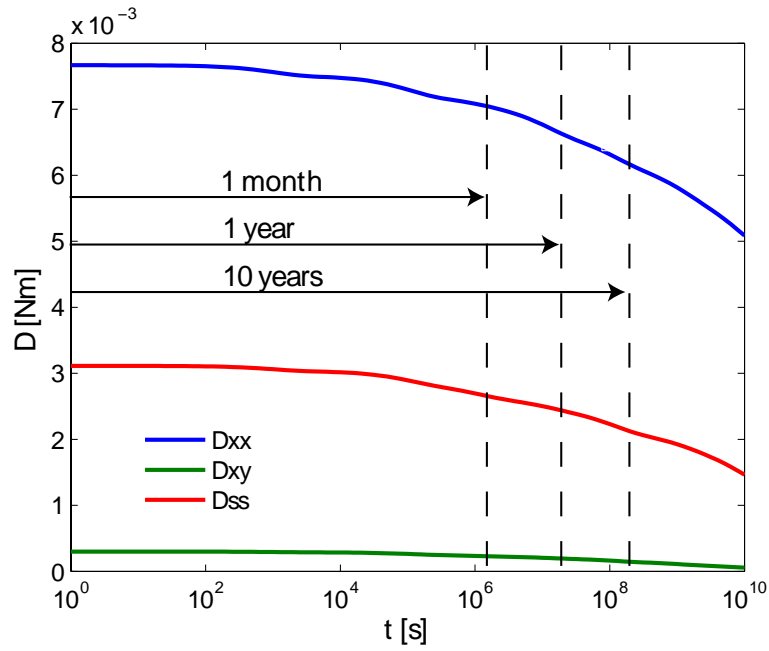
Figure 5.9. Viscoelastic bending stiffnesses of plain-weave lamina.

parisons demonstrate good agreement between model predictions and experimental measurements. Higher noise is observed in the bending test data. In the four-point bending test, the specimen was loaded through point contacts. The vibration of the specimen caused by air circulation inside the environmental chamber was therefore more severe.
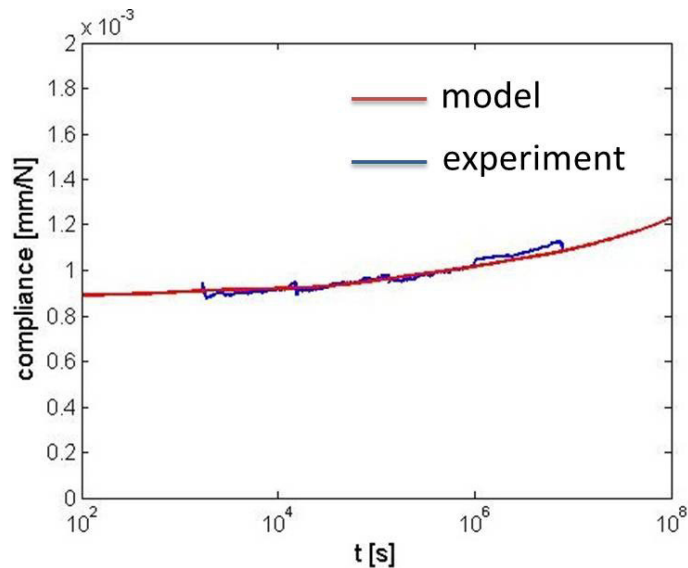
Figure 5.10. Axial compliance of plain-weave lamina at $45°$ angle to fiber direction at a reference temperature of $40°C$.
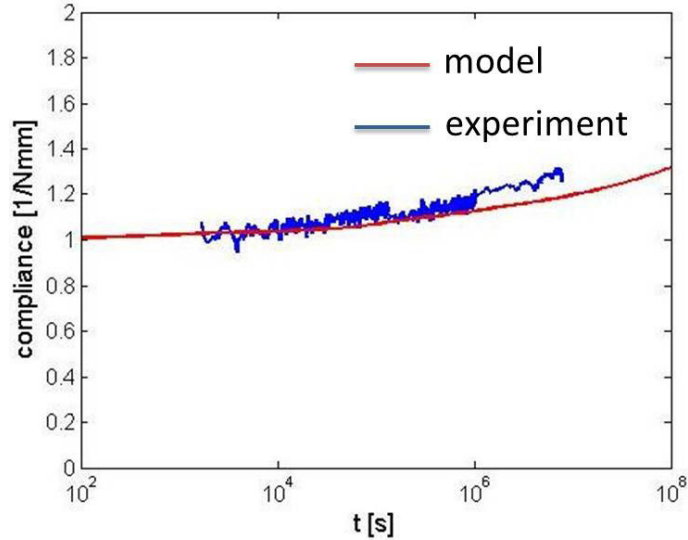
Figure 5.11. Bending compliance of plain-weave lamina at $45°$ angle to fiber direction at a reference temperature of $40°$C.

5.4 Deployment and Shape Recovery Experiments

To assess the deployment and shape recovery behavior after stowage, experiments were carried out on a composite tape-spring with a radius of 19 mm, a thickness of 0.125 mm, a length of 596 mm, and an areal density of 131.2 g/m^2. The tape-spring was made of ± 45 plain-weave fabric with 1 k tows of T300 carbon fibers impregnated with PMT-F4 epoxy resin. It was fabricated by laying the resin-impregnated fabric on a cylindrical steel mandrel, wrapping the assembly in release films, and cured under vacuum for 2 hours at $120°$C and 400 kPa. A single-ply lamina was used so that the resulting tape-spring would have a relatively low stiffness and its deployment would span for a longer period for experimental measurements. The lamina layup was chosen to be ± 45 because the behavior in the longitudinal direction of the tape-spring is dominated by the matrix and hence more sensitive to effects of time and temperature changes.

An important feature of viscoelastic behavior in polymers is the temperature dependence of the relaxation time. Epoxy matrix materials have glass transition temperature T_g well above room temperature and therefore show little viscoelastic response. A long stowage time is required to observe noticeable viscoelastic effects during deployment. However, relaxation or creep behavior accelerates as the temperature moves towards T_g. To shorten stowage time for experimental measurements, the tape-spring was therefore stowed at a higher temperature.

Each test consisted of stowing the tape-spring for a given length of time at a specified temperature, deploying it, and measuring the shape change over time after deployment. Experiments were performed inside a thermal chamber that stabilizes the temperature of the specimens within $0.1°$C over the test period. The test specimen was clamped on the bottom and positioned vertically on a

granite table to reduce background vibration. Thermocouples were placed at three different locations in the vicinity of the specimen to monitor the temperature uniformity, which can be controlled within $\pm 0.5°$C. In Chapter 4, it was discovered that the behavior of viscoelastic tape-springs is characterized by a short-term deployment phase followed by a long-term recovery phase. Tape-springs undergo large displacements within a short period during deployment and exhibit infinitesimal deformations over extended periods during shape recovery. Two displacement measurement schemes were therefore employed to probe the behavior under such drastically different length and time scales. The deployed angle was extracted from images taken using a high resolution camcorder with a frame rate of 30 fps. Full field displacements of the fold region in the tape-spring were measured using a three dimensional digital image correlation system during the recovery phase. The system consists of two Point Grey Research CCD cameras with a resolution of 2448 x 2048 and a pixel size of 3.45 μm x 3.45 μm. The cameras were positioned to capture a series of images of the inner surface of the tape-spring throughout the test. The experimental configuration is shown in Figure 5.12.

The test proceeded as follows. The chamber was first heated and stabilized at the stowage temperature. The chamber was then opened for manually stowing the tape-spring to an angle of 87° so that gravity could be taken advantage of to slow down the initial deployment time. To minimize the disturbance of the thermal environment, the chamber was kept opened for only a short time. The specimen was stowed for a period of 8 h, after which the temperature inside the chamber was changed to the deployment temperature and the specimen was deployed. Displacements were measured continuously over time from the instant of deployment to 8 h after deployment. Three sets of tests with different stowage and deployment temperatures summarized in Table 5.3 were conducted. Each type of test was repeated with nominally identical conditions.

As noted previously, the behavior of tape-springs after stowage can be divided into two stages, namely deployment and recovery. Figure 5.13 plots the measured deployed angle over time for all tests and Figure 5.14 shows a series of intermediate shapes of the tape-spring during deployment for test 2. In all cases, the tape-spring passes through the undeformed configuration and overshoots by a small amount, after which the deployed angle gradually tends towards zero. The effect of stowage at different temperatures is apparent in Figure 5.13. In test 1, the maximum overshoot occurred at 0.4 s with a magnitude of -1.4°. In test 2, the maximum overshoot was delayed to 0.65 s with a larger angle of -2.5°. The deployment responses for tests 2 and 3 are nearly identical with only a minor difference in the overshoot time. This result suggests that short-term deployment is affected mainly by the stowage conditions and the deployment conditions have only a minor effect.

Figure 5.15 shows the measured out-of-plane displacement field in the fold region of the tape-spring, superimposed on images of the specimen over a longer time span for test 2. The displacement field measurements were obtained from analyzing images of the deformed specimens with the Vic-3D digital image correlation software. The principle of analysis is the following. A reference image is first

chosen and divided into small square regions. The software then matches these regions between any subsequent image and the reference image based on pattern recognition algorithms and determines the displacement components between the two images. The result is then a displacement field for each image relative to the reference. To illustrate the small movements during recovery, the image taken at the instant of maximum overshoot was chosen to be the reference. As shown in Figure 5.15, an out-of-plane displacement of only 3.0 mm was recorded over 5743 s (1.6 h) whereas the original depth of the tape-spring is 16.0 mm. This indicates that the cross-sectional shape of the tape-spring was slowly changing over a long period after deployment, even though the tape-spring had nearly reached the undeformed configuration in about 1 s. If the tape-spring had been made of a time-independent material, the cross section would have fully recovered and arrived at the fully deployed configuration almost instantaneously.

The experimental results presented provide a quantitative characterization of how stowage extends the time for deployment and shape recovery in viscoelastic composite structures.
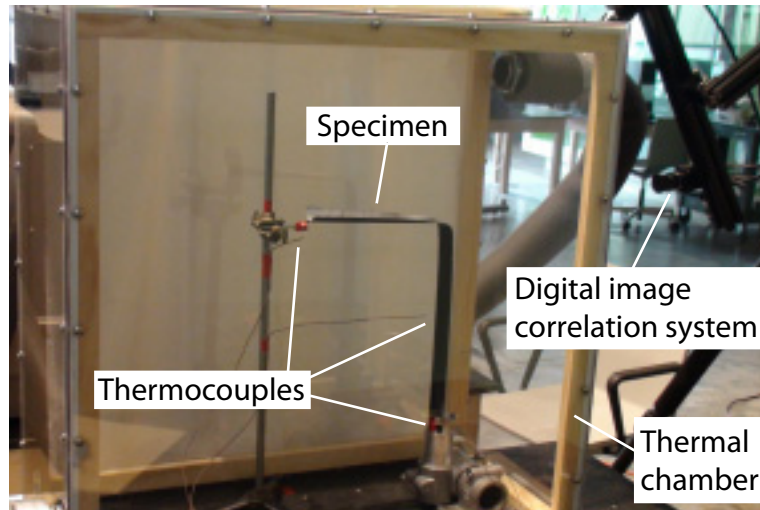
Figure 5.12. Experimental configuration.

Test	Stowage temperature [°C]	Deployment temperature [°C]
1	23	23
2	60	60
3	60	23

Table 5.3. Conditions of tests conducted.
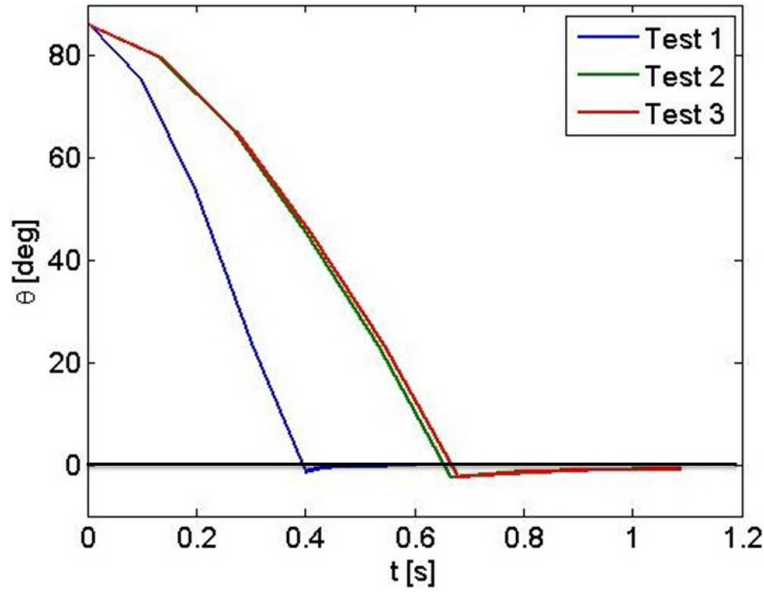
Figure 5.13. Measured deployed angle vs. time.

5.5   Finite Element Analysis and Results Comparison

The response of composite tape-springs, studied experimentally in Section 5.4, was simulated in Abaqus/Standard using a model with 2268 quadrilateral shell elements (S4) with a maximum dimension of 3.85 mm as shown in Figure 5.16. The viscoelastic stiffness properties of the shell elements were defined by assigning the ABD matrix obtained in Section 5.3.3 via a user-defined shell section subroutine (UGENS). The temperature shift factor of the shell elements was taken to be the same as that of the matrix.

The boundary conditions were applied as follows. The bottom end section CC' was held fixed throughout the analysis. To reach the stowed configuration, the cross section at the fold region was first flattened by applying equal and opposite rotations on the two edge nodes B and B'. At the same time, a rotation of $87°$ was applied to the middle node A of the top cross section of the tape-spring. The prescribed rotations on the edge nodes were then removed and the tape-spring was kept at the stowed configuration for 8 h. The boundary condition on the top node was released instantaneously at the end of the stowage step. The analysis was quasi-static for the folding and stowage steps, and was switched to dynamic after the removal of the top node constraint. The deployment process was simulated for 8 h. Gravity loading was imposed in the z-axis throughout the simulation. The analysis took 40 h to complete.

Figure 5.17 compares the deployment angle vs. time profile during deployment between experimental measurements and finite element simulations for test 2. Overall, the simulations show good agreement with the observed response, except that the overshoot angle is overpredicted by about
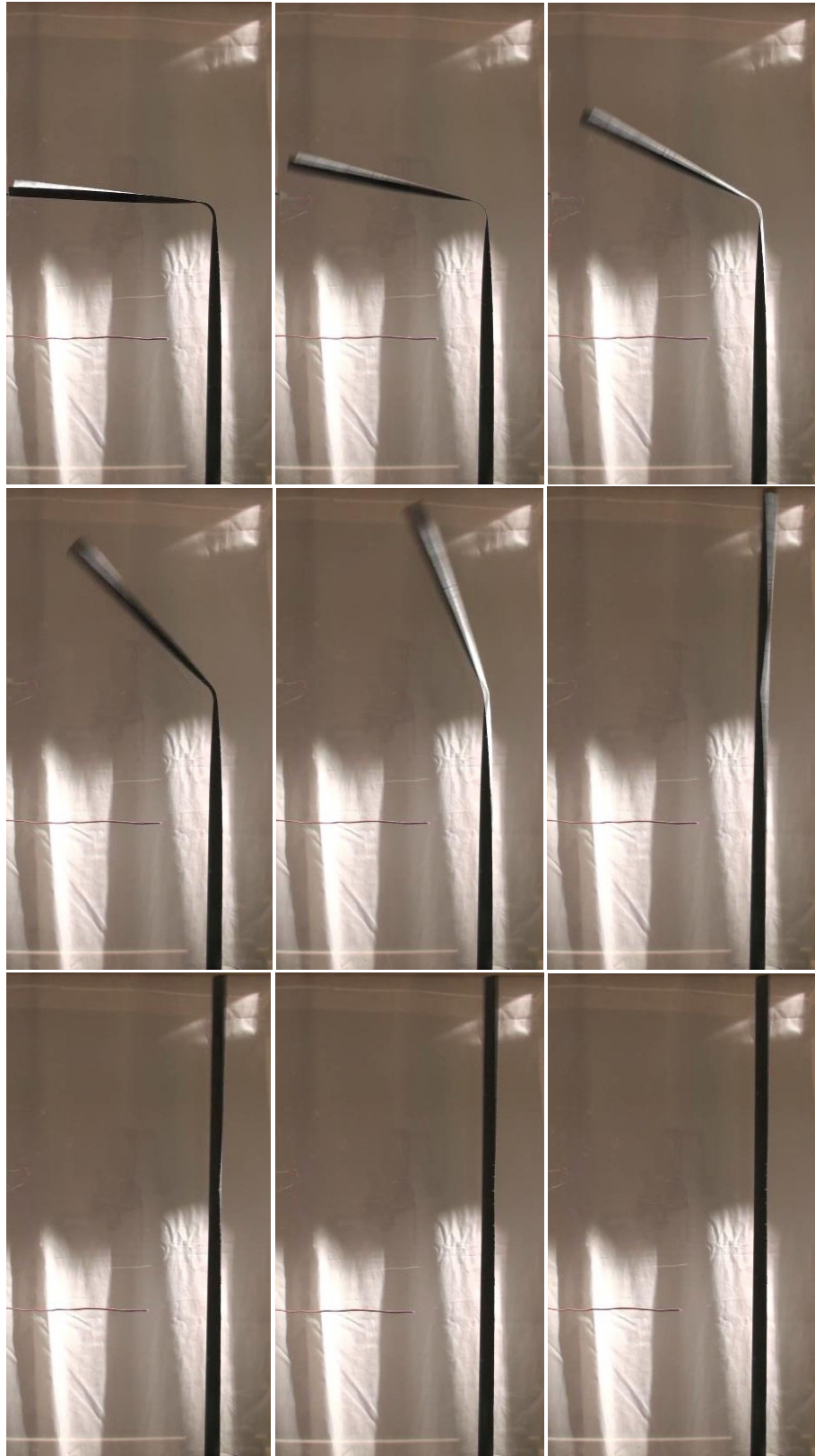
Figure 5.14. Snapshots at 0 s, 0.13 s, 0.26 s, 0.39 s, 0.52 s, 0.65 s, 0.78 s, 0.91 s, and 1.04 s of deployment sequence.
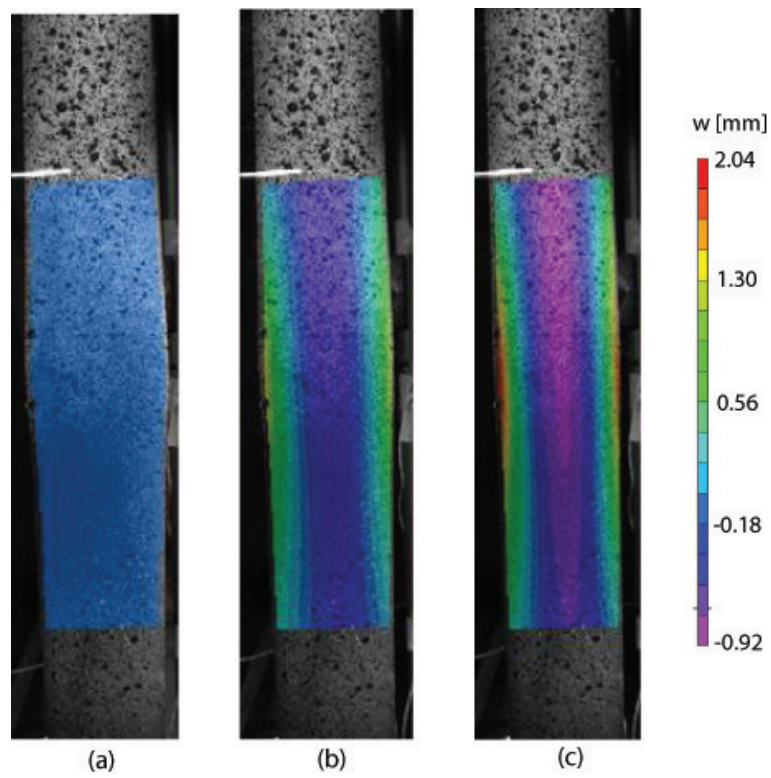
Figure 5.15. Measured out-of-plane displacements of the fold region relative to the configuration of maximum overshoot: (a) at overshoot (reference), (b) after 50 s, and (c) after 5743 s.

1.5°.
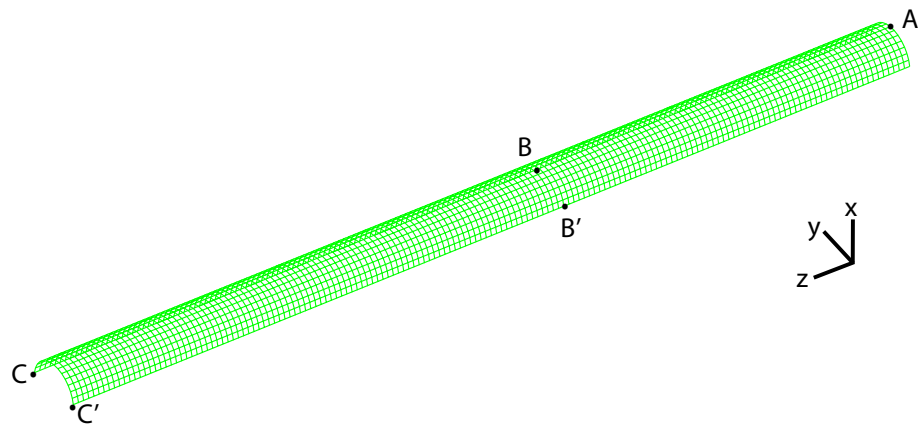
Figure 5.16. Finite element model for tape-spring.
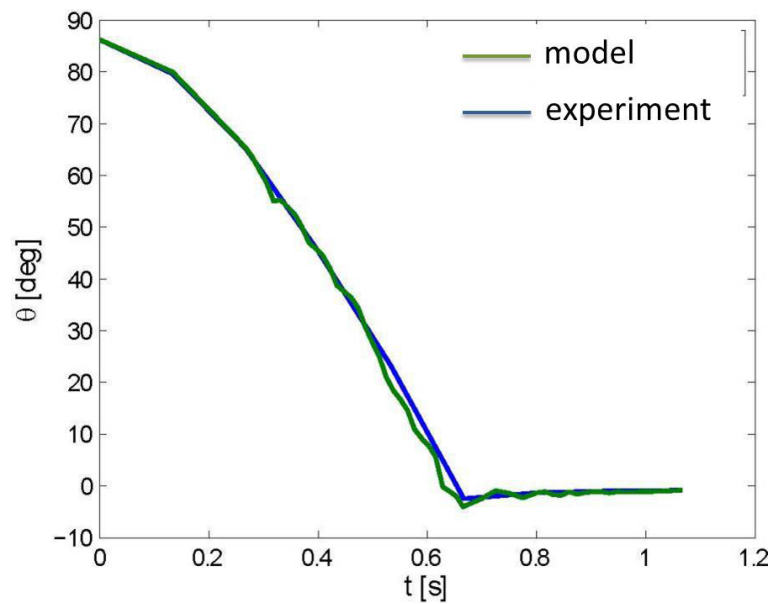
Figure 5.17. Comparison of deployment angle vs. time.

5.6 Prediction of Long-term Stowage Effects

The effect of long-term stowage was investigated numerically using the micromechanical viscoelastic model. A finite element analysis in which the composite tape-spring was subject to a stowage period of 1 year at 23°C was carried out. The finite element model and the simulation techniques were identical to those in Section 5.5. The deployment angle is plotted against time in Figure 5.18. It is observed that the deployment is drastically different from the behavior after shorter stowage times

studied in Section 5.4. The tape-spring only deploys to an angle of 82.6° in 15 days and seems to stay at this angle. This is because the internal force has reduced to a low value after 1 year of stowage and is not sufficient to deploy the tape-spring under gravity loading.
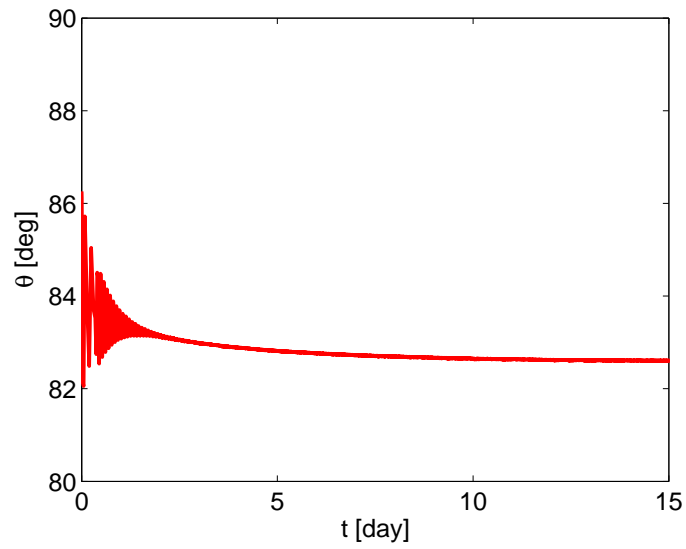
Figure 5.18. Predicted deployment angle after 1 year of stowage at 23°C.

Chapter 6

Stress Concentrations in Balloon Films

6.1   Introduction

As mentioned in Chapter 1, the NASA superpressure balloon consists of a thin envelope made of linear low density polyethylene (LLDPE) film, contained within equally spaced meridional tendons. A limiting factor in the design of these balloons is the presence of high stress concentrations in relatively small regions of the balloon film. One area where stress concentrations arise is at the junction of tendon pockets and balloon envelope. To maintain the position of a tendon in between adjacent lobes, a tendon pocket constructed by the same balloon film material is bonded to the balloon envelope, Figure 6.1. As a result, the thickness of the envelope abruptly increases at the locations of tendon pockets.

To enable the estimation of realistic factors of safety the actual stress concentrations in these regions need to be predicted, which requires accurate modeling of the phenomena that affect the stress state at regions with localized deformation. The film used in NASA superpressure balloons is a 38 μm thick polymer film called StratoFilm 420, which exhibits nonlinear viscoelastic, anisotropic properties (Rand and Sterling, 2006; Rand and Wakefield, 2010) and is easily wrinkled. A viscoelastic model for StratoFilm 420 has been formulated based on the Schapery theory by Rand and Sterling (2006) and implemented in a finite element analysis to study the overall shape and stress distribution (Gerngross et al., 2008). However, the local strains in regions of stress concentrations are expected to exceed the limits of validity of this model.

This study establishes a computational model that accurately predicts the anisotropic, viscoelastic material response as well as the wrinkling instability behavior at large strains to avoid over-conservative designs due to incorrect estimates of localized stress concentrations. The proposed model is applicable up to the point where the instantaneous stiffness of the material vanishes and irrecoverable deformation begins.
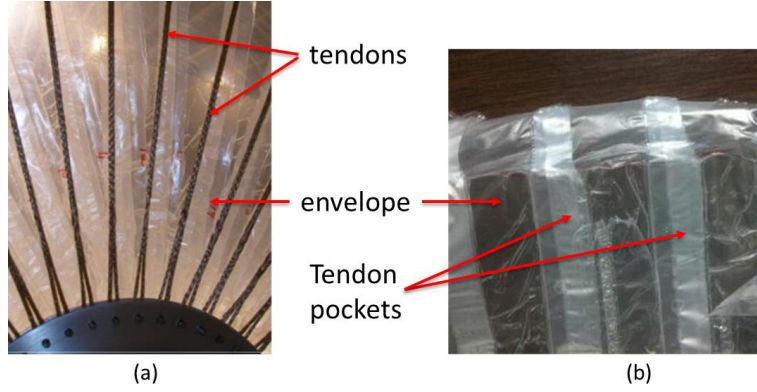
Figure 6.1. Thickness variation in balloon envelops due to bonding extra layers of film to construct tendon pockets.

6.2 Background

6.2.1 Nonlinear Viscoelasticity

Time and temperature dependent behavior of polymers is well studied in linear viscoelasticity. When the viscoelastic behavior is nonlinear, the Boltzmann superposition principle used in linear viscoelasticity is no longer directly applicable. Constitutive models based on the multiple integral approach were first proposed but found limited usage due to the complexity of the resulting equations and substantial laboratory characterization required. The first widely used nonlinear viscoelastic model is due to Schapery, who introduced a single integral formulation where nonlinearities appear in the constitutive equations as stress or strain dependent material parameters (Schapery, 1966 1969 1997).

Another single integral model is the free volume model presented by Knauss and Emri (1981 1987). Instead of relying on the stress or strain dependent material parameters that have no direct physical interpretation, they postulated a relation between macroscopic deformation and time shift factor through the concept of free volume. Free volume is the intermolecular space in a polymer that allows for freedom of molecular chain motions over time in response to imposed deformation, giving rise to the observed viscoelastic response. Chain mobility is enhanced with increased free volume, allowing for faster accommodation of the chains to the imposed deformation. Hence the free volume implicitly controls the time scale of the material. The time shift factor was related to the free volume by Doolittle (1951),

$$\log\ a = \frac{B}{2.303}\left(\frac{1}{f} - \frac{1}{f_0}\right),\tag{6.1}$$

where B is a material function, f denotes the fractional free volume and f_0 is the fractional volume at some reference conditions. In the free volume model, the volumetric dilatation ϵ_v is correlated

with free volume by

$$f = f_0 + \alpha_v(T - T_0) + \epsilon_v, \tag{6.2}$$

where α_v is the volumetric coefficient of thermal expansion. Combining Equations (6.1) and (6.2) gives

$$\log a = \frac{-B}{2.303 f_0} \left[\frac{\alpha_v(T - T_0) + \epsilon_v}{f_0 + \alpha_v(T - T_0) + \epsilon_v} \right]. \tag{6.3}$$

It can be shown that Equation (6.3) reduces to the Williams-Landel-Ferry (WLF) equation in linear viscoelasticity in the case of negligible volumetric strain. The free volume model was formulated using finite kinematics to predict the rubbery behavior of polymers (O'Dowd and Knauss, 1995) and modified to include distortional effects by Popelar and Liechti (1997). The modified model has been implemented in finite element simulations to study nonlinear shear behavior (Popelar and Liechti, 2003). Only isotropic materials were considered in these studies.

Both the Schapery model and the free volume model were found to be inadequate in predicting the unloading behavior in uniaxial cyclic tests (Xia et al., 2006). In particular, the experimentally determined unloading path has a concave curvature while the models predict a convex path. The same discrepancy was observed for other nonlinear viscoelastic models (Zhang and Moore, 1997), including the distortion-modified free volume model (Arzoumanidis and Liechti, 2003). Models with an incorrect unloading path curvature tend to underestimate the strain recovery during unloading. Among the attempts to remedy this problem, the unloading switch rule proposed by Xia et al. (2006) has demonstrated the ability to correct the curvature sign when incorporated into nonlinear viscoelastic models.

6.2.2   Wrinkling

Wrinkling can be explained as a structural instability where a thin plate deforms out-of-plane when it is subject to in-plane compression. Numerical modeling of wrinkling is mainly performed using either shell or membrane elements. Shell elements are able to capture the three-dimensional wrinkled shape, but such an analysis requires small element size and hence high computational cost. Membrane elements neglect the shape of wrinkles and aim to capture only the mid-plane deformation and stress distribution. When the details of the wrinkles are not the primary concern, a membrane analysis provides an efficient approach. However, in finite element analysis using conventional membrane elements, wrinkling leads to element over-contraction and thus the strain and stress states are incorrectly computed.

In classical theory, a membrane is under plane stress and has no bending stiffness. When the compressive stress exceeds the critical load, the membrane wrinkles because it has no bending stiff-

ness and stops carrying compression. This instability is not accounted for in conventional membrane elements, which result in overestimation of compressive strain and stress. The issue is outlined in Figure 6.2. Many models have been proposed to circumvent the issue of element over-contraction and are based upon two unifying assumptions: (1) the critical compressive load for wrinkling is zero, and (2) a wrinkled element is in a uniaxial tension state and the direction of tension is perpendicular to the wrinkling direction.

The aforementioned simplifications were first used in the tension field theory to tackle isotropic membrane wrinkling (Reissner, 1938). Based on the same assumptions, Stein and Hedgepeth (1961) modified the elastic properties and introduced the concept of variable Poisson's ratio to remove compressive stress in the wrinkled regions. Pipkin (1986) treated wrinkling as an energy minimization problem and replaced the standard strain energy density with the relaxed energy density, which becomes zero when a compressive strain is applied. Roddeman et al. (1987) introduced a virtual elongation into the deformation gradient of a wrinkled membrane so that the modified deformation reflects the actual deformation.

Analysis of anisotropic membranes is more challenging because the direction of wrinkles is generally not aligned with the principal stress direction as in the case of isotropic membranes. A wrinkle direction search procedure is necessary before any modification can be made. Kang and Im (1997) proposed a scheme that modifies the transverse strain in the wrinkle direction so that the transverse stress in that direction vanishes. They observed that the shear strain of an over-contracted element is the same as that in a truly wrinkled membrane and used this as a condition to find the wrinkling direction. Alternatively, Epstein and Forcinito (2001) extended the relaxed energy function to anisotropic membranes through the concept of saturated elasticity.

Although a variety of approaches has been proposed, the resulting constitutive relations obtained are essentially identical because the models are based on common assumptions (Miyazaki, 2006). The difference is in their numerical implementation and physical interpretation.

The incorporation of wrinkling behavior in membrane analysis leads to different element modifications depending on the stress state of the element. The three possible states of a membrane are the taut state, in which tensile stress exists in all directions; the wrinkled state, in which both tension and compressive are present; and the slack state, in which only compression exists. A wrinkling criterion is used to distinguish the element state in the course of a finite element analysis. Three wrinkling criteria, namely stress criterion, strain criterion, and combined stress-strain criterion (Roddeman et al., 1987), have been proposed. Kang and Im (1997) compared the three criteria and concluded that the stress-strain criterion is the most suitable for wrinkling analysis of anisotropic membranes. The combined stress-strain criterion is given by

$$taut: \quad \sigma_2 > 0$$
$$wrinkled: \quad \epsilon_1 > 0 \quad \text{and} \quad \sigma_2 \leq 0 \qquad (6.4)$$
$$slack: \quad \epsilon_1 \leq 0$$

where ϵ_1 is the major principal strain and σ_2 is the minor principal stress.
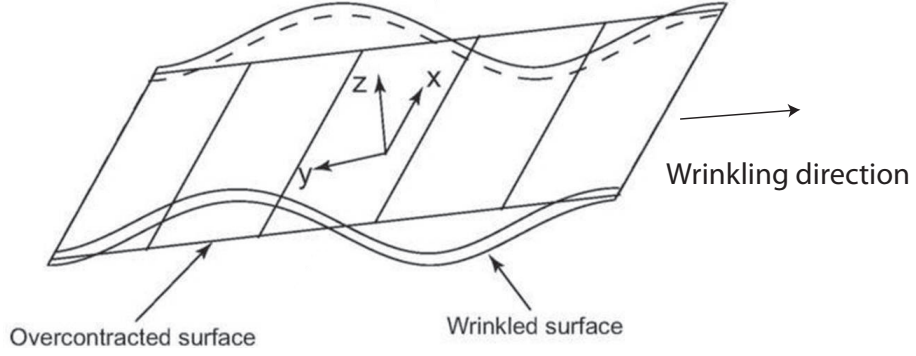
Figure 6.2. Membrane element over-contraction due to wrinkling.

6.3 Model Formulation

StratoFilm 420 is produced by a coextrusion process of three layers of films, resulting in directional-dependent material properties. In the current work, the film is modeled as an orthotropic membrane with principal material directions denoted as machine direction (MD) and transverse direction (TD). The free volume nonlinear viscoelastic model is extended to include material orthotropy. For modeling wrinkling, the procedure proposed by Kang and Im (1997) is adopted.

6.3.1 Orthotropic Free Volume Model

The free volume model is adopted for the balloon film and plane stress conditions are assumed. Finite strains and rotations are present during large deformations, making different stress and strain measures possible for constitutive modeling (Holzapfel, 2000). To satisfy the principle of objectivity, the model formulated herein is formulated in terms of the second Piola-Kirchoff stress P and the Green-Lagrange strain E, which form a conjugate pair. They are defined as

$$[P] = J[F^{-1}][\sigma][F^{-T}], \qquad (6.5)$$

$$[E] = [F^T][F] - [I], \qquad (6.6)$$

where $[F]$ is the deformation gradient, $[\sigma]$ is the Cauchy stress, and J is the Jacobian defined by $J = \det[\mathrm{F}]$. The constitutive relation is given as

$$[E(t)] = \int_0^t [D(t' - s')] \left[\dot{P}(s)\right] ds, \tag{6.7}$$

where t' is the reduced time defined as

$$t' = \int_0^t \frac{du}{a} \quad \text{and} \quad s' = \int_0^s \frac{du}{a}. \tag{6.8}$$

The shift factor a is given by Equation (6.3). The Green strains and the second Piola Kirchoff stresses are

$$[E(t)] = \begin{bmatrix} E_1(t) \\ E_2(t) \\ E_3(t) \\ E_6(t) \end{bmatrix}, \tag{6.9}$$

$$[P(t)] = \begin{bmatrix} P_1(t) \\ P_2(t) \\ 0 \\ P_6(t) \end{bmatrix}, \tag{6.10}$$

where the subscripts 1 and 2 denote the machine and transverse direction of the film respectively, the subscript 3 denotes the direction normal to the film, and the subscript 6 denotes the in-plane shear direction. The creep compliance $D(t)$ takes the form

$$[D(t)] = \begin{bmatrix} D_{11}(t) & D_{12}(t) & D_{13}(t) & 0 \\ D_{12}(t) & D_{22}(t) & D_{23}(t) & 0 \\ D_{13}(t) & D_{23}(t) & D_{33}(t) & 0 \\ 0 & 0 & 0 & D_{66}(t) \end{bmatrix}, \tag{6.11}$$

Under plane stress conditions the compliance is often written as a 3 by 3 matrix, however the compliance matrix in Equation (6.11) has the additional terms D_{13}, D_{23} and D_{33} corresponding to the film behavior in the thickness direction. These coefficients are needed to compute the volumetric strain as an internal state variable in the free volume model. The volumetric strain is defined as

$$\epsilon_v = det(F) - 1. \tag{6.12}$$

Each entry in $D(t)$ is represented by a Prony series,

$$D(t) = D_0 + \sum_{j=1}^{n} D_j (1 - e^{-t/\tau_j}), \tag{6.13}$$

where D_0 is the instantaneous compliance, D_j are the retardation coefficients, τ_j are the retardation times.

In summary, the complete model describes the nonlinear viscoelastic response by means of Equations (6.3), (6.7), (6.8), and (6.11).

6.3.2   Material Parameters for StratoFilm 420

To implement the orthotropic free volume model, the material parameters in Equations (6.3) and (6.11) need to be determined. For calculating the time shift factor in Equation (6.3), the necessary parameters are B, α_v, and f_0. In Equation (6.11), there are 7 independent compliance functions, but only 6 are needed because $D_{33}(t)$ is multiplied by zero in the case of plane stress. For StratoFilm 420, most of the required parameters can be converted from data collected in (Rand, 2008a) by making certain assumptions on the film behavior in the thickness direction. The remaining parameters were obtained by carrying out additional material characterization tests. This section describes how each parameter was obtained for implementation of the proposed model.

The volumetric coefficient of thermal expansion is written as the sum of the linear coefficients of thermal expansion,

$$\alpha_v = \alpha_1 + \alpha_2 + \alpha_3, \tag{6.14}$$

where the subscripts 1, 2, and 3 denote the machine, transverse, and thickness directions. Both α_1 and α_2 were obtained as polynomial functions of temperature by Young (2010),

$$\alpha_1 = \sum_{j=1}^{13} p_j T^{13-j}, \tag{6.15}$$

$$\alpha_2 = \sum_{j=1}^{13} q_j T^{13-j}, \tag{6.16}$$

where T is temperature in degree Kelvin, p_j and q_j are polynomial coefficients given in Table 6.1. In this work we assume α_3 to be the average of α_1 and α_2. The resulting α_v is plotted in Figure 6.3.

The material functions B and f_0 were determined from temperature shift data in Rand (2008a) as follows. Note that the time shift factor given by Equation (6.3) reduces to the temperature shift factor in linear viscoelasticity where the volumetric strain is infinitesimal. Therefore, B and f_0 can be found by fitting temperature shift data obtained from creep tests at small strains to Equation (6.3) with $\epsilon_v = 0$.

Rand (2008a) obtained the temperature shift data for StratoFilm 420 and expressed the data by the following numerical functions,

$$
\log\ a_T = \begin{cases} (T - 293.16)[7.33 \times 10^{-4}(T - 273.16) - 0.179133] & \text{if}\quad T \geq 233.16\ \text{K}; \\ 3.1068 - 0.2350275(T - 273.16) & \text{if}\quad T < 233.16\ \text{K}. \end{cases} \tag{6.17}
$$

To determine B and f_0, the data represented by Equation (6.17) were fitted to Equation (6.3) with $\epsilon_v = 0$ and $T_0 = 293.16$ K, which is

$$
\log\ a = \frac{-B}{2.303 f_0}\left[\frac{\alpha_v(T - 293.16)}{f_0 + \alpha_v(T - 293.16)}\right]. \tag{6.18}
$$

In the numerical fitting procedure, Equation (6.19) was first rewritten in the WLF form,

$$
\log\ a = \frac{-c_1(T - 293.16)}{c_2 + (T - 293.16)}. \tag{6.19}
$$

where c_1 and c_2 are constants given by

$$
\frac{B}{2.303 f_0} = c_1, \tag{6.20}
$$

$$
\frac{f_0}{\alpha_v} = c_2. \tag{6.21}
$$

The Levenberg-Marquardt algorithm in Matlab was used in the fitting procedure to first find c_1 and c_2, B and f_0 were then obtained with known α_v. The results are plotted in Figures 6.4 and 6.5.

The creep compliance of the film in the machine direction, D_{11}, was expressed as a Prony series of 15 terms at the reference temperature $T_0 = 293.16$ K in Rand (2008a). The master curve is plotted in Figure 6.6 and the corresponding Prony series terms are summarized in Table (6.2). Following the work of Rand (2008b), the remaining in-plane compliances were assumed to be expressed by the same Prony series as the compliance in the machine direction, but multiplied by experimentally determined constants as follows:

$$
D_{12}(t) = -0.48 D_{11}(t), \tag{6.22}
$$

$$
D_{22}(t) = (1.122 + 6.5895 \times 10^{-4} T - 6.609 \times 10^{-6} T^2) D_{11}(t), \tag{6.23}
$$

$$
D_{66}(t) = 4.45 D_{11}(t). \tag{6.24}
$$

It is noted that assuming the compliance functions to be related by time-independent functions or constants results in a simplified representation of the material behavior because the creep compliance functions in different directions can vary with time differently. Independent characterization of the

j	$p_j \; [K^{-1}]$	$q_j \; [K^{-1}]$
1	$-1.314349420165660 \times 10^{-27}$	$1.656628670569420 \times 10^{-27}$
2	$3.757961363054510 \times 10^{-24}$	$-4.538552920810370 \times 10^{-24}$
3	$-4.870560919889060 \times 10^{-21}$	$5.644504822368260 \times 10^{-21}$
4	$3.783161974578100 \times 10^{-18}$	$-4.213294503544060 \times 10^{-18}$
5	$-1.961126506078030 \times 10^{-15}$	$2.102008465628270 \times 10^{-15}$
6	$7.146793667601330 \times 10^{-13}$	$-7.383200108461120 \times 10^{-13}$
7	$-1.877228425197230 \times 10^{-10}$	$1.871956621022750 \times 10^{-10}$
8	$3.580706769622300 \times 10^{-8}$	$-3.451673660888610 \times 10^{-8}$
9	$-4.922242452967390 \times 10^{-6}$	$4.593443382129490 \times 10^{-6}$
10	$4.755521948988130 \times 10^{-4}$	$-4.302432036460990 \times 10^{-4}$
11	$-3.065068396780760 \times 10^{-2}$	$2.692250002443280 \times 10^{-2}$
12	$1.183350730959610 \times 10^{0}$	$-1.010550330725230 \times 10^{0}$
13	$-2.069690662157120 \times 10^{1}$	$1.720772480526920 \times 10^{1}$

Table 6.1. Coefficients of polynomials characterizing the coefficients of thermal expansion.

in-plane compliance functions is currently underway. For the purpose of model development and demonstration, this simplified representation is employed.

The compliance functions D_{13} and D_{23} of StratoFilm 420 were not characterized by Rand. Because of the small thickness of the film, direct measurements of these properties would pose significant challenges. In the present study, D_{13} and D_{23} were determined by fitting the model predictions to the results of uniaxial tensile tests.

Uniaxial tension tests on 38 μm thick specimens of StratoFilm 420 were conducted with an Instron materials testing machine equipped with a thermal chamber. Reflective targets were adhered to the specimen for strain measurements using laser extensometers. A type-T thermocouple was used to monitor the temperature throughout the tests. Prior to testing, the thermal chamber was maintained at $T = 10°$ for 1 hour to achieve stable thermal equilibrium. Specimens with machine and transverse direction oriented along the loading direction were stretched at a nominal strain rate of $0.1\%/s$ to provide data for fitting D_{13} and D_{23} respectively.

The Prony series for D_{13} and D_{23} were assumed to have the same retardation times ρ_j as that of D_{11}. The Prony coefficients were determined by fitting the nonlinear viscoelastic model to data obtained by uniaxial tension tests described above using the Levenberg-Marquardt algorithm in Matlab. The results of the uniaxial tension tests and the numerical fits are shown in Figure 6.7. The Prony series for D_{13} and D_{23} are plotted in Figure 6.8.

6.3.3 Unloading Behavior

To correctly simulate the unloading behavior, the switch rule proposed by Xia et al. (2006) was modified and incorporated into the current free volume model. Xia et al. (2006) first distinguished between loading and unloading using a criterion based on the von Mises stress level experienced by
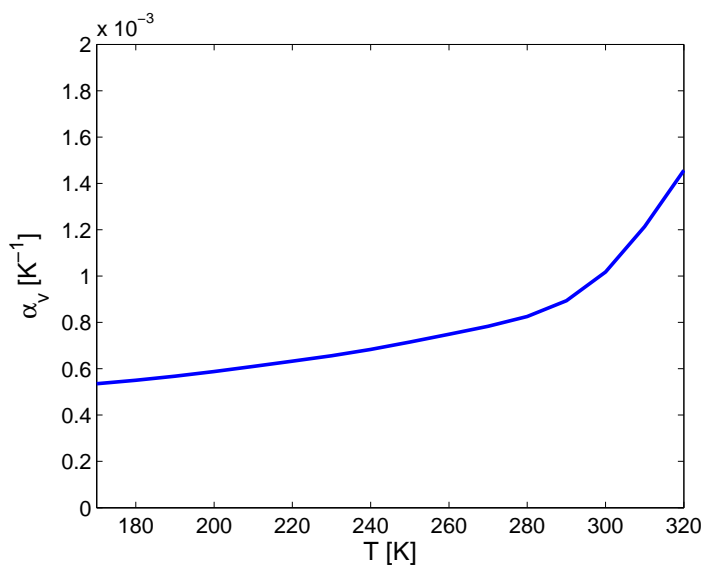
Figure 6.3. Volumetric coefficient of thermal expansion.
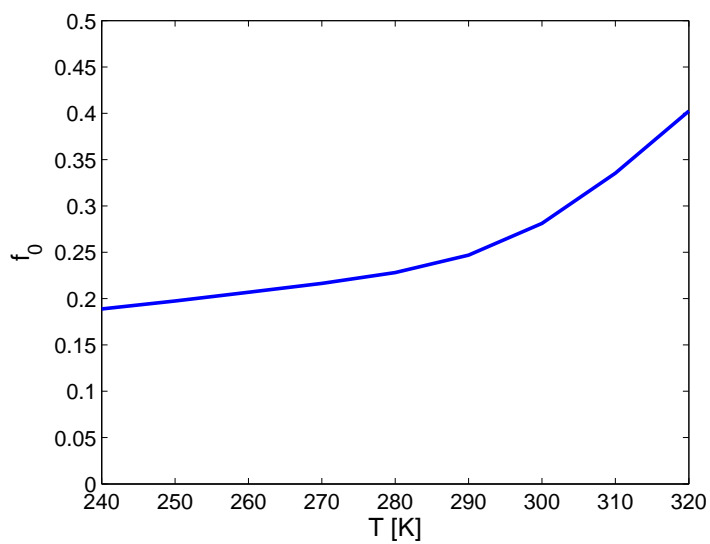
Figure 6.4. Reference fractional free volume.
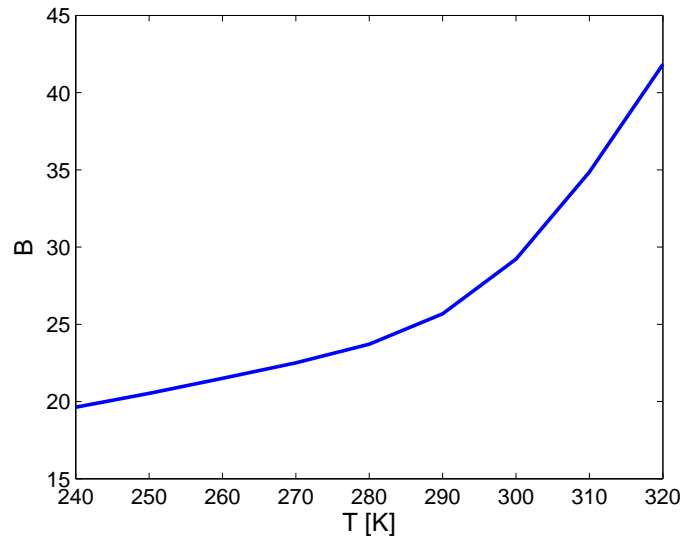
Figure 6.5. Material function B in the time shift factor of the free volume model.
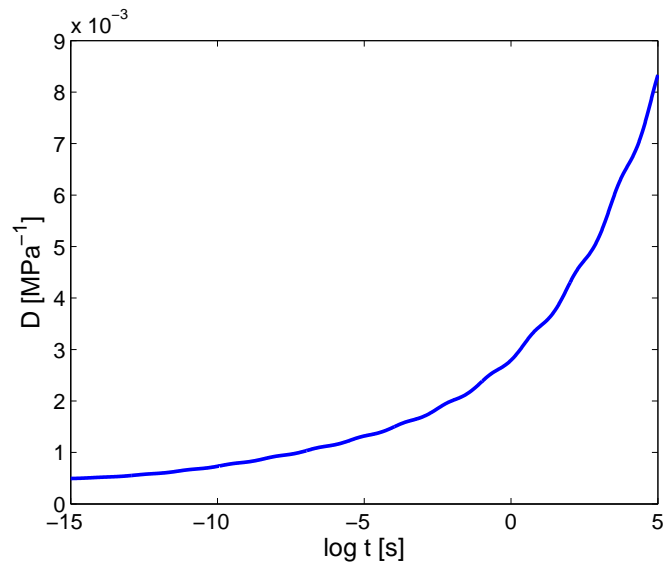
Figure 6.6. Master curve of the machine direction compliance at $T_0 = 293.16$ K.

j	$D_{11,j}\ [MPa^{-1}]$	$\rho_j\ [s]$
0	3.0000×10^{-4}	——
1	1.8764×10^{-4}	1.6548×10^{-16}
2	2.9249×10^{-5}	4.8697×10^{-15}
3	5.8224×10^{-5}	1.4330×10^{-13}
4	8.7542×10^{-5}	4.2170×10^{-12}
5	1.1561×10^{-4}	1.2409×10^{-10}
6	1.4159×10^{-4}	3.6517×10^{-9}
7	1.6989×10^{-4}	1.0746×10^{-7}
8	2.0924×10^{-4}	3.1623×10^{-6}
9	2.7274×10^{-4}	9.3057×10^{-5}
10	3.7796×10^{-4}	2.7264×10^{-3}
11	5.4670×10^{-4}	8.0584×10^{-2}
12	8.0581×10^{-4}	2.3714
13	1.1844×10^{-3}	69.783
14	1.7204×10^{-3}	2053.5
15	2.6285×10^{-3}	60430

Table 6.2. Prony series representation of D_{11}.
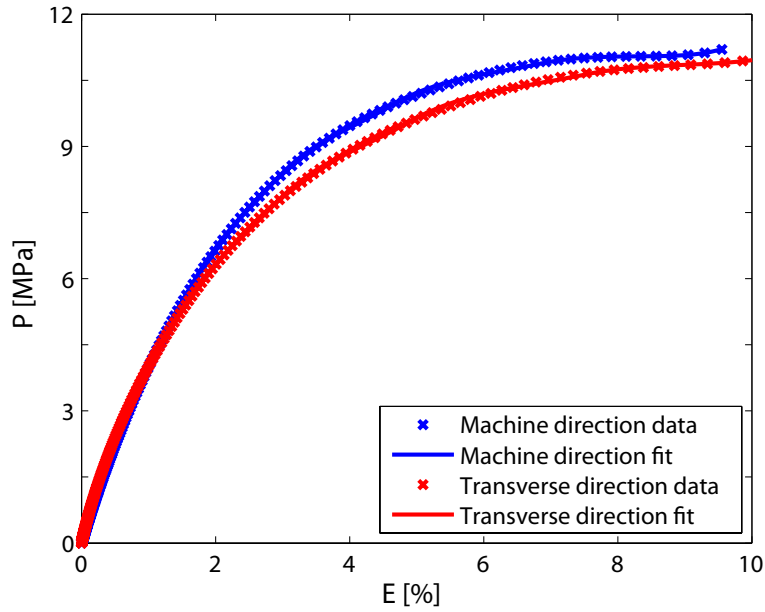
Figure 6.7. Uniaxial calibration tests on two different specimens.
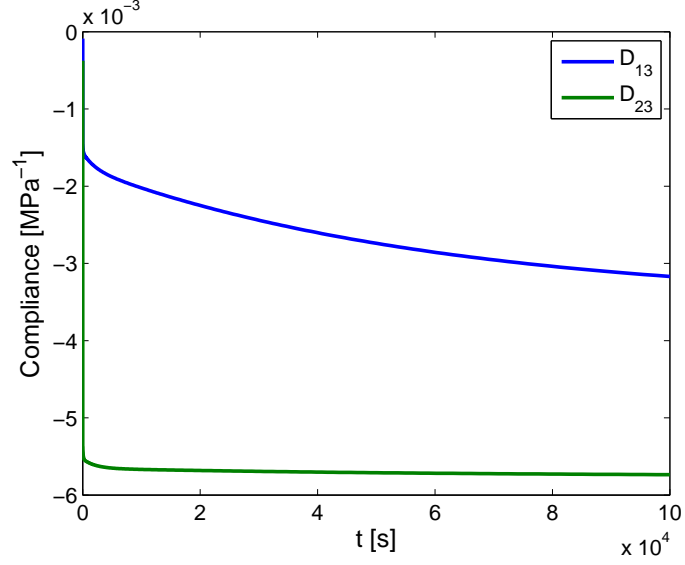
Figure 6.8. Master curves of D_{13} and D_{23}.

the material. The criterion is checked throughout the deformation history. No correction is made when loading but when unloading is detected the nonlinear parameters in the viscoelastic model retain their values at the point of switching from loading to unloading. In the present free volume model, the criterion is based upon ϵ_v. A local maximum in the volumetric strain history corresponds to switching from loading to unloading:

$$\frac{d\epsilon_v}{dt}\bigg|_{switch} = 0; \tag{6.25}$$

$$\frac{d^2\epsilon_v}{dt^2}\bigg|_{switch} < 0. \tag{6.26}$$

During the entire unloading path, the time shift factor is kept constant and is computed using the value of ϵ_v at the switch point. The reverse switching from unloading to loading occurs when Equation (6.25) is again satisfied and Equation (6.26) is reversed.

6.3.4   Orthotropic Wrinkling Model

The model for orthotropic wrinkling is divided into three steps: element state detection, wrinkling angle search in the case of wrinkled element, and recalculation of stress and strain states.

The combined stress-strain criterion described in Section 6.2.2 is employed to determine the state (taut, wrinkled, slack) of an element.

When both principal stresses are positive, the membrane is under biaxial tension and is therefore taut. Then, no stress or strain modification is necessary, and the constitutive equation, Equa-

tion (6.7), gives the correct membrane response.

When both principal strains are less than zero, the membrane is slack. In this case, all stresses of the membrane are zero:

$$[P(t)] = 0. \tag{6.27}$$

When the major principal strain is positive and the minor principal stress is negative, the membrane is wrinkled. It has been mentioned that the state of a wrinkled element is characterized by uniaxial tension in the direction perpendicular to the wrinkles. The correction procedure therefore involves first determining the wrinkling direction and imposing the uniaxial tension state in the wrinkling coordinate frame. The method for searching the wrinkling direction is based upon the work of Kang and Im (1997), but modified for nonlinear viscoelastic membranes described by the constitutive integral in Equation (6.7).

The correction procedure is described as follows. Consider the three configurations of a material element shown in Figure 6.9. The undeformed configuration is denoted by $ABCD$ with $(1, 2)$ defining the directions of material orthotropy. The final, wrinkled configuration is defined by $A"B"C"D"$, in which x and y denote the directions of uniaxial tension and wrinkling respectively. The angle between the material coordinate frame $(1, 2)$ and the wrinkling coordinate frame (x, y), α, is known as the wrinkling angle. The wrinkling direction aligns with the minor principal stress or strain direction in isotropic materials, but this is generally not true for anisotropic materials.

Under a locally homogeneous planar deformation, $ABCD$ deforms to the wrinkled configuration $A"B"C"D"$. The deformation may be thought of as a two-step process. The first step is a purely material deformation from $ABCD$ to $A'B'C'D'$ under uniaxial tensile stress P_w. Wrinkling is absent in this step because the boundaries of the element are free to move. The strain components involved are normal strain E_x^u, transverse strain E_y^u due to Poisson's contraction, and shear strain E_{xy}^u because of coupling between normal and shear compliances of the material in the wrinkling frame (x, y). The second step is a purely wrinkling deformation from $A'B'C'D'$ to $A"B"C"D"$. The material stress and strain states remain the same during this process, but the element contracts due to the formation of wrinkles. Because of the presence of wrinkles, the actual material element is non-planar. The profile represented by $A"B"C"D"$ is in fact only the two-dimensional projection of the actual wrinkle element. An over-estimation of transverse strain in the wrinkling direction would be resulted if it were calculated using the projected surface. This is the origin of the error in conventional membrane analysis. The correct material strains (i.e. without over-contraction in the wrinkling direction) is represented by $A'B'C'D'$, which we seek to determine by correcting the known strains in $A"B"C"D"$.

Kang and Im (1997) demonstrated that the normal and shear strains remain unchanged in going

from $A'B'C'D'$ to $A"B"C"D"$, but the transverse strain reduces. In other words,

$$E_x^u = E_x, \tag{6.28}$$

$$E_{xy}^u = E_{xy}, \tag{6.29}$$

$$E_y^u \geq E_y, \tag{6.30}$$

where E_x, E_y, E_{xy} are the normal, transverse, and shear strains in $A"B"C"D"$.

The unknowns to be found are then P_x, E_y^u and α. They are determined by invoking the uniaxial tension condition in the wrinkling coordinate frame, in which the constitutive equations are written as

$$E_x^u(t) = \int_0^t \widehat{D}_{11}(t' - s')\dot{P}_x(s)ds, \tag{6.31}$$

$$E_y^u(t) = \int_0^t \widehat{D}_{12}(t' - s')\dot{P}_x(s)ds, \tag{6.32}$$

$$E_{xy}^u(t) = \int_0^t \widehat{D}_{16}(t' - s')\dot{P}_x(s)ds, \tag{6.33}$$

where $\widehat{D}_{11}$, $\widehat{D}_{12}$, $\widehat{D}_{16}$ denote the compliance terms in the winkling coordinate frame. They are related to the in-plane compliance terms in the material coordinate frame by a rotation of α,

$$\widehat{[D]} = [R][D][R]^{-1}, \tag{6.34}$$

where $[D]$ is a 3 by 3 matrix filled by the in-plane compliance terms in Equation (6.11) and

$$[T] = \begin{bmatrix} \cos^2(\alpha) & \sin^2(\alpha) & 2\sin(\alpha)\cos(\alpha) \\ \sin^2(\alpha) & \cos^2(\alpha) & -2\sin(\alpha)\cos(\alpha) \\ -\sin(\alpha)\cos(\alpha) & \sin(\alpha)\cos(\alpha) & \cos^2(\alpha) - \sin^2(\alpha) \end{bmatrix}. \tag{6.35}$$

Equations (6.31), (6.32), and (6.33) present 3 equations for finding the three unknowns, P_x, E_y^u and α. An iterative approach is used to solve the nonlinear systems of equations. At the beginning of the solution process, an initial guess is made for α and P_x is first calculated through Equation (6.31) with known E_x^u. The strains E_y^u and E_{xy}^u are then determined from P_x with Equations (6.32) and (6.33). The iteration continues until the conditions $E_{xy}^u = E_{xy}$ and $E_y^u \geq E_y$ are satisfied. It was shown in Kang and Im (1997) that only one solution of α satisfies all the imposed conditions and therefore the wrinkling direction is unique. The strains E_x^u, E_y^u, E_{xy}^u, and the uniaxial tensile stress P_x finally obtained define the correct stress and strain states of an element that wrinkles at an angle

α from the material directions.
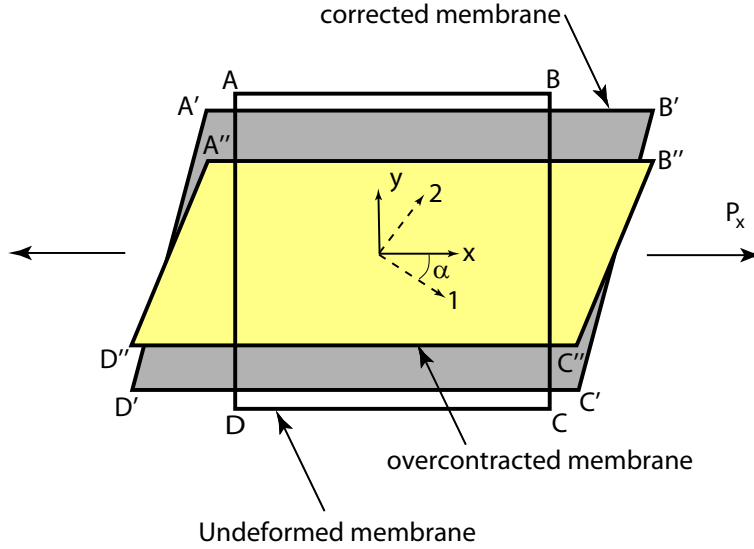
Figure 6.9. States of an element in the wrinkling process.

6.4 Numerical Implementation

The nonlinear viscoelastic model, loading/unloading switch rule, and wrinkling models described in Section 6.3 were combined and implemented in the explicit dynamic finite element solver Abaqus/Explicit through a user-defined material (VUMAT) subroutine. Because of the presence of strong nonlinearity due to wrinkling, an explicit solver has advantages in terms of computational cost over an implicit solver. For this reason Abaqus/Explicit was chosen for the current study. This section first describes the overall scheme of the numerical implementation and discusses the each component of the subroutine in detail.

An overview of the computational scheme within an iteration is depicted in Figure 6.10. In each iteration, the Abaqus solver passes to the VUMAT subroutine the time increment size Δt and the corresponding Green strains at the end of the current increment $[E_t]$. The role of VUMAT is to update the Cauchy stress $[\sigma_t]$.

The VMAT subroutine first uses the volumetric strain at the end of the previous time increment, $\epsilon_{v,t-\Delta t}$, to decide whether a switch from loading to unloading is required, and computes the time shift factor $a_{t-\Delta t}$ using the chosen volumetric strain and the given temperature T. The current in-plane stresses $[P_t]$ are obtained from the constitutive equations based on $a_{t-\Delta t}$ and $[E_t]$. At this point, each element is checked for wrinkling and corresponding corrections are made to the element stress and strain states depending upon the element state. The through-thickness strain $E_{3,t}$ and the volumetric strain $\epsilon_{v,t}$ are now determined from the correct $[P_t]$ and $[E_t]$, and stored for the next

iteration.

Note that the stress update is based on $a_{t-\Delta t}$, instead of an iterative scheme to arrive at a closer approximation for the current increment. Such an explicit integration approach is augmented by a step size adjustment process to maintain the accuracy of the solution. In this procedure, the time increment is reduced and the numerical procedure is repeated from the beginning until a specified tolerance on the change in volumetric strain $\Delta \epsilon_v$ is satisfied. The computed stresses $[P_t]$ are finally pushed forward to the Cauchy stresses $[\sigma_t]$ for returning to the Abaqus solver.

6.4.1   Loading/Unloading Switch Rule

Numerically, the criterion for switching described by Equations (6.25) and (6.26) is realized by comparing the values of volumetric strain at consecutive time steps. The time shift factor is determined according to

$$
\begin{aligned}
a_{t-\Delta t} &= a(T_{t-\Delta t}, \epsilon_{v,t-\Delta t}) \quad \text{if} \quad \epsilon_{v,t-\Delta t} \geq \epsilon_{v,t-2\Delta t}; \\
a_{t-\Delta t} &= a(T_{t-\Delta t}, \epsilon_{v,s}) \qquad \text{if} \quad \epsilon_{v,t-\Delta t} < \epsilon_{v,t-2\Delta t}.
\end{aligned}
\tag{6.36}
$$

where s is the time at which loading switches to unloading. For an element loaded from its unstressed configuration at $t = 0$, the first instance $\epsilon_{v,t-\Delta t} < \epsilon_{v,t-2\Delta t}$ is detected identifies the first switching point. It follows that a local maximum volumetric strain is located at $t - 2\Delta t$ and therefore $\epsilon_{v,s} = \epsilon_{v,t-2\Delta t}$. This value of the volumetric strain is stored and used for computing $a_{t-\Delta t}$ until when $\epsilon_{v,t-\Delta t} \geq \epsilon_{v,t-2\Delta t}$ is detected again. The model uses the closest local maximum volumetric strain to compute the time shift factor during unloading for each cycle.

6.4.2   Stress Computation

To compute $[P_t]$, the recursive integration algorithm proposed by Lai and Bakker (1996) is employed. The derivation of the discretized constitutive equations formulated in terms of relaxation modulus has been described in Chapter 2. In the present implementation, the algorithm is modified for the free volume nonlinear viscoelastic model and formulated in terms of creep compliance. For illustration of the algorithm, the discretized equations are presented for the uniaxial case first and then generalized for multiaxial situations. In uniaxial deformation, assuming the stress P_t varies linearly over the current time step, the current strain E_t, is expressed by

$$
E_t = D_0 P_t + \sum_{j=1}^{n} D_j P_t - \sum_{j=1}^{n} D_j q_{j,t},
\tag{6.37}
$$

where

$$
q_{j,t} = e^{-\Delta t'/\rho_j} q_{j,t-\Delta t} + (P_t - P_{t-\Delta t}) \frac{1 - e^{-\Delta t'/\rho_j}}{\Delta t'/\rho_j}.
\tag{6.38}
$$
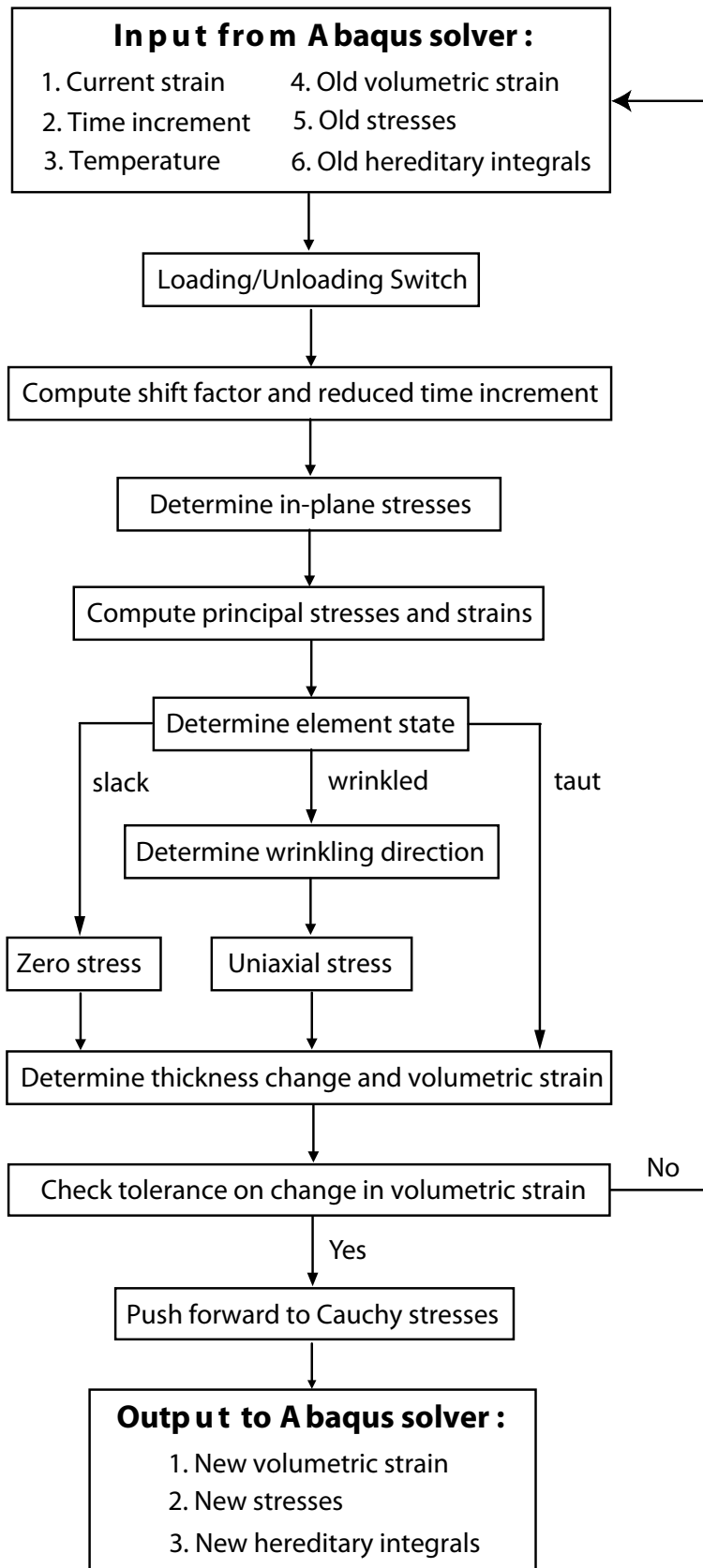
Figure 6.10. Overview of model implementation in VUMAT subroutine in Abaqus/Explicit.

The hereditary integrals $q_{j,t-\Delta t}$ and stress $P_{t-\Delta t}$ have been computed in the previous step and stored as state variables. The reduced time increment $\Delta t'$ is computed assuming the time shift factor is constant over Δt:

$$\Delta t' = \frac{\Delta t}{a_{t-\Delta t}}. \tag{6.39}$$

where the time shift factor $a_{t-\Delta t}$ in the free volume model is determined by

$$log\ a_{t-\Delta t} = \frac{-B_{t-\Delta t}}{2.303 f_{0,t-\Delta t}} \left[\frac{\alpha_{v,t-\Delta t}(T_{t-\Delta t} - T_0) + \epsilon_{v,t-\Delta t}}{f_{0,t-\Delta t} + \alpha_{v,t-\Delta t}(T_{t-\Delta t} - T_0) + \epsilon_{v,t-\Delta t}} \right]. \tag{6.40}$$

The volumetric strain in Equation (6.40) is also determined in the previous time step and stored as a state variable. The final form of the current strain E_t is obtained by substituting Equation (6.38) into Equation (6.37) and rearranging:

$$E_t = \bar{D}_t P_t - f_{t-\Delta t}, \tag{6.41}$$

where

$$\bar{D}_t = D_0 + \sum_{j=1}^{n} D_j - \sum_{j=1}^{n} D_j \frac{1 - e^{-\Delta t'/\rho_j}}{\Delta t'/\rho_j}, \tag{6.42}$$

$$f_{t-\Delta t} = \sum_{j=1}^{n} D_j \left[e^{-\Delta t'/\rho_j} q_{j,t-\Delta t} - \frac{1 - e^{-\Delta t'/\rho_j}}{\Delta t'/\rho_j} P_{t-\Delta t} \right]. \tag{6.43}$$

Equations (6.42) and (6.43) are dependent only on information at $t - \Delta t$ which is already known. For in-plane stresses, the discretized equations are

$$\begin{bmatrix} E_1 \\ E_2 \\ E_6 \end{bmatrix}_t = \begin{bmatrix} \bar{D}_{11} & \bar{D}_{12} & 0 \\ \bar{D}_{12} & \bar{D}_{22} & 0 \\ 0 & 0 & \bar{D}_{66} \end{bmatrix}_t \begin{bmatrix} P_1 \\ P_2 \\ P_6 \end{bmatrix}_t - \begin{bmatrix} f_1 \\ f_2 \\ f_6 \end{bmatrix}_{t-\Delta t}. \tag{6.44}$$

The current stress $[P]_t$ is inverted from the given strain $[E]_t$ in Equation 6.44.

6.4.3   Wrinkling Correction

The element state is determined from the computed stresses using the combined stress-strain criterion. Depending on the element state, the stresses and strains are recalculated differently.

For taut elements, no correction for stress or strain is needed. The stresses are calculated from the given strains as

$$
\begin{bmatrix} P_1 \\ P_2 \\ P_6 \end{bmatrix} = \begin{bmatrix} \bar{D}_{11} & \bar{D}_{12} & 0 \\ \bar{D}_{12} & \bar{D}_{22} & 0 \\ 0 & 0 & \bar{D}_{66} \end{bmatrix}^{-1} \begin{bmatrix} E_1 + f_1 \\ E_2 + f_2 \\ E_6 + f_6 \end{bmatrix}. \tag{6.45}
$$

For wrinkled elements, the wrinkling angle search procedure described in Section (**??** is used to find the wrinkling direction. The stresses in the wrinkle coordinate frame are then determined by

$$
\begin{bmatrix} \widehat{P}_1 \\ \widehat{P}_2 \\ \widehat{P}_6 \end{bmatrix} = \begin{bmatrix} \frac{\widehat{E}_1 + \widehat{f}_1}{\widehat{D}_{11}} \\ 0 \\ 0 \end{bmatrix} \tag{6.46}
$$

where the 1-axis and 2-axis are normal and parallel to the wrinkling direction respectively. To correct over-contraction in the direction transverse to wrinkle, the strain is recalculated from the corrected stress:

$$
\widehat{E}_2 = \widehat{\bar{D}}_{12} \widehat{P}_1 - \widehat{f}_2. \tag{6.47}
$$

For slack elements, the stresses in the current time step are set to zero,

$$
\begin{bmatrix} P_1 \\ P_2 \\ P_6 \end{bmatrix} = \begin{bmatrix} 0 \\ 0 \\ 0 \end{bmatrix}. \tag{6.48}
$$

However, the strains do not vanish instantaneously as in the case of elastic materials. Instead, they are computed from the deformation history as

$$
\begin{bmatrix} E_1 \\ E_2 \\ E_6 \end{bmatrix} = - \begin{bmatrix} f_1 \\ f_2 \\ f_6 \end{bmatrix}. \tag{6.49}
$$

For all elements, the corrected stresses and strains are then rotated back to the material coordinate frame for computing the through-thickness strain E_3:

$$
E_3 = \bar{D}_{13} P_1 + \bar{D}_{23} P_2 - f_3. \tag{6.50}
$$

6.5   Validation of Orthotropic Nonlinear Viscoelastic Model

The accuracy of the nonlinear viscoelastic model without wrinkling first was assessed by comparison to experimental data obtained from cyclic tests under controlled conditions. To avoid wrinkling,

test cases with uniform stress distribution were chosen and described in this section.

6.5.1   Experiments

Biaxial tension and in-plane shear experiments were conducted on cylindrical specimens with a diameter of 100 mm and height of 270 mm. The specimens were fabricated by bonding with a heat sealer two 38 μm thick rectangular pieces of StratoFilm 420. This construction technique provided two diametrically opposite seams that balance the stiffness distribution and thus avoid that the cylinder bends when it is loaded axially. Each end of the cylinders was bonded and clamped around the rim of a wooden disc acting as an end-fitting for connection with the load frame. The bottom fitting was equipped with two air ports for inflation and pressure measurements. Reflective targets were adhered to the cylinder surface for strain measurements using laser extensometers. A type-T thermocouple and a differential pressure transducer were used to monitor the temperature and pressure throughout the tests. The test setup is shown in Figure (6.11).
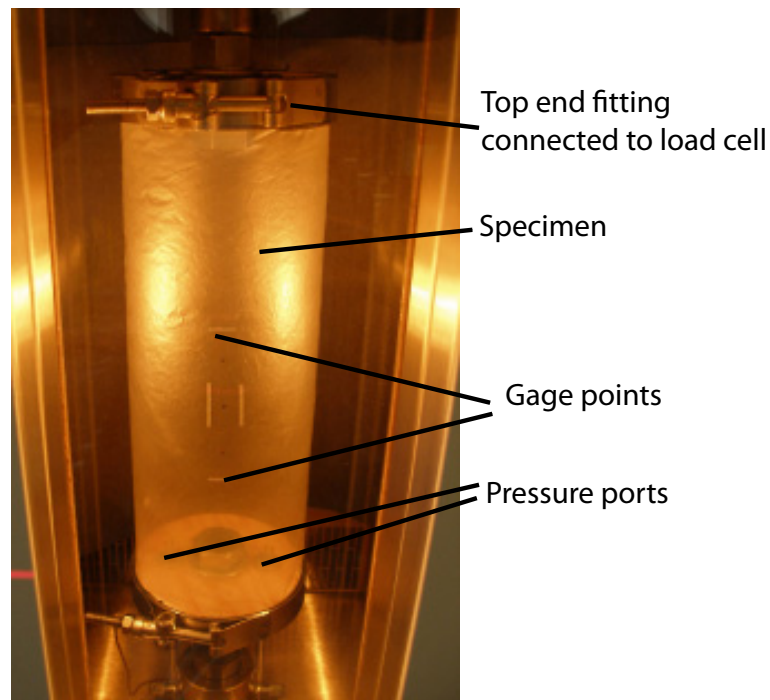
Figure 6.11. Cylindrical specimen mounted inside a thermal chamber.

For the biaxial tension tests, the cylinders were first inflated to the required pressure over a period of 10 s to provide hoop stress. Once the set pressure had been reached, the specimens were stressed axially by the load frame at a rate of 0.1 MPa/s for one cycle. For investigation of shear behavior, the cylinder was oriented such that the loading direction was at 45° from either material direction. This created a shear stress in the material frame of reference. The pressure, axial load, temperature, axial

Test	Type of test	Axial loading direction	Pressure [Pa]	Temperature [C]
1	Biaxial tension	Machine direction	700	-10
2	Biaxial tension	Transverse direction	400	0
3	In-plane shear	45° from machine direction	150	0

Table 6.3. Parameters of validation tests for nonlinear viscoelastic model.

and transverse strains were measured synchronously over time. The test conditions are summarized in Table 6.3.

6.5.2 Finite Element Analysis

A finite element model of the cylinder was constructed in to test the validity of the model and the numerical algorithm by comparing simulations with the tests conducted. The mesh consisted of 208 M3D4 square membrane elements. The constitutive behavior of the elements were defined with the free volume model described in Section 6.3 and Section 6.4, but with the wrinkling model deactivated. A material coordinate system was defined on all elements such that the material directions varied according to the load case being considered in Table 6.3.

Boundary conditions were imposed on the two ends of the cylinder. One end was fully constrained while the other was constrained in the radial direction, but free to translate in the axial direction. Geometrically nonlinear analyses were carried out. A uniform pressure was applied on all elements through the command *DLOAD and the axial load was imposed on the nodes at the partially constrained end using *CLOAD. The test conditions in Table 6.3 were replicated in the simulations.

6.5.3 Results Comparison

The stress-strain behavior for the biaxial tension and shear tests is plotted in Figs. (6.12)-(6.14), where it can be seen that the general features of each response have been satisfactorily reproduced. With the switch rule, the viscoelastic model treats loading and unloading differently. This allows the correct unloading path curvature to be predicted. It is worthwhile to mention that strain continues to increase with decreasing load for a short period of time before it reduces with load during unloading. This is a typical result of viscoelastic material under load control mode. The increase in strain in the initial part of the unloading segment is due to the prior loading, whose effect diminishes with time until the effect of unloading on the material eventually dominates. Close agreement is achieved between simulations and experimental data for the loading path for all three load cases presented. Despite having the correct curvature, the model predictions for the unloading path show some discrepancy with the measured response. In particular the model underestimates the strain and the errors in strain grow in size as the load decreases. In the fully unloaded state,

the discrepancies are about 1.5%, 1% and 2% for tests 1, 2 and 3 respectively. Good correlation is obtained also in the plots of strain response over time for both material directions (tests 1 and 2) as illustrated in Figs. (6.15) and (6.16), except for the same kind of discrepancy described earlier for the unloading path.
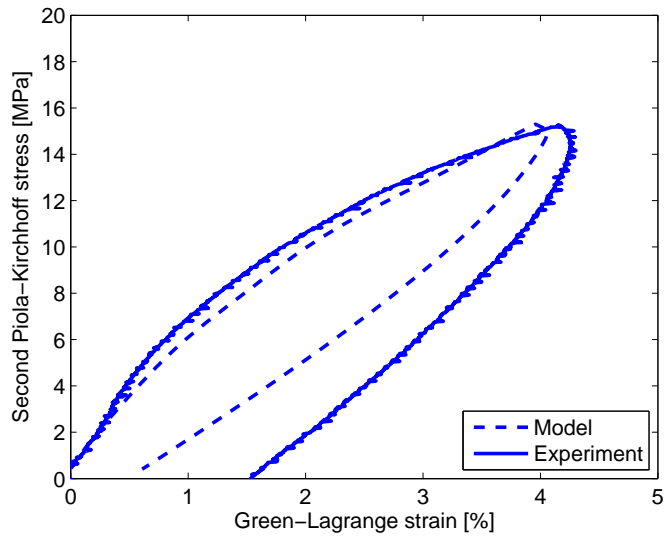
Figure 6.12. Stress vs. strain plots for test 1.
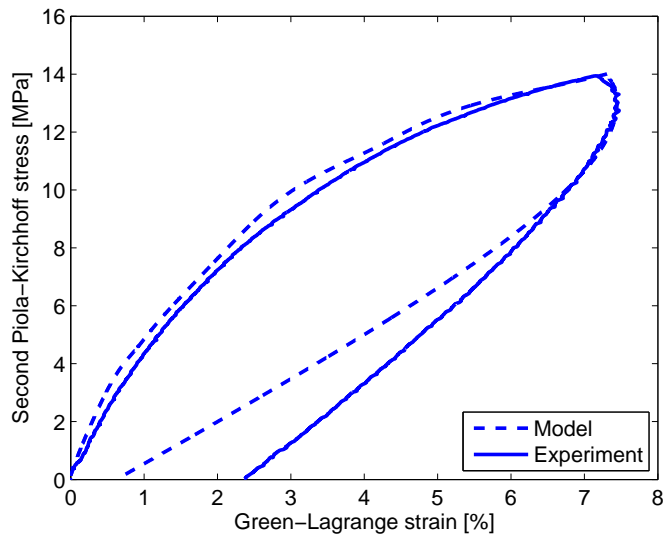
Figure 6.13. Stress vs. strain plots for test 2.
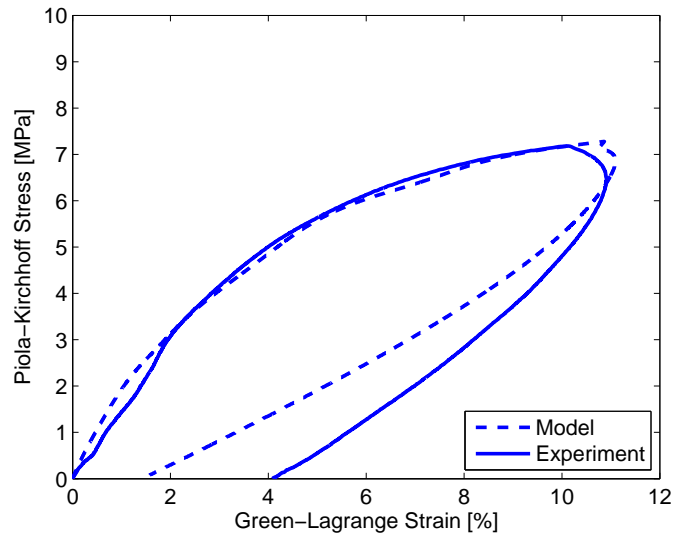
Figure 6.14. Stress vs. strain plots for test 3.
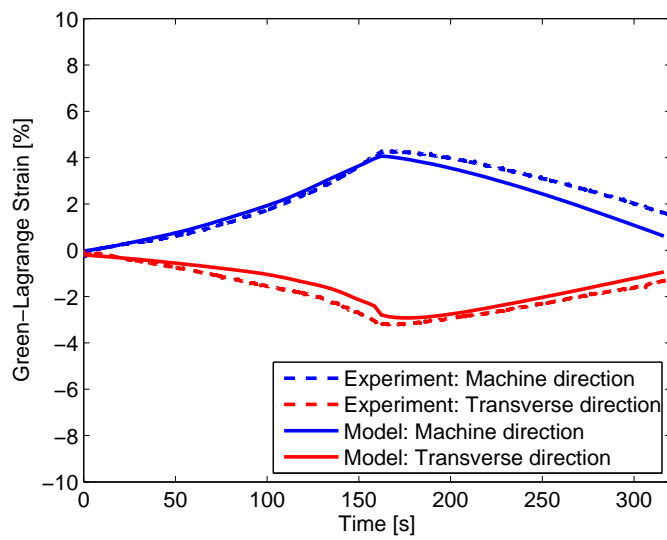
Figure 6.15. Strain vs. time plots for test 1.
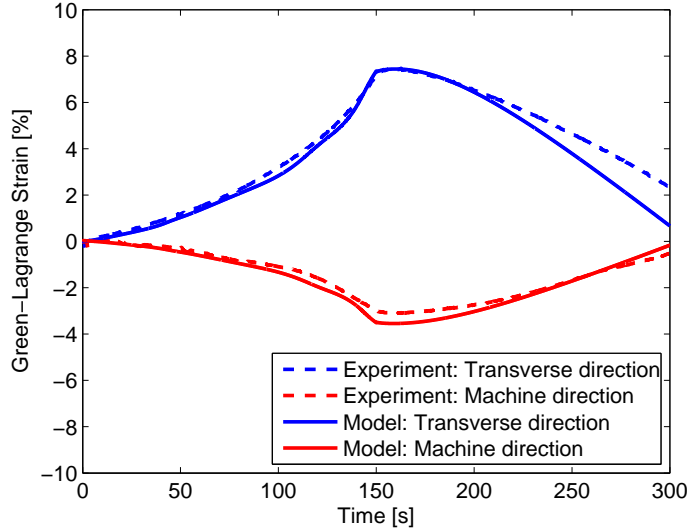
Figure 6.16. Strain vs. time plots for test 2.

6.6 Validation of Combined Nonlinear Viscoelastic and Wrinkling model

The accuracy of the proposed model was assessed by comparison to experimental measurements obtained from uniaxial stretch tests on StratoFilm 420 under a specified temperature and strain rate. As both nonlinear viscoelastic and wrinkling effects are present, this test serves as a verification for the proposed membrane model. This section describes the experimental configuration, specimen preparation, and finite element simulation techniques. Results from measurements and predictions are compared.

6.6.1 Experiments

Uniaxial tension tests were carried out on rectangular StratoFilm 420 specimens with a length of 250 mm, a width of 114 mm, and a thickness of 38 μm. An important step in specimen preparation is applying uniform clamping pressure on the two ends so that a uniaxial stress state is maintained in the middle region of the specimen. During preparation, a mist of water was first sprayed on a flat plastic sheet. A specimen with the required dimensions was put on the plastic sheet and lightly pressured with a hand roller to eliminate air bubbles. The specimen was held firmly against against the plastic sheet by the water surface tension at the interface. The top and bottom edges of the specimen were glued onto plastic plattens, which were clamped between metallic fixtures. Before mounting onto the testing machine, a black speckle pattern with a characteristic length of 2 mm was spray-painted onto the specimen for displacement measurements with digital image correlation.

Figure 6.17 shows the final specimen.

The experimental configuration is shown in Figure 6.18. The specimen was tested inside an environmental chamber. To correctly measure strains on a wrinkled surface, three-dimensional digital image correlation was employed. Digital image correlation is a non-contact technique that measures full-field displacements of a surface in three dimensional space. The system consists of two Point Grey Research CCD cameras with a resolution of 2448 x 2048 and a pixel size of 3.45 μm x 3.45 μm, each equipped with a lens with a focal length of 12 mm. The cameras were positioned to capture a series of images of the specimen through the window of the chamber. A lightbox was placed behind the specimen inside the chamber to illuminate the speckle pattern for displacement measurements.

The test proceeded as follows. The chamber was first cooled and stabilized at 0°C. To avoid disturbance of the optical path due to fogging at sub-ambient temperatures, the vicinity of the chamber window is constantly purged with dry nitrogen gas. The specimen was stretched to a nominal strain of 10% at a rate of 0.1%/s.

Figure 6.19 shows the measured out-of-plane displacement field of the stretched specimen. The displacement field measurements were obtained from analyzing images of the deformed specimens with the Vic-3D digital image correlation software. The principle of analysis is the following. A reference image is first chosen and divided into small square regions. The software then matches these regions between any subsequent image and the reference image based on pattern recognition algorithms and determine the movements of the regions between the two images. The result is then a displacement field for each image relative to the reference. The presence of wrinkling is apparent in Figure 6.19. The wrinkle amplitude is highest in the middle of the specimen and decreases towards the edges. Comparing the wrinkled shapes at nominal tensile strains of 5% and 10%, it is observed that the number of wrinkles increases with higher tensile strain, but the amplitude of the wrinkles is smaller.

6.6.2 Finite Element Simulations

By taking advantage of symmetry, only half of the rectangular film was modeled in Abaqus/Explicit. The finite element model is an uniform mesh of 720 quadrilateral membrane elements (M3D4). The membrane behavior was defined through the user subroutine VUMAT with both nonlinear viscoelastic and wrinkling behavior. The bottom edge of the model was held fixed while the top edge was given a displacement of 25 mm in 100 s. The prescribed displacement rate is sufficiently slow such that no spurious dynamic effects were observed.

Abaqus/Explicit is an explicit solver with conditional stability. The minimum time step required to satisfy the stability limit for the current simulation is 10^{-7} s. To speed up analysis, the mass of the finite element model was artificially scaled up so that a stable time increment of 10^{-4} s could

plastic plattens   specimen

lightbox
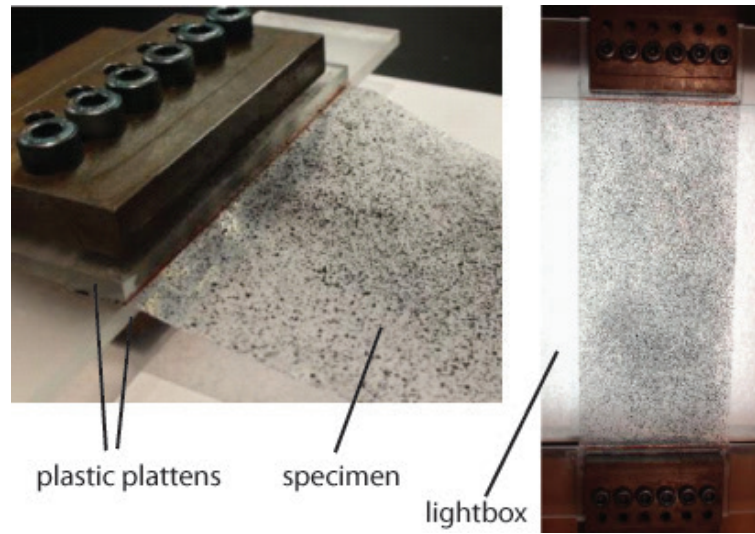
Figure 6.17. Specimen preparation showing the clamped boundary and the mounted configuration.

Thermal chamber mounted on materials testing machine

Balloon film specimen

Digital image correlation system
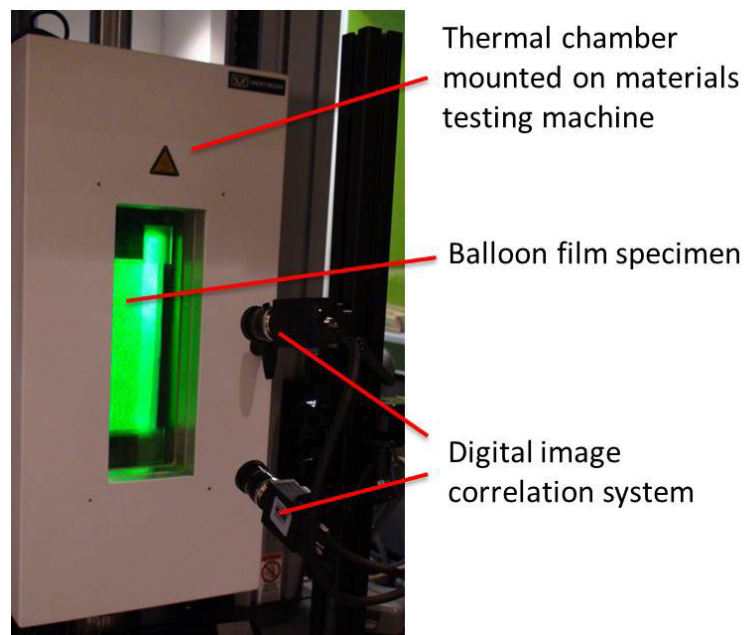
Figure 6.18. Experimental configuration.
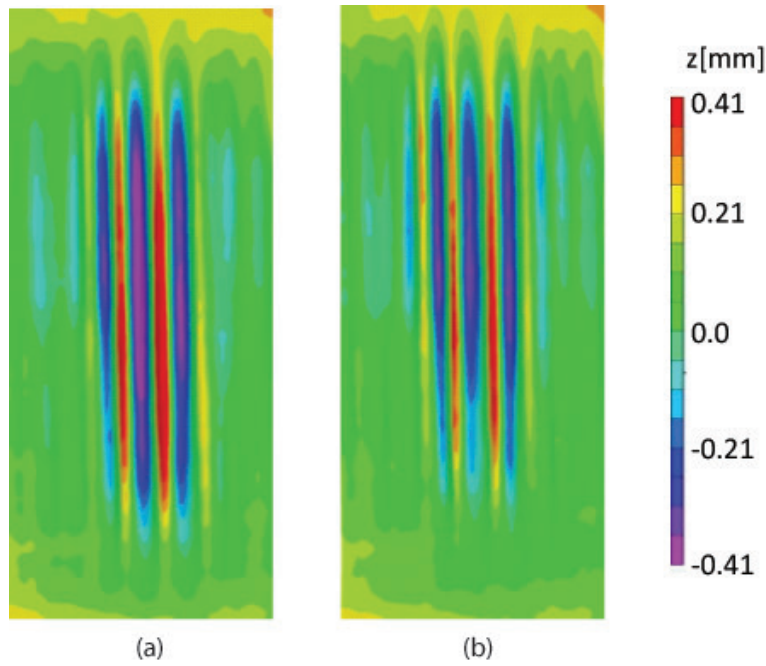
Figure 6.19. Measured out-of-plane displacements at a nominal strain of (a) 5%, and (b) 10%.

be achieved. The simulations results were not adversely affected because the problem is quasi-static and therefore the effects of inertia are insignificant.

6.6.3 Results Comparison

The transverse strain field at an overall longitudinal strain of 10% obtained from experimental measurements and finite element simulations are compared in Figure 6.20. The transverse strain determined from digital image correlation is the transverse strain component measured on the wrinkled surface and represents the actual material strain. Even though the wrinkles appear across the the membrane specimen, the transverse strain is effectively uniform. The three-dimensional deformation resulting from wrinkling does not have a significant effect on the in-plane behavior. This justifies the use of membrane approximation which only models homogeneous deformation within an element. A reasonable agreement is obtained between measured and predicted transverse strain fields. The stress-strain curves are compared in Figure 6.21, which shows that the proposed model which incorporates nonlinear viscoelastic and wrinkling behavior is capable of predicting the stress response accurately.
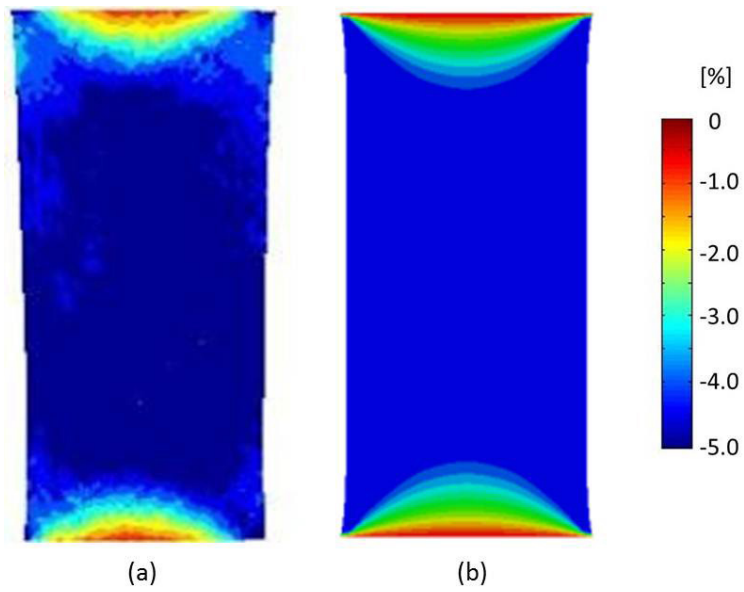
Figure 6.20. Comparison of transverse strain fields for uniaxial stretch at a rate of 0.1%/*s* and a temperature of 0°C at an overall longitudinal strain of 10%: (a) measured, and (b) predicted.
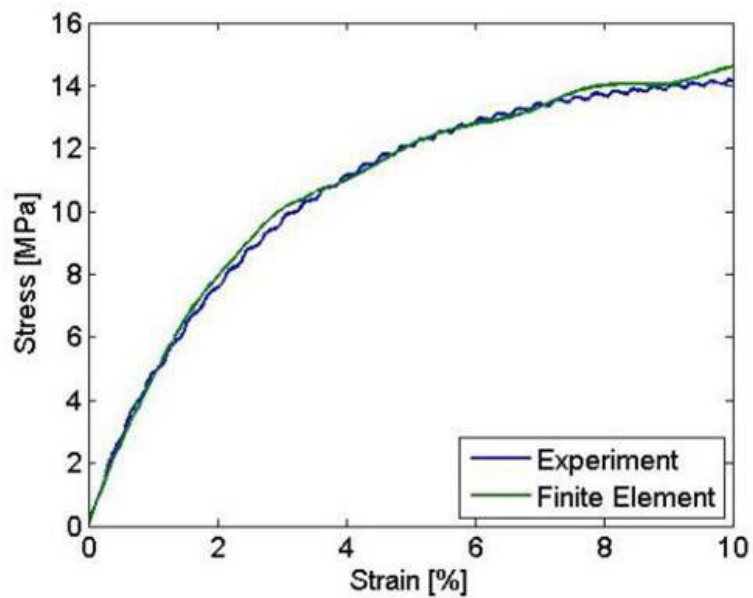
Figure 6.21. Comparison of stress-strain response for uniaxial stretch at a rate of 0.1%/*s* and a temperature of 0°C.

6.7 Thickness Variation in Balloon Films

Stress concentrations in balloon films resulting from sudden thickness changes are studied experimentally and numerically with the proposed nonlinear viscoelastic and wrinkling membrane model. The problem considered is applying a uniaxial tension on a rectangular film in which a small region has a higher thickness than the rest of the film. This aims to replicate the thickness variation at the junction of balloon envelope and tendon pockets. This section presents the construction of test specimens, experimental conditions, and details of finite element analysis. Experimental and numerical results are compared and important findings are discussed.

6.7.1 Experiments

The construction of test film specimen is shown in Figure 6.22. The thickness in the middle region of the rectangular film is increased by bonding 4 additional layers of film using an impulse heat sealer. The experimental configuration and procedure was identical to that described in Section 6.6. The film was stretched uniaxially at a rate of $0.1\%/s$ and at a temperature of $0°$C.

The deformed shape at a tensile strain of 2% is shown in Figure 6.23, where the wrinkling pattern is clearly affected by the introduction of a thicker region. Wrinkles appear only in the thinner region. The wrinkling direction is approximately aligned with the film diagonal at the corners of the thicker film region and is parallel to the loading direction at the end of section of the thicker region. This wrinkling pattern is consistent with the transverse strain field shown in Figure ??, where localized compressive strains are observed around the intersection region of the thicker and thinner regions. The longitudinal and shear strain distributions are shown in Figure 6.25 and Figure 6.26. Because of the sudden change in thickness, the longitudinal strain is redistributed locally at the termination of the thicker region. Along the film centerline, a jump in longitudinal strain is found in crossing from the thicker to the thinner region. The longitudinal strain discontinuity leads to localized shear deformation at the corners of the thicker region. All the strain components gradually spread out from the local concentration region.

The strain distributions suggests that significant shear lag effects result from the abrupt change thickness and hence sudden loss in tensile stress at the interface of the thicker and thinner regions along the centerline. The excess stress needs to be carried by shear on the two sides of the thicker region.

6.7.2 Finite Element Analysis

For finite element analysis, half of the film was modeled with 1578 triangular membrane elements (M3D3) with a minimum element edge length of 0.25 mm. The finite element mesh is shown in Figure 6.27. The mesh density is increased in the region of local concentration to capture the high
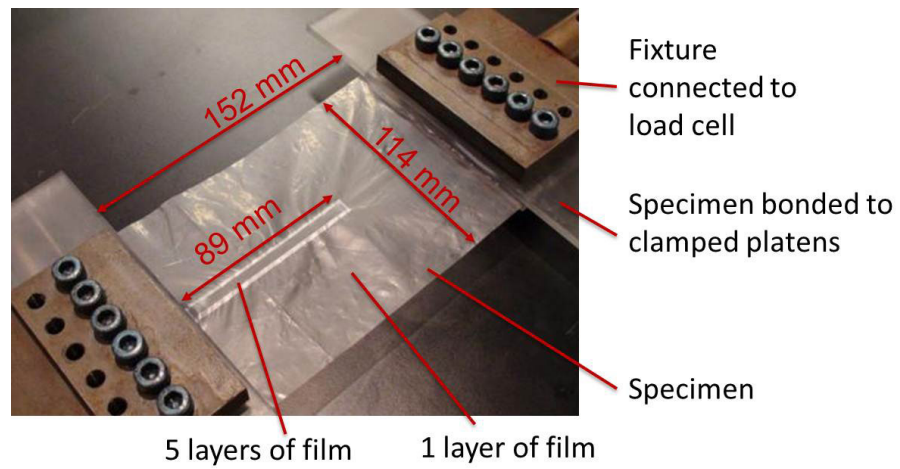
Figure 6.22. Balloon film specimen with thickness variation.
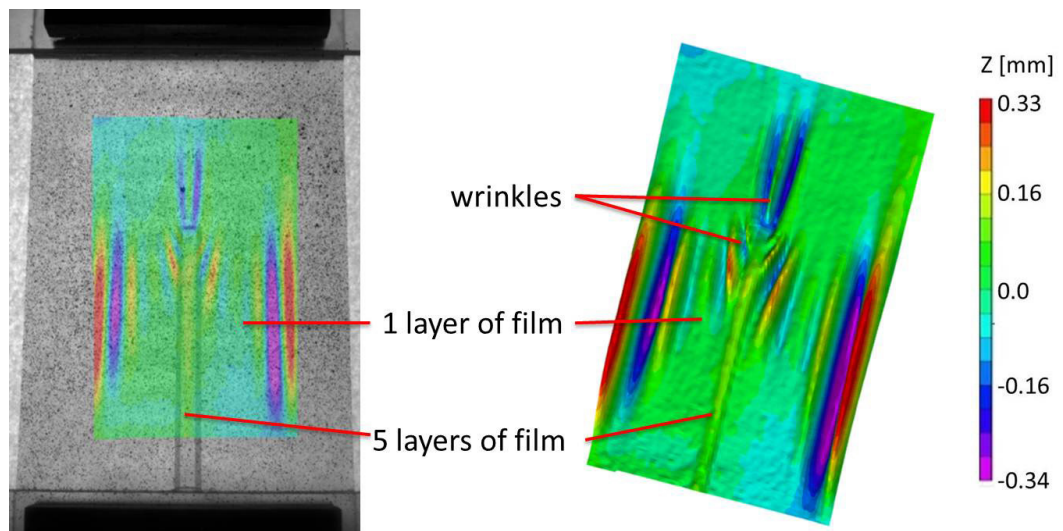
Figure 6.23. Measured out-of-plane deformation of balloon film with thickness variation at a tensile strain of 2%: (a) two-dimensional plot superimposed on the specimen image, and (b) three-dimensional deformed shape.
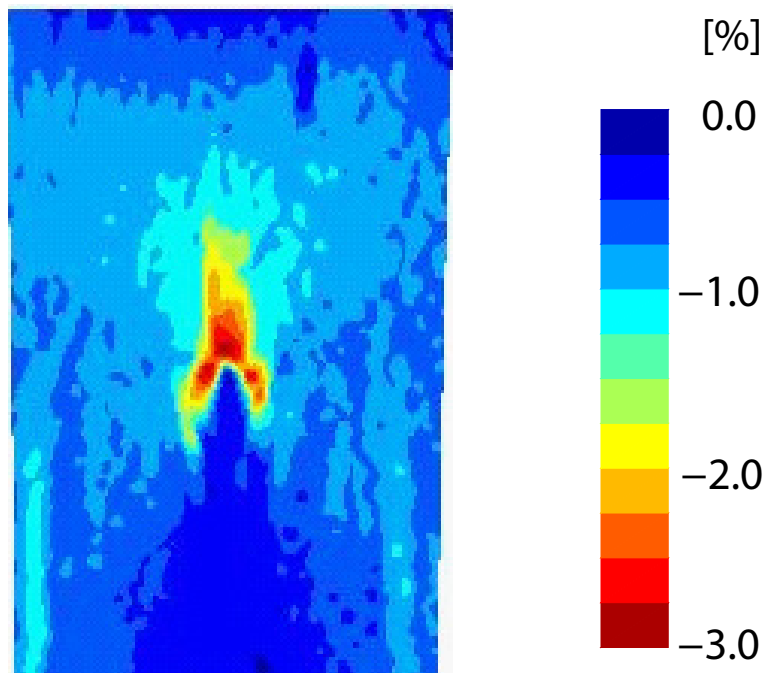
Figure 6.24. Measured transverse strain distribution at an average tensile strain of 2%.
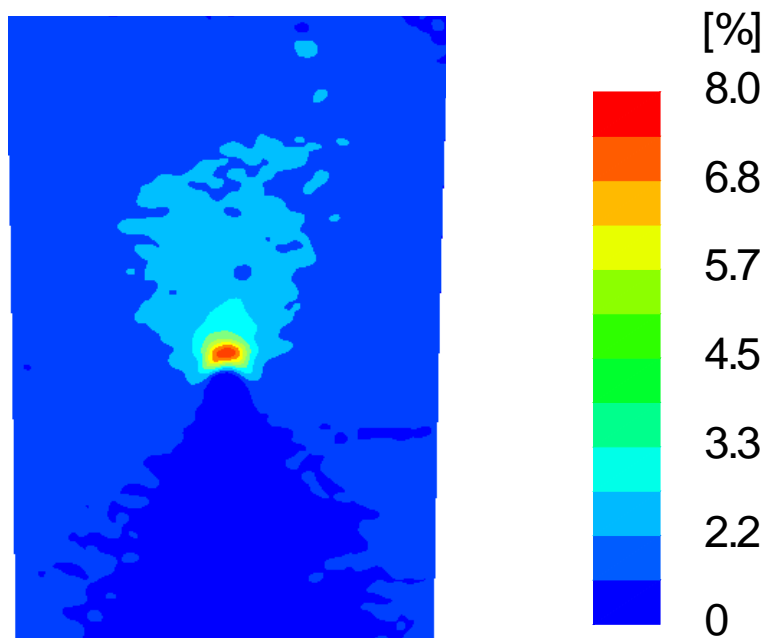
Figure 6.25. Measured longitudinal strain distribution at an average tensile strain of 2%.
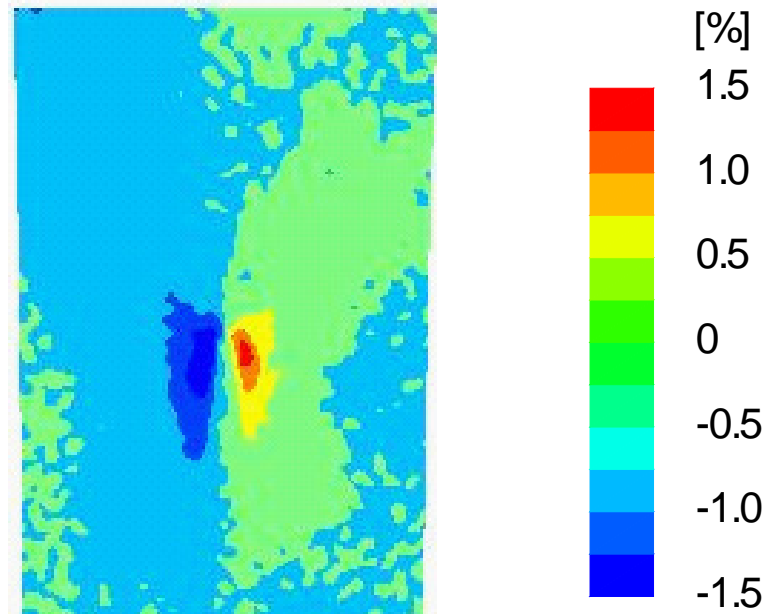
Figure 6.26. Measured shear strain distribution at an average tensile strain of 2%.

strain gradients. The constitutive behavior of the elements and the mass scaling techniques described in Section 6.6 were employed. The thickness of the red region was defined to be 5 times of that of the grey region in Figure 6.27. In the analysis, the bottom edge of the model was held fixed while a displacement of 15.2 mm was imposed on the top edge linearly over 100 s.
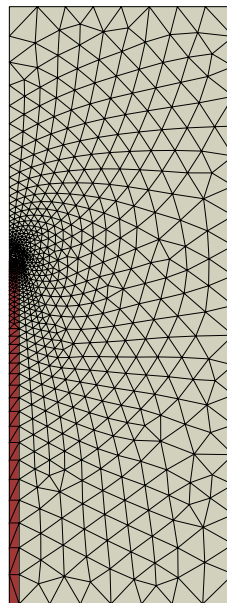
Figure 6.27. Finite element model.

6.7.3   Results Comparison

The longitudinal strain distributions from experimental measurements and finite element analysis are compared in Figure 6.28 and Figure 6.29. Good agreement is achieved for both the longitudinal and transverse strain distributions. At the local concentration region, the model predicts a jump in strains while the experimental measurements show a continuous change in strain. This is because local averaging is performed during strain computation in digital image correlation and the strain variation resulted is smoothed.

To quantify more precisely the strain concentration due to thickness change, a plot of longitudinal strain profile along the centerline of the specimen is shown in Figure 6.30. The longitudinal strain in the thicker region is always lower than the applied strain of 2% while the opposite is true for the thinner region. At the location of sudden thickness reduction, the strain jumps from 0.5% to 8.0%. The strain approaches the applied value towards the two ends. A concentration factor of 4 is found for the present case where the thickness difference is 5 times. A similar profile is observed for transverse strain along the centerline as shown in Figure 6.31. The transverse strain tends to zero on the two ends because of the clamp constraints. A maximum strain of -3.4% is reached.
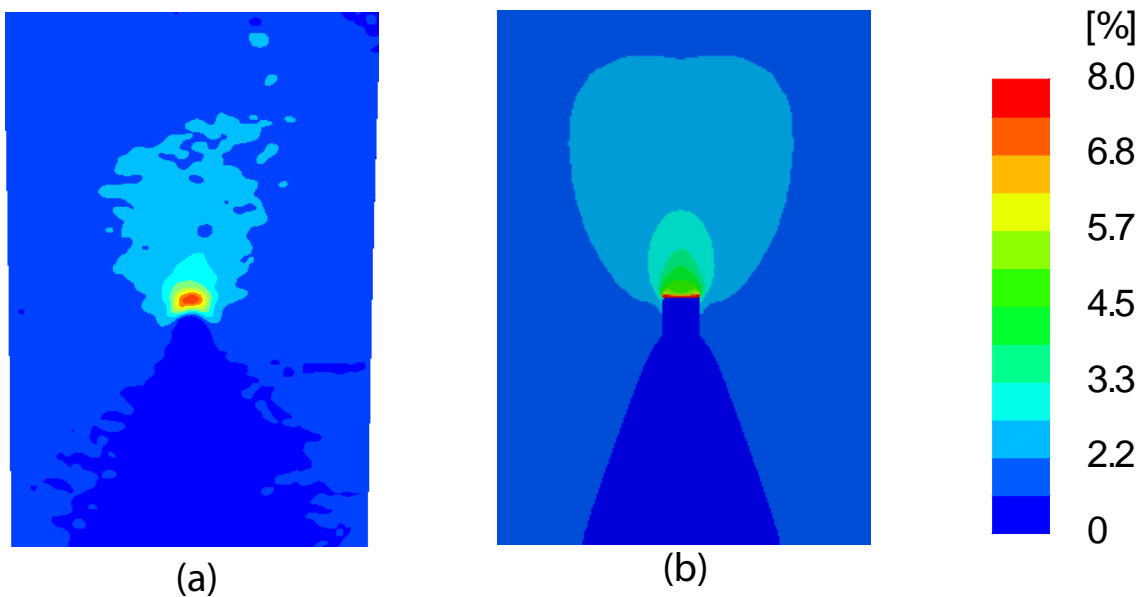
Figure 6.28. Longitudinal strain field with an applied strain of 2%: (a) measured, and (b) predicted.
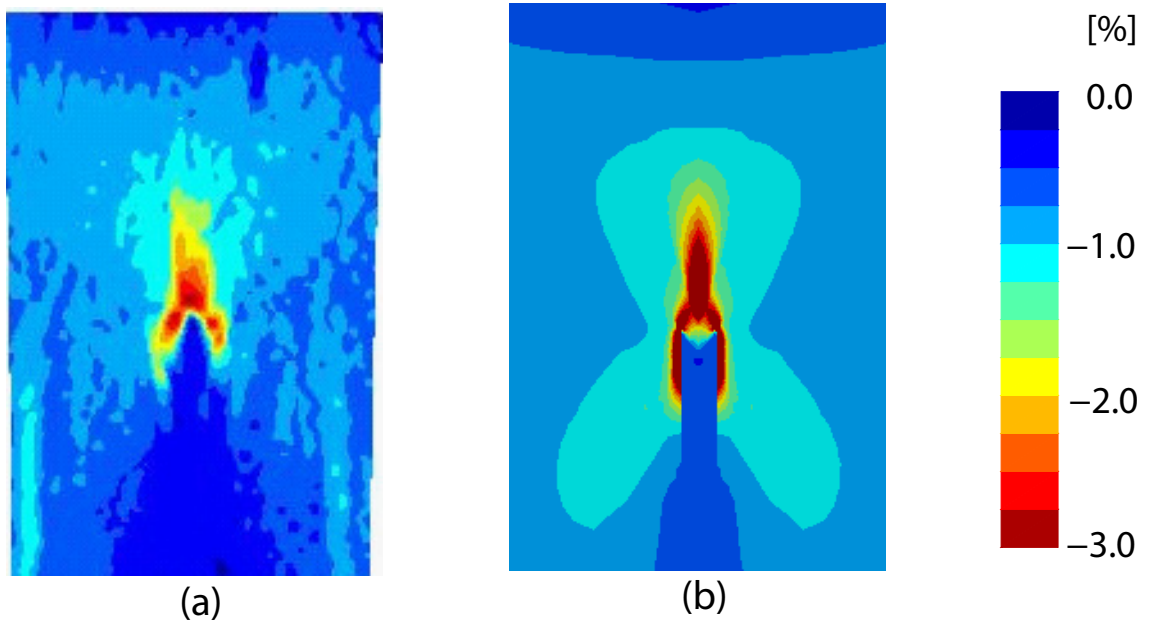
Figure 6.29. Transverse strain field with an applied strain of 2%: (a) measured, and (b) predicted.
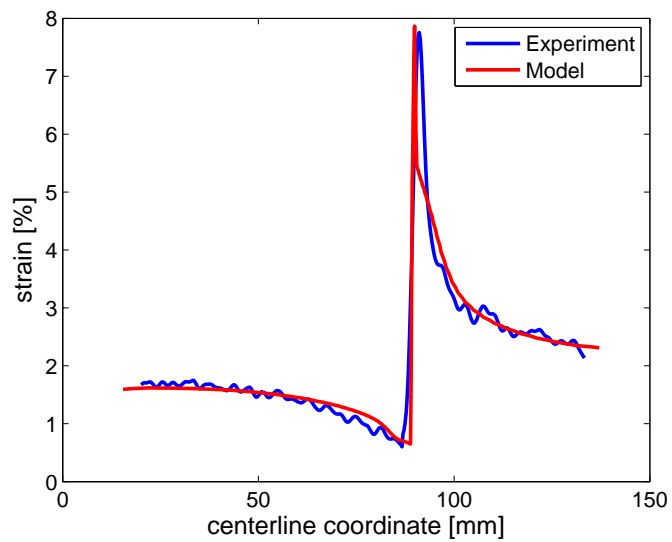
Figure 6.30. Longitudinal strain along centerline of balloon film.
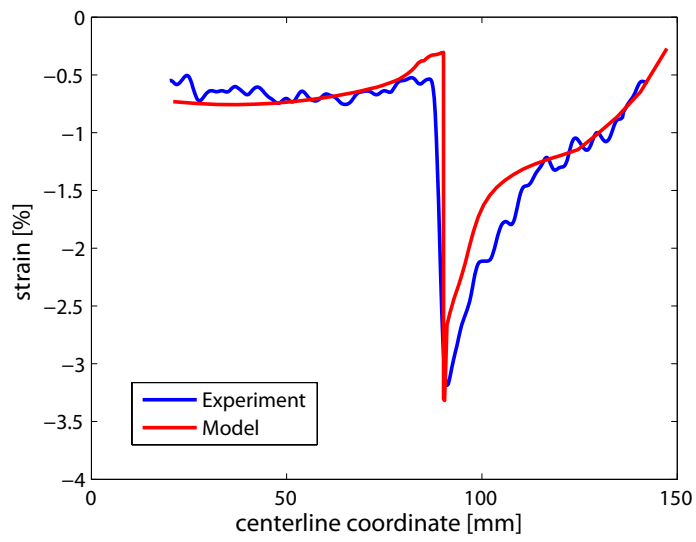
Figure 6.31. Transverse strain along centerline of balloon film.

Chapter 7

Conclusions

This chapter discusses the achievements and limitations of the present work. It also suggests potential directions for future research.

7.1 Findings and Discussion

A detailed analysis of the shape recovery behavior of a homogeneous linear viscoelastic beam after being held at a constant deflection under quasi-static conditions has been presented. Closed-form solutions for both force relaxation and shape recovery were obtained assuming the solutions are spatial-temporal separable. Relaxation behavior during stowage can lead to a significant reduction in internal force, which determines the amount of instantaneous recovery upon removal of the deflection constraint. The long term recovery response of a viscoelastic beam shows asymptotic behavior over time and depends strongly on temperature and holding duration. The recovery time increases with stowage temperature and duration, but the effects diminish with time. The time and temperature effects can be concisely represented on a master curve relating stowage time and recovery time in the reduced time scale for a given material. The simple expressions for load and deflection resulting from the analysis show close agreement with finite element simulations that model the finite amount of time required to impose each change in boundary conditions as well as experimental results.

The analytical relations presented are limited to one-dimensional structures in which spatial-temporal separable solutions are permissible. The applicability of the results are thus limited to problems involving quasi-static loading, homogeneous materials, and uniform spatial temperature distribution throughout the structure. Nonetheless, they provide an intuitive understanding of the shape recovery process and are useful for choosing materials for recovery performance. The simple closed-form solutions provide a starting point for understanding shape recovery in more complicated structures.

The nonlinear behavior of open cylindrical shells made of homogeneous polymer materials under bending has been studied with respect to the effects of time and temperature. Open cylindrical shells

can be folded to high curvatures by triggering a local instability and the resulting nonlinear load-displacement relationship is characterized by a limit load and a propagation load. Both the limit and the propagation load increase with folding rate but decrease with temperature. The behavior in the stowed configuration is characterized by significant load relaxation. This indicates the loss over time of the available deployment force over time for shells subject to long term stowage.

The behavior of these shells after stowage encompasses three distinct stages. The first is a weak dynamic response accompanied by a low magnitude vibration. This short dynamic phase is followed by a steady deployment that returns the shell to almost the straight deployed configuration but with a slight overshoot. A complete shape recovery requires a final slow creep recovery of the fold cross section. An interesting feature is that the fold remains stationary throughout deployment. These features are distinct from elastic shells, which show much stronger dynamic response and a localized fold that travels along the shell during deployment. The difference can be explained by the inherent energy dissipation in viscoelastic structures. Because of load relaxation, the energy stored in folding the shell is dissipated over time and the internal force is too low to cause significant dynamics. An advantage of this effect is that the deployment process becomes more steady and the risk of damage due to dynamic events is decreased. However, the internal force may drop to a point that is not sufficient to bring the structure back to the original configuration.

The continuous folding, stowage, deployment, and shape recovery processes have been analyzed with a finite element model that incorporates a linear isotropic viscoelastic material model with an experimentally determined master curve. The material model constitutes of a six-term Prony series and a Williams-Landel-Ferry type temperature shift function. The finite element model uses shell elements with thickness defined by the measured thickness distribution of tested specimens to closely capture the instability in load response. The finite element model captures the experimentally measured behavior, including the effects of rate and temperature in the nonlinear load-displacement response during folding, load relaxation over an extended stowage duration, and short term deployment as well as long term shape recovery. Good qualitative and quantitative results in modeling the viscoelastic and nonlinear behavior of shells under quasi-static and dynamic situations have been demonstrated.

A micromechanical finite element modeling framework for determining the homogenized viscoelastic properties of woven composite laminas made from linear elastic fibers and viscoelastic matrix has been developed. In the modeling framework, unit cell homogenization is carried out at both the tow level and the lamina level to capture the microscopic details of the composite laminas. The microscopic geometric and compositional information have been obtained from examination of photomicrographs of woven composite laminas fabricated in-house using an autoclave. At the tow level, the viscoelastic behavior of a unidirectional tow is determined from the constituent fiber and matrix properties, which have been experimentally characterized. A uniform distribution of fibers

has been assumed. Since the fiber volume fraction is higher at the tow level, the effect of the fiber distribution is minor. The outcome of the unit cell analysis is a transversely isotropic viscoelastic model of a tow. The results from the tow level homogenization serve as the input for the lamina unit cell which is composed of wavy viscoelastic tows connected by regions of pure epoxy matrix. A sinusoidal shape has been assumed for the tow geometry. The lamina has been homogenized to a viscoelastic Kirchhoff plate with a viscoelastic ABD matrix. The homogenized properties have been verified with a series of tension and bending creep tests at several temperatures.

In the proposed modeling framework, the composite has been assumed to be thermorheologically simple and its temperature dependent behavior is the same as that of the matrix. This assumption is generally not true for heterogeneous materials made of phases with distinct molecular structures. Perfect interfacial bonding has been assumed in the unit cell finite element modeling. It has been suggested that a thin interfacial region having mechanical properties different from the constituents exists because the molecular structures are altered when two constituents adhere. As good agreement has been obtained between model predictions and experimental results, it is concluded that in the present case this microscopic interfacial bonding effect is secondary. The micromechanical model presented is limited to linear viscoelastic behavior only. Since the difference in modulus between carbon fibers and epoxy matrix is generally more than 10 times, locally nonlinear deformation in the interfacial regions is possible when the composite is subject to larger overall deformation. The model predictions based on the assumption of linearity would produce an over-estimation of composite modulus.

The viscoelastic micromechanical model developed for woven composite shells has been applied to study the stowage effects of a composite tape-spring. Based on the time-temperature superposition principle, stowing composite tape-springs at higher temperatures is equivalent to extending the stowage time. This principle has been exploited to investigate the effects of different stowage times by varying the stowage temperatures. Finite element analyses of deployment and shape recovery behavior after stowage for different stowage and deployment temperatures have been carried out. Also, deployment and shape recovery experiments have been conducted on composite tape-springs in a controlled temperature environment and compared with model predictions. It has been found that a tape-spring deploys quickly and overshoots the deployed configuration by a small amount, and then moves slowly towards its final reference configuration. The short-term deployment is dependent mainly on the stowage conditions and insignificantly affected by the deployment conditions. The full shape recovery from the overshoot position to the fully deployed state takes place in an asymptotic manner. Stowing a composite tape-spring has the effect of extending the time required for deployment and shape recovery. The observed behavior has been well predicted by finite-element simulations based on the micromechanical composite shell model. The effects of long-term stowage on the deployment of composite tape-springs were studied with finite element analysis. For the spe-

cific case in which the tape-spring deploys against gravity after it is stowed for 1 year, the analysis has shown that deployment is never completed.

As mentioned before, the micromechanical model used for the simulation of tape-springs is linear viscoelastic. For composite tape-springs made of several plies, the maximum strain reached is potentially beyond the range of validity of linear viscoelastic models. Simulations of long-term stowage effects are based upon the principle of time-temperature superposition. The predicted results therefore rely on how precisely the master curve has been constructed and on the time range of validity of the time-temperature superposition principle. The behavior of tape-springs under thermal cycles during stowage has not been investigated and the effects of long-term stowage have been assumed to be due to viscoelasticity of the matrix only. Other effects such as physical and chemical ageing, degradation due to moisture have not been considered.

A membrane model that captures the nonlinear viscoelastic and wrinkling behavior of polymer balloon films has been established. The model is capable of predicting the large strain and wrinkling behavior of StratoFilm 420, which is the film currently used for NASA superpressure balloons. The model is formulated in terms of finite kinematics using the single integral approach. For the nonlinear viscoelastic model, the free volume theory is generalized for orthotropic materials and applied to StratoFilm 420. The nonlinear behavior is incorporated through a time shift function that is dependent on the volumetric strain. A switching rule that distinguishes between loading and unloading behavior is included into the model and found capable of predicting the correct curvature of the unloading path, a feature that had not been previously captured by nonlinear viscoelastic models. For membrane wrinkling, an orthotropic wrinkling model that corrects the stress and strain states of wrinkled elements is established for nonlinear viscoelastic materials. The orthotropic nonlinear viscoelastic and wrinkling models have been combined and implemented in the finite element solver Abaqus as a user-defined subroutine. The computational scheme is based on a recursive algorithm which results in efficient computation.

Two sets of validation tests have been conducted to verify the proposed membrane model. The first set aims at validating the nonlinear viscoelastic behavior only. In this validation, model predictions of cyclic biaxial tension and shear stress states have been compared with experiments conducted on inflated cylindrical specimens under controlled thermal conditions. The results show good agreement between experiments and numerical simulations, except that the model consistently overestimates the strain recovery during unloading; this discrepancy increases as the specimen gradually approaches the zero stress configuration. Since the model had been "calibrated" against the loading parts only of two tension tests, it is not surprising that the unloading predictions are less accurate. The second set of tests aims to verify the combined viscoelastic and wrinkling model. For this model validation, uniaxial stretch test on StratoFilm 420 has been conducted. The strain fields on the wrinkled surface have been measured by a technique based on three-dimensional digi-

tal image correlation. Comparisons between transverse strain fields and stress-strain response have demonstrated good model accuracy.

The material parameters of StratoFilm 420 in the thickness direction need to be characterized for implementing the nonlinear viscoelastic model. Because of the experimental difficulty associated with the small thickness of the film, the required parameters have been obtained by fitting model predictions to in-plane test data at a particular temperature. Even though the model provides good predictions at temperatures near the temperature for model calibration, it is expected that its accuracy will deteriorate at temperatures away from the calibration point.

Stress concentrations arising from sudden thickness variation in balloon films have been studied with finite element analysis using the proposed membrane model and experiments. Thickness variation has been introduced into balloon films by bonding additional layers thus creating stress concentration regions when the films are subject to tension. Because of the sudden change in stiffness at the intersection of thick and thin regions, significant shear lag effects have been observed and cause heavy wrinkling in the region. The longitudinal strain is locally redistributed at the location of concentration. A strain concentration factor of 4 is found for the case of a thickness difference of 5 times. The membrane model has accurately captured the strain fields and quantitatively reproduced the strain discontinuity.

The membrane model is limited to nonlinear viscoelastic behavior and therefore fails to capture any viscoplastic effects which are expected at higher overall applied strain and larger thickness difference. Rupture of the film at locations of stress concentrations is important for the design for superpressure balloons, but has not been considered in this thesis.

The primary contribution of this thesis is the development and validation of general modeling techniques for viscoelastic shells and membranes that are applicable for study of time and temperature dependent behavior in thin-walled structures. This thesis has also characterized stowage effects in deployable structures and stress concentrations in balloon structures using the established modeling and experimental techniques. The work presented can serve to derive guidelines for design improvement.

7.2   Future Work

A number of future research directions have been identified in the course of this research.

As mentioned in the previous section, the micromechanical model developed in this thesis has been limited to linear viscoelastic behavior. To take into account possible nonlinear behavior at higher strain, it would be useful to incorporate a nonlinear viscoelastic model to describe the matrix behavior. The free volume model used for the balloon film in this thesis can potentially applied to model the matrix. An advantage of this model is that environmental effects such as moisture

degradation and physical ageing can be incorporated into the model through the time shift function.

At high temperatures or over long time scales, the matrix may become sufficiently soft that the deformation of the stiff fibers is geometrically nonlinear. At such point it would be important to include geometric nonlinear behavior of the fibers in the micromechanical modeling. The assumption of periodicity used in unit cell homogenization imposes stringent restrictions on the deformation. A more general framework for nonlinear homogenization is necessary to model such geometrically nonlinear effects.

The mechanical properties of the matrix has been assessed only through constant temperature creep tests. It would be beneficial to investigate experimentally the matrix behavior under thermal cycles as well as cyclic loads.

Mechanical properties of balloon films have been characterized only at relatively high temperatures with respect to the flight temperature of superpressure balloons. More experimental data at lower temperatures are needed. The ultimate stresses and strains are especially important to characterize the failure behavior of balloon films.

To predict balloon film behavior up to the point of failure, it would be useful to incorporate a viscoplastic model in the established nonlinear viscoelastic model to provide a viscoelastic-viscoplastic constitutive description of the balloon film. It is also important to develop a failure criterion that can be assimilated into the current membrane model to predict failure of balloon films at regions of stress concentrations.

Finally, it would be interesting to investigate numerically the behavior of a full-scale balloon under flight conditions using the nonlinear viscoelastic model established in this thesis and carry out detailed simulations for particular regions of the balloons where stress concentrations arise.

Bibliography

D.S. Adams and M. Mobrem. Lenticular jointed antenna deployment anomaly and resolution on-board the mars express spacecraft. *Journal of Spacecrafts and Rockets*, 46:403–408, 2009.

T. Alfrey. Nonhomogeneous stress in viscoelasticity. *Quarterly of Applied Mathematics*, 2:113–119, 1944.

G.A. Arzoumanidis and K.M. Liechti. Linear viscoelastic property measurement and its significance for some nonlinear viscoelasticity models. *Mechanics of Time-Depdendent Materials*, 7:209–250, 2003.

H.F. Brinson and L.C. Brinson. *Polymer Engineering Science and Viscoelasticity*. Springer, New York, 2008.

L.C. Brinson and W.G. Knauss. Finite element analysis of multiphase viscoelastic solids. *Journal of Applied Mechanics*, 59:730–737, 1992.

C.R. Calladine. The theory of thin shell structures 1888-1988. *Proceedings of the Institution of Mechanical Engineers*, 202:1–9, 1988.

J. Capodagli and R.S. Lakes. Isothermal viscoelastic properties of pmma and ldpe over 11 decades of frequency and time: a test of time-temperature superposition. *Rheologica Acta*, 47:777–786, 2008.

E. Chater and J.W. Hutchinson. On the propagation of bulges and buckles. *Journal of Applied Mechanics*, 51:269–277, 1984.

R.M. Christensen. *Theory of Viscoelasticity: An Introduction*. Academic Press, New York, second edition, 1982.

B.D. Coleman and W. Noll. Foundations of linear viscoelasticity. *Reviews of Modern Physics*, 33: 239–249, 1961.

M.I. Daniel and O. Ishai. *Engineering Mechanics of Composite Materials*. Oxford University Press, 2006.

J.L. Domber, J.D. Hinkle, L.D. Peterson, and P.A. Warren. Dimensional repeatability of an elastically folded composite hinge for deployed spacecraft optics. *Journal of Spacecraft and Rockets*, 39:646–652, 2002.

A.K. Doolittle. Studies in newtonian flow. ii the dependence of the viscosity of liquids on free-space. *Journal of Applied Mechanics*, 22:1471–1475, 1951.

M. Epstein and M.A. Forcinito. Anisotropic membrane wrinkling: theory and analysis. *International Journal of Solids and Structures*, 38:5253–5272, 2001.

J.D. Ferry. *Viscoelastic Properties of Polymers*. John Wiley and Sons, New York, third edition, 1980.

W. Flugge. *Viscoelasticity*. Springer-Verlag, New York, 1975.

T. Gerngross, Y. Xu, and S. Pellegrino. Viscoelastic behavior of pumpkin balloons. *Advances in Space Research*, 42:1683–1690, 2008.

S. Govindarajan, N.A. Langrana, and G.J. Weng. An experimental and theoretical study of creep of a graphite/epoxy woven composite. *Polymer Composites*, 17:353–361, 1996.

G.A.C. Graham. The contact problem in the linear theory of viscoelasticity. *International Journal of Engineering Science*, 3:27–46, 1965.

R.M. Haj-Ali and A.H. Muliana. Numerical finite element formulation of the schapery nonlinear viscoelasic material model. *International Journal for Numerical Methods in Engineering*, 59:25–45, 2004.

Z. Hashin. Viscoelastic behavior of heterogeneous media. *Journal of Applied Mechanics*, 32E:630–636, 1965.

Z. Hashin. Viscoelastic fiber reinforced materials. *AIAA Journal*, 1966.

M. Henriksen. Nonlinear viscoelastic stress analysis - a finite element approach. *Computers and Structures*, 18:133–139, 1984.

H.H. Hilton. The significance of (an)isotropic viscoelastic poisson ratio stress and time dependencies. *International Journal of Solids and Structures*, 35:3081–3095, 1998.

H.H. Hilton. Implications and constraints of time-independent poisson ratios in linear isotropic and anisotropic viscoelasticity. *Journal of Elasticity*, 63:221–251, 2001.

G.A. Holzapfel. *Nonlinear Solid Mechanics*. John Wiley and Sons, Chichester, 2000.

S.C. Hunter. The hertz problem for a rigid spherical indentor and a viscoelastic half-space. *Journal of Mechanics and Physics of Solids*, 8:219–234, 1960.

S.C. Hunter. The rolling contact of a rigid cylinder with a viscoelastic half-space. *Journal of Applied Mechanics*, 28:611–617, 1961.

S. Kang and S. Im. Finite element analysis of wrinkling membranes. *Journal of Applied Mechanics*, 64:263–269, 1997.

W.G. Knauss. The sensitivity of the time-temperature shift process to thermal variations - a note. *Mechanics of Time-Dependent Materials*, 12:179–188, 2008.

W.G. Knauss and I.J. Emri. Nonlinear viscoelasticity based on free volume consideration. *Computers and Structures*, 13:123–128, 1981.

W.G. Knauss and I.J. Emri. Volume change and the nonlinearly thermo-viscoelastic constitution of polymers. *Polymer Engineering and Science*, 27:86–100, 1987.

S. Kyriakides. Propagating instabilities in structures. In J.W. Hutchinson and T.Y. Wu, editors, *Advances in Applied Mechanics*, 1994.

J. Lai and A. Bakker. 3-d schapery representation for nonlinear viscoelasticity and finite element implementation. *Computational Mechanics*, 18:182–191, 1996.

R.S. Lakes. On poisson's ratio in linearly viscoelastic solids. *Journal of Elasticity*, 85:45–63, 2006.

E.H. Lee. Stress analysis in viscoelastic bodies. *Quarterly of Applied Mathematics*, 13:183, 1955.

E.H. Lee and J.R.M. Radok. The contact problem for viscoelastic bodies. *Journal of Applied Mechanics*, 27:438–444, 1960.

E.H. Lee, J.R.M. Radok, and W.B. Woodward. Stress analysis for linear viscoelastic materials. *Transactions of the Society of Rheology*, 3:41–59, 1959.

S. Lee and W.G. Knauss. A note on the determination of relaxation and creep data from ramp tests. *Mechanics of Time-Dependent Materials*, 4:1–7, 2000.

M. Levesque, M.D. Gilchrist, N. Bouleau, K. Derrien, and D. Baptiste. Numerical inversion of the laplace-carson transform applied to homogenization of randomly reinforced linear viscoelastic media. *Computational Mechanics*, 40:771–789, 2007.

H. Lu, X. Zhang, and W.G. Knauss. Uniaxial, shear, and poisson relaxation and their conversion to bulk relaxation: studies on poly(methyl methacrylate). *Polymer Engineering and Science*, 37: 1053–1064, 1997.

N.G. McCrum, C.P. Buckley, and C.B. Bucknall. *Principles of Polymer Engineering*. Oxford Science Publications, Oxford, second edition, 2003.

Y. Miyazaki. Wrinkle/slack model of membrane. *International Journal for Numerical Methods in Engineering*, 66:1179–1209, 2006.

M. Mobrem and D.S. Adams. Deployment analysis of lenticular jointed antennas onboard the mars express spacecraft. *Journal of Spacecrafts and Rockets*, 46:394–402, 2009.

L.W. Morland. A plane problem of rolling contact in linear viscoelasticity theory. *Journal of Applied Mechanics*, 29:345–352, 1962.

L.W. Morland. Exact solutions for rolling contact between viscoelastic cylinders. *Quarterly Journal of Mechanics and Applied Mathematics*, 20:73–106, 1967.

N.P. O'Dowd and W.G. Knauss. Time dependent large principal deformation of polymers. *Journal of Mechanics and Physics of Solids*, 43:771–792, 1995.

S. Pellegrino. Large retractable appendages in spacecrafts. *Journal of Spacecrafts and Rockets*, 32:1006–1014, 1995.

A.C. Pipkin. The relaxed energy for isotropic elastic membranes. *IMA Journal of Applied Mathematics*, 36:85–99, 1986.

C.F. Popelar and K.M. Liechti. Multiaxial nonlinear viscoelastic characterization and modeling of a strucutural adhesive. *Journal of Materials and Technology*, 119:205–210, 1997.

C.F. Popelar and K.M. Liechti. A distortion-modified free volume theory for nonlinear viscoelastic behavior. *Mechanics of Time-Depdendent Materials*, 7:89–141, 2003.

J.L. Rand. An improved constitutive equation for sf420 part i: the master curve. Report by Winzen Engineering Inc., 2008a.

J.L. Rand. An improved constitutive equation for sf420 part ii: the biaxial behavior. Report by Winzen Engineering Inc., 2008b.

J.L. Rand and W.J. Sterling. A constitutive equation for stratospheric balloon materials. *Advances in Space Research*, 37:2087–2091, 2006.

J.L. Rand and D. Wakefield. Studies of thin film nonlinear viscoelasticity for superpressure balloons. *Advances in Space Research*, 45:56–60, 2010.

W.T. Read. Stress analysis for compressible viscoelastic materials. *Journal of Applied Physics*, 21:671–674, 1950.

E. Reissner. On tension field theory. *Fifth International Congress on Applied Mechanics*, pages 88–92, 1938.

F.P.J. Rimrott. Storable tubular extensible member: a unique machine element. *Machine Design*, 37:156–163, 1965.

D.G. Roddeman, J. Drucker, C.W.J. Oomens, and J.D. Janssen. The wrinkling of thin membranes: Part i - theory. *Journal of Applied Mechanics*, 54:884–887, 1987.

S.B. Sane and W.G. Knauss. On interconversion of various material functions of pmma. *Mechanics of Time-Dependent Materials*, 5:325–343, 2001.

R.A. Schapery. An engineering theory of nonlinear viscoelasticity with applications. *International Journal of Solids and Structures*, 2:407–425, 1966.

R.A. Schapery. On the characterization of nonlinear viscoelastic materials. *Polymer Engineering and Science*, 9:295–310, 1969.

R.A. Schapery. Nonlinear viscoelastic and viscoplastic constitutive equations based on thermodynamics. *Mechanics of Time-Dependent Materials*, 1:209–240, 1997.

K.A. Seffen and S. Pellegrino. Deployment dynamics of tape springs. *Proceedings of the Royal Society of London, Seris A: Mathematical and Physical Sciences*, 455:1003–1048, 1999.

P. Seizt. Spar resolving spat over antenna work. *Space News*, September 4, 1994.

P. Shrotriya and N.R. Sottos. Viscoelastic response of woven composite substrates. *Composite Science and Technology*, 65:621–634, 2005.

I.S. Smith. The nasa balloon program: Looking to the future. *Advances in Space Research*, 33: 1588–1593, 2004.

M.S. Smith and E.L. Rainwater. Optimum designs for superpressure balloons. *Advances in Space Research*, 33:1688–1693, 2004.

O. Soykasap. Deployment analysis of a self-deployable composite boom. *Composite Structures*, 89: 374–381, 2009.

O. Soykasap, S. Pellegrino, P. Howard, and M. Notter. Folding large antenna tape spring. *Journal of Spacecrafts and Rockets*, 45:560–567, 2008.

M. Stein and J.M. Hedgepeth. Analysis of partly wrinkled membranes. *NASA Technical Note*, D-813, 1961.

R.L. Taylor, K.S. Pister, and G.L. Goudreau. Thermomechanical analysis of viscoelastic solids. *International Journal for Numerical Methods in Engineering*, 2:45–59, 1970.

N.W. Tschoegl. *The Phenomenological Theory of Linear Viscoelastic Behavior*. Springer-Verlag, Heidelberg, 1989.

N.W. Tschoegl, W.G. Knauss, and I. Emri. Poisson's ratio in linear viscoelasticity - a critical review. *Mechanics of Time-Dependent Materials*, 6:3–51, 2002.

H.S. Tsien. A generalization of alfrey's theorem for viscoelastic media. *Quarterly of Applied Mathematics*, 8:104, 1950.

M.L. Williams, R.F. Landel, and J.D. Ferry. The temperature dependence of relaxation mechanisms of amorphous polymers and other glass-forming liquids. *Journal of the American Chemical Society*, 77:3701–3707, 1955.

Z. Xia, X. Shen, and F. Ellyin. An assessment of nonlinearly viscoelastic constitutive models for cyclic loading: The effect of a general loading/unloading rule. *Mechanics of Time-Dependent Materials*, 9:281–300, 2006.

J.C.H. Yee and S. Pellegrino. Composite tube hinges. *Journal of Aerospace Engineering*, 18:224–231, 2005.

L. Young. Gsfc cte curve fitting data. Report by Goddard Space Flight Center, 2010.

C.T. Zhang and I.D. Moore. Nonlinear mechanical response of high density polyethylene. part ii: Uniaxial constitutive modeling. *Polymer Engineering and Science*, 37:414–420, 1997.

Q. Zhu, P. Shrotriya, P.H. Geubelle, and N.R. Sottos. Viscoelastic response of a woven composite substrate for multilayer circuit board applications. *Composite Science and Technology*, 46:394–402, 2003.

Appendix A

Abaqus User-defined Subroutines

A.1 UMAT for Viscoelastic Tows

```
*USER SUBROUTINES
C***********************************************************************
C2345678901234567890123456789012345678901234567890123456789012345678901 2
      SUBROUTINE UMAT(STRESS,STATEV,DDSDDE,SSE,SPD,SCD,
     1 RPL,DDSDDT,DRPLDE,DRPLDT,
     2 STRAN,DSTRAN,TIME,DTIME,TEMP,DTEMP,PREDEF,DPRED,CMNAME,
     3 NDI,NSHR,NTENS,NSTATV,PROPS,NPROPS,COORDS,DROT,PNEWDT,
     4 CELENT,DFGRD0,DFGRD1,NOEL,NPT,LAYER,KSPT,KSTEP,KINC)

 INCLUDE 'ABA_PARAM.INC'

   CHARACTER*80 CMNAME
   DIMENSION STRESS(NTENS),STATEV(NSTATV),
  1 DDSDDE(NTENS,NTENS),DDSDDT(NTENS),DRPLDE(NTENS),
  2 STRAN(NTENS),DSTRAN(NTENS),TIME(2),PREDEF(1),DPRED(1),
  3 PROPS(NPROPS),COORDS(3),DROT(3,3),DFGRD0(3,3),DFGRD1(3,3)

   INTEGER NProny, counter
   REAL*8 rhoi(7)
   REAL*8 C11inf, C12inf, C22inf, C23inf, C44inf, C55inf
   REAL*8 C11i(7), C12i(7), C22i(7), C23i(7), C44i(7), C55i(7)
   REAL*8 qold(NTENS, 7), q(NTENS, 7)
   REAL*8 f111, f122, f123, f121, f222, f233, f232, f223
   REAL*8 f444, f555, f556
```

```
      REAL*8 depsilon(NTENS), epsilonE(NTENS), sigmaE(NTENS)


C----------PROPS DESIGNATION----------C
C
C     PROPS  1 - 7 : rhoi   %relaxation times
C     PROPS  8      : C11inf
C     PROPS  9 - 15 : C11i
C     PROPS 16      : C12inf
C     PROPS 17 - 23 : C12i
C     PROPS 24      : C22inf
C   PROPS 25 - 31 : C22i
C     PROPS 32      : C23inf
C     PROPS 33 - 39 : C23i
C     PROPS 40      : C44inf
C     PROPS 41 - 47 : C44i
C     PROPS 48      : C55inf
C     PROPS 49 - 55 : C55i


C----------STATEV DESIGNATION----------C
C
C     STATEV  1 - 42 : qold   %old hereditary integrals


C-----linear viscoelastic parameters--------C


C    Number of Prony terms
     NProny=7


C    Obtain Prony coefficients
     do i=1,NProny
       rhoi(i)=PROPS(i)
       C11i(i)=PROPS(8+i)
       C12i(i)=PROPS(16+i)
       C22i(i)=PROPS(24+i)
       C23i(i)=PROPS(32+i)
       C44i(i)=PROPS(40+i)
       C55i(i)=PROPS(48+i)
```

```
      end do


C Obtain long term modulus
C11inf=PROPS(8)
C12inf=PROPS(16)
C22inf=PROPS(24)
C23inf=PROPS(32)
C44inf=PROPS(40)
C55inf=PROPS(48)


C----------solution-dependent variables----------C


C     old heredity integrals
      counter = 1
  do j = 1,NTENS
       do i = 1,NProny
    qold(j,i) = STATEV(counter)
    counter = counter+1
  end do
      end do


C----------update stress-------------C


C     switch to Voight notation
      depsilon(1)=DSTRAN(1)
      depsilon(2)=DSTRAN(2)
      depsilon(3)=DSTRAN(3)
      depsilon(4)=DSTRAN(6)
      depsilon(5)=DSTRAN(5)
      depsilon(6)=DSTRAN(4)
      epsilonE(1)=STRAN(1) + DSTRAN(1)
      epsilonE(2)=STRAN(2) + DSTRAN(2)
      epsilonE(3)=STRAN(3) + DSTRAN(3)
      epsilonE(4)=STRAN(6) + DSTRAN(6)
      epsilonE(5)=STRAN(5) + DSTRAN(5)
      epsilonE(6)=STRAN(4) + DSTRAN(4)
```

```
C     compute q
      do j = 1,NTENS
        do i = 1, NProny
          q(j,i)=EXP(-DTIME/rhoi(i))*qold(j,i)+
     1 depsilon(j)*(1-EXP(-DTIME/rhoi(i)))/(DTIME/rhoi(i))
        end do
      end do


C     compute f
    f111=0
      f122=0
      f123=0
      f121=0
      f222=0
      f233=0
      f232=0
      f223=0
      f444=0
      f555=0
      f556=0
      do i = 1, NProny
        f111=f111+C11i(i)*q(1,i)
        f122=f122+C12i(i)*q(2,i)
        f123=f123+C12i(i)*q(3,i)
        f121=f121+C12i(i)*q(1,i)
        f222=f222+C22i(i)*q(2,i)
        f233=f233+C23i(i)*q(3,i)
        f232=f232+C23i(i)*q(2,i)
        f223=f223+C22i(i)*q(3,i)
        f444=f444+C44i(i)*q(4,i)
        f555=f555+C55i(i)*q(5,i)
        f556=f556+C55i(i)*q(6,i)
      end do

      sigmaE(1) = C11inf*epsilonE(1)+f111+C12inf*epsilonE(2)+f122+
```

```
   1 C12inf*epsilonE(3)+f123
    sigmaE(2) = C12inf*epsilonE(1)+f121+C22inf*epsilonE(2)+f222+
   1 C23inf*epsilonE(3)+f233
    sigmaE(3) = C12inf*epsilonE(1)+f121+C23inf*epsilonE(2)+f232+
   1 C22inf*epsilonE(3)+f223
    sigmaE(4) = C44inf*epsilonE(4) + f444
    sigmaE(5) = C55inf*epsilonE(5) + f555
    sigmaE(6) = C55inf*epsilonE(6) + f556


    STRESS(1) = sigmaE(1)
    STRESS(2) = sigmaE(2)
    STRESS(3) = sigmaE(3)
    STRESS(4) = sigmaE(6)
    STRESS(5) = sigmaE(5)
    STRESS(6) = sigmaE(4)


C-----update solution-dependent variables-----C


C     hereditary integrals
      counter = 1
      do j = 1,NTENS
        do i = 1, NProny
          STATEV(counter)=q(j,i)
          counter=counter+1
        end do
      end do


C-----update Jacobian (tangent stiffess)-----C


      do i = 1, NTENS
        do j = 1, NTENS
          DDSDDE(i,j)=0.0
        end do
      end do


      do i = 1, NProny
```

```
      DDSDDE(1,1)=DDSDDE(1,1)+C11inf+
    1 C11i(i)*(1-EXP(-DTIME/rhoi(i)))/(DTIME/rhoi(i))
      DDSDDE(1,2)=DDSDDE(1,2)+C12inf+
    1 C12i(i)*(1-EXP(-DTIME/rhoi(i)))/(DTIME/rhoi(i))
      DDSDDE(2,2)=DDSDDE(2,2)+C22inf+
    1 C22i(i)*(1-EXP(-DTIME/rhoi(i)))/(DTIME/rhoi(i))
      DDSDDE(2,3)=DDSDDE(2,3)+C23inf+
    1 C23i(i)*(1-EXP(-DTIME/rhoi(i)))/(DTIME/rhoi(i))
      DDSDDE(5,5)=DDSDDE(5,5)+C55inf+
    1 C55i(i)*(1-EXP(-DTIME/rhoi(i)))/(DTIME/rhoi(i))
      DDSDDE(6,6)=DDSDDE(6,6)+C44inf+
    1 C44i(i)*(1-EXP(-DTIME/rhoi(i)))/(DTIME/rhoi(i))
      end do


      DDSDDE(1,3)=DDSDDE(1,2)
      DDSDDE(2,1)=DDSDDE(1,2)
      DDSDDE(3,1)=DDSDDE(1,3)
      DDSDDE(3,2)=DDSDDE(2,3)
      DDSDDE(3,3)=DDSDDE(2,2)
      DDSDDE(4,4)=DDSDDE(5,5)


C----------update energy----------C


C     update elastic strain energy in SSE
      SSE = 0.0


C     update creep dissipation in SCD
      SCD = 0.0


C     update plastic dissipation in SPD
    SPD = 0.0


      RETURN
      END
C**********************************************************************
C**********************************************************************
```

```
C23456789012345678901234567890123456789012345678901234567890123456789012
      SUBROUTINE SDVINI(STATEV,COORDS,NSTATV,NCRDS,NOEL,NPT,
     1 LAYER,KSPT)


      INCLUDE 'ABA_PARAM.INC'


      DIMENSION STATEV(NSTATV),COORDS(NCRDS)


C     Initialize state variables
      do i = 1,NSTATV
        STATEV(i) = 0.0
      end do


      RETURN
      END
```

A.2   UGENS for Viscoelastic Laminas

```
*USER SUBROUTINES
C************************************************************************
C23456789012345678901234567890123456789012345678901234567890123456789012
      SUBROUTINE UGENS(DDNDDE,FORCE,STATEV,SSE,SPD,PNEWDT,STRAN,
     1 DSTRAN,TSS,TIME,DTIME,TEMP,DTEMP,PREDEF,DPRED,CENAME,NDI,
     2 NSHR,NSECV,NSTATV,PROPS,JPROPS,NPROPS,NJPROP,COORDS,CELENT,
     3 THICK,DFGRD,CURV,BASIS,NOEL,NPT,KSTEP,KINC,NIT,LINPER)


      INCLUDE 'ABA_PARAM.INC'


      CHARACTER*80 CMNAME
      DIMENSION DDNDDE(NSECV,NSECV),FORCE(NSECV),STATEV(NSTATV),
     1 STRAN(NSECV),DSTRAN(NSECV),TSS(2),TIME(2),PREDEF(*),
     2 DPRED(*),PROPS(*),JPROPS(*),COORDS(3),DFGRD(3,3),
     3 CURV(2,2),BASIS(3,3)


      INTEGER nProny, counter
      REAL*8 rhoi(7)
```

```fortran
      REAL*8 A11inf, A12inf, A33inf, D11inf, D12inf, D33inf
      REAL*8 A11i(7), A12i(7), A33i(7), D11i(7), D12i(7), D33i(7)
      REAL*8 qold(NSECV, 7), q(NSECV, 7)
      REAL*8 a111, a122, a121, a112, a333
      REAL*8 d114, d125, d124, d115, d336
      REAL*8 strainE(NSECV)
      REAL*8 c1, c2, Tr, aT


C----------PROPS DESIGNATION----------C
C
C     PROPS  1 - 7  : rhoi   %relaxation times
C     PROPS  8      : A11inf
C     PROPS  9 - 15 : A11i
C     PROPS 16      : A12inf
C     PROPS 17 - 23 : A12i
C     PROPS 24      : A33inf
C   PROPS 25 - 31 : A33i
C     PROPS 32      : D11inf
C     PROPS 33 - 39 : D11i
C     PROPS 40      : D12inf
C     PROPS 41 - 47 : D12i
C     PROPS 48      : D33inf
C     PROPS 49 - 55 : D33i


C----------STATEV DESIGNATION----------C
C
C     STATEV  1 - 42 : qold   %old hereditary integrals


C-----material parameters---------C


C Number of Prony terms
      nProny=7


C     Obtain Prony coefficients
      do i=1,nProny
        rhoi(i)=PROPS(i)
```

```fortran
      A11i(i)=PROPS(8+i)

      A12i(i)=PROPS(16+i)

      A33i(i)=PROPS(24+i)

      D11i(i)=PROPS(32+i)

      D12i(i)=PROPS(40+i)

      D33i(i)=PROPS(48+i)

    end do


C Obtain long term modulus
A11inf=PROPS(8)

A12inf=PROPS(16)

A33inf=PROPS(24)

D11inf=PROPS(32)

D12inf=PROPS(40)

D33inf=PROPS(48)


C WLF parameters
      Tr=313.0

      c1=28.3816

   c2=93.291


C----------solution-dependent variables----------C


C     old heredity integrals
      counter = 1

do j = 1,NSECV

       do i = 1,nProny

   qold(j,i) = STATEV(counter)

   counter = counter+1

  end do

      end do


C----------update stress-------------C


C     generalized section strains at the end of increment
      strainE(1)=STRAN(1) + DSTRAN(1)
```

```fortran
      strainE(2)=STRAN(2) + DSTRAN(2)

      strainE(3)=STRAN(3) + DSTRAN(3)

      strainE(4)=STRAN(4) + DSTRAN(4)

      strainE(5)=STRAN(5) + DSTRAN(5)

      strainE(6)=STRAN(6) + DSTRAN(6)


C shift factor
      aT=10**(-c1*(TEMP-Tr)/(c2+TEMP-Tr))


C     reduced time increment
dtr=DTIME/aT


C     compute q
      do j = 1,NSECV
        do i = 1, nProny
          q(j,i)=exp(-dtr/rhoi(i))*qold(j,i)+
     & DSTRAN(j)*(1-exp(-dtr/rhoi(i)))/(dtr/rhoi(i))
        end do
      end do


C     compute a and d
  a111=0
      a122=0
      a121=0
      a112=0
      a333=0
      d114=0
      d125=0
      d124=0
      d115=0
      d336=0
      do i = 1, nProny
        a111=a111+A11i(i)*q(1,i)
        a122=a122+A12i(i)*q(2,i)
        a121=a121+A12i(i)*q(1,i)
        a112=a112+A11i(i)*q(2,i)
```

```
          a333=a333+A33i(i)*q(3,i)

          d114=d114+D11i(i)*q(4,i)

          d125=d125+D12i(i)*q(5,i)

          d124=d124+D12i(i)*q(4,i)

          d115=d115+D11i(i)*q(5,i)

          d336=d336+D33i(i)*q(6,i)

        end do


        FORCE(1) = A11inf*strainE(1)+a111+A12inf*strainE(2)+a122

        FORCE(2) = A12inf*strainE(1)+a121+A11inf*strainE(2)+a112

        FORCE(3) = A33inf*strainE(3)+a333

        FORCE(4) = D11inf*strainE(4)+d114+D12inf*strainE(5)+d125

        FORCE(5) = D12inf*strainE(4)+d124+D11inf*strainE(5)+d115

        FORCE(6) = D33inf*strainE(6)+d336


C-----update solution-dependent variables-----C


C     hereditary integrals
        counter = 1
        do j = 1,NSECV
          do i = 1, nProny
            STATEV(counter)=q(j,i)
            counter=counter+1
          end do
        end do


C-----update Jacobian (tangent stiffess)-----C


        do i = 1, NSECV
          do j = 1, NSECV
            DDNDDE(i,j)=0.0
          end do
        end do


        do i = 1, nProny
          DDNDDE(1,1)=DDNDDE(1,1)+A11inf+
```

```
   & A11i(i)*(1-exp(-dtr/rhoi(i)))/(dtr/rhoi(i))
      DDNDDE(1,2)=DDNDDE(1,2)+A12inf+
   & A12i(i)*(1-exp(-dtr/rhoi(i)))/(dtr/rhoi(i))
      DDNDDE(3,3)=DDNDDE(3,3)+A33inf+
   & A33i(i)*(1-exp(-dtr/rhoi(i)))/(dtr/rhoi(i))
      DDNDDE(4,4)=DDNDDE(4,4)+D11inf+
   & D11i(i)*(1-exp(-dtr/rhoi(i)))/(dtr/rhoi(i))
      DDNDDE(4,5)=DDNDDE(4,5)+D12inf+
   & D12i(i)*(1-exp(-dtr/rhoi(i)))/(dtr/rhoi(i))
      DDNDDE(6,6)=DDNDDE(6,6)+D33inf+
   & D33i(i)*(1-exp(-dtr/rhoi(i)))/(dtr/rhoi(i))
    end do


    DDNDDE(2,1)=DDNDDE(1,2)
    DDNDDE(2,2)=DDNDDE(1,1)
    DDNDDE(5,4)=DDNDDE(4,5)
    DDNDDE(5,5)=DDNDDE(4,4)


C----------update energy----------C


C     update elastic strain energy in SSE
      SSE = 0.0


C     update plastic dissipation in SPD
SPD = 0.0


      RETURN
      END
C**********************************************************************
C**********************************************************************
C23456789012345678901234567890123456789012345678901234567890123456789012
      SUBROUTINE SDVINI(STATEV,COORDS,NSTATV,NCRDS,NOEL,NPT,
     1 LAYER,KSPT)


      INCLUDE 'ABA_PARAM.INC'
```

```
      DIMENSION STATEV(NSTATV),COORDS(NCRDS)


C     Initialize state variables
      do i = 1,NSTATV
        STATEV(i) = 0.0
      end do


      RETURN
      END
```

A.3 VUMAT for StratoFilm 420

```
*USER SUBROUTINES
C**********************************************************************
C2345678901234567890123456789012345678901234567890123456789012345678901234567890123456789012
      subroutine vumat(
     1 nblock, ndir, nshr, nstatev, nfieldv, nprops, lanneal,
     2 stepTime, totalTime, dt, cmname, coordMp, charLength,
     3 props, density, strainInc, relSpinInc,
     4 tempOld, stretchOld, defgradOld, fieldOld,
     5 stressOld, stateOld, enerInternOld, enerInelasOld,
     6 tempNew, stretchNew, defgradNew, fieldNew,
     7 stressNew, stateNew, enerInternNew, enerInelasNew )


      include 'vaba_param.inc'


      dimension props(nprops), density(nblock), coordMp(nblock,*),
     1 charLength(nblock), strainInc(nblock,ndir+nshr),
     2 relSpinInc(nblock,nshr), tempOld(nblock),
     3 stretchOld(nblock,ndir+nshr),
     4 defgradOld(nblock,ndir+nshr+nshr),
     5 fieldOld(nblock,nfieldv), stressOld(nblock,ndir+nshr),
     6 stateOld(nblock,nstatev), enerInternOld(nblock),
     7 enerInelasOld(nblock), tempNew(nblock),
     8 stretchNew(nblock,ndir+nshr),
```

```
8  defgradNew(nblock,ndir+nshr+nshr),
9  fieldNew(nblock,nfieldv),
1  stressNew(nblock,ndir+nshr), stateNew(nblock,nstatev),
2  enerInternNew(nblock), enerInelasNew(nblock)

   character*80 cmname

   integer nProny, counter, state
   real*8 tauj(15)
   real*8 S110, S120, S130, S220, S230, S660
   real*8 S11j(15),S12j(15),S13j(15),S22j(15),S23j(15),S66j(15)

   real*8 CTEMD, CTETD, CTEV
   real*8 c1, c2, Tr
   real*8 fr, B

   real*8 PK2pold(3)
   real*8 q11old(15),q12old(15),q13old(15)
   real*8 q21old(15),q22old(15),q23old(15)
   real*8 q66old(15)
   real*8 thetaold, thetaolder, thetashift

   real*8 aTtheta, dtr
   real*8 S11, S12, S13, S22, S23, S66
   real*8 f11, f12, f13, f21, f22, f23, f66
   real*8 U(3,3), UT(3,3), U2(3,3), I(3,3), E(3,3), PK2(3,3), detS

   real*8 Ep(3), PK2p(3), PK2ppr(3), Eppr(3)

   real*8 Sp(3,3), fp(3)
   integer nalpha, nloop, nbeta, ngamma
   real*8 alpha(19), beta(19), gamma(19), angle_w
   real*8 T(3,3), Tinv(3,3)
   real*8 Ep_rot(3), Sp_rot(3,3), fp_rot(3), Ep_u(3)
   real*8 Ep1_a(19), deltaEp2_a(19), deltaEp3_a(19)
   real*8 Ep1_b(19), deltaEp2_b(19)
```

```fortran
      real*8 angle_l, angle_r, f_l, f_r, angle_new, f_new
      real*8 Ep_w(3), Sp_w(3,3), fp_w(3), PK2p_w(3)
      real*8 Ep_c(3), PK2p_c(3)


      real*8 Uppr(2), theta, detU, detUp


      real*8 temp1(3,3), temp2(3,3), sigma(3,3)


      real*8,PARAMETER:: pi=3.14159265358979323846d0
      real*8,PARAMETER:: tol=1.0d-12


C----------PROPS DESIGNATION----------C
C
C     PROPS  1 - 13 : CTEMD %Coefficient of Thermal Expansion MD
C     PROPS 14 - 26 : CTETD %Coefficient of Thermal Expansion TD
C     PROPS 27 - 32 : WLF   %William-Landel-Ferry Constants
C     PROPS 33 - 47 : tauj  %Retardation Times
C     PROPS 48      : D0    %Prony Coefficients MD
C     PROPS 49 - 63 : Dj    %Prony Coefficients MD
C   PROPS 64   : S130  %Prony Coefficients MD & ThD
C     PROPS 65 - 79 : S13j  %Prony Coefficients MD & ThD
C     PROPS 80      : S230  %Prony Coefficients TD & ThD
C     PROPS 81 - 95 : S23j  %Prony Coefficients TD & ThD
C
C----------STATEV DESIGNATION----------C
C
C     statev   1 -   3 : PK2old %PK2 stresses at the beginning of increment
C     statev   4 - 108 : qold %hereditary integrals at the beginning of increment
C     statev 109 - 112 : E %Green strain at the beginning of increment
C     statev 113 : thetaold  %volumetric strain at the beginning of increment
C     statev 114 : thetaolder %volumetric strain at the beginning of previous increment
C     statev 115 : thetashift %volumetric strain used for shift factor
C     statev 116 : aTthetaold %shift factor at the beginning of increment
C
C----------material parameters---------C
```

```fortran
C Number of Prony terms
      nProny=15


C     Obtain compliance Prony coefficients
      do j=1,NProny
        tauj(j)=PROPS(32+j)
S11j(j)=PROPS(48+j)
S12j(j)=-0.4*PROPS(48+j)
        S13j(j)=PROPS(64+j)
        S22j(j)=(1.122+(6.5895D-4)*T-(6.609D-6)*T**2)*PROPS(48+j)
S23j(j)=PROPS(80+j)
S66j(j)=2.45*PROPS(48+j)
      end do


C Obtain instantaneous compliance
S110=PROPS(48)
S120=-0.4*PROPS(48)
S130=PROPS(64)
S220=(1.122+(6.5895E-4)*T-(6.609E-6)*T**2)*PROPS(48)
S230=PROPS(80)
      S660=2.45*PROPS(48)


C----------zeroth increment---------C


      if (stepTime==0) then


      do km = 1,nblock


      detS=S110*S220-S120*S120
      stressNew(km,1)=stressOld(km,1)
     & +(S220*strainInc(km,1)-S120*strainInc(km,2))/detS
      stressNew(km,2)=stressOld(km,2)
     & +(-S120*strainInc(km,1)+S110*strainInc(km,2))/detS
      stressNew(km,3)=0.0d0
stressNew(km,4)=stressOld(km,4)+strainInc(km,4)/S660
```

```
      end do


      end if


C----------actual increments---------C


      if (stepTime/=0.0d0) then


      do km = 1,nblock


C----------free volume parameters---------C


C Calculate CTE
       CTEMD=props(1)*tempOld(km)**12+props(2)*tempOld(km)**11
     & +props(3)*tempOld(km)**10+props(4)*tempOld(km)**9
     & +props(5)*tempOld(km)**8+props(6)*tempOld(km)**7
     & +props(7)*tempOld(km)**6+props(8)*tempOld(km)**5
     & +props(9)*tempOld(km)**4+props(10)*tempOld(km)**3
     & +props(11)*tempOld(km)**2+props(12)*tempOld(km)+props(13)
CTETD=props(14)*tempOld(km)**12+props(15)*tempOld(km)**11
     & +props(16)*tempOld(km)**10+props(17)*tempOld(km)**9
     & +props(18)*tempOld(km)**8+props(19)*tempOld(km)**7
     & +props(20)*tempOld(km)**6+props(21)*tempOld(km)**5
     & +props(22)*tempOld(km)**4+props(23)*tempOld(km)**3
     & +props(24)*tempOld(km)**2+props(25)*tempOld(km)+props(26)
       CTEV=CTEMD+CTETD+(CTEMD+CTETD)/2.0d0


C     WLF constants
if (tempOld(km)>233.16d0) then
        c1=props(27)
        c2=props(28)
        Tr=props(29)
      else
        c1=props(30)
        c2=props(31)
        Tr=props(32)
```

```
      end if


C free volume at reference temperature Tr
fr=c2*CTEV


C Doolittle equation parameter
B=2.303d0*fr*c1


C----------solution-dependent variables----------C


C     PK2 stresses at the beginning of increment
      do j=1,3
PK2pold(j) = stateOld(km,j)
end do


C     heredity integrals at the beginning of increment
counter = 4 ! first position of qold in stateOld
do j = 1,nProny
        q11old(j) = stateOld(km,counter)
        q12old(j) = stateOld(km,counter+nProny)
        q13old(j) = stateOld(km,counter+2*nProny)
        q21old(j) = stateOld(km,counter+3*nProny)
        q22old(j) = stateOld(km,counter+4*nProny)
        q23old(j) = stateOld(km,counter+5*nProny)
        q66old(j) = stateOld(km,counter+6*nProny)
  counter = counter+1
end do


C     volumetric strain at the beginning of increment
      thetaold=stateOld(km,113)


C     volumetric strain at the beginning of previous increment
      thetaolder=stateOld(km,114)


C     volumetric strain used for shift
      thetashift=stateOld(km,115)
```

```
C----------determine element state-------------C


C     change volumetric strain for loading/unloading switch
      if (thetaold>=thetaolder) thetashift=thetaold


C shift factor
      aTtheta=10.0d0**((-B/(2.303d0*fr))
     & *(CTEV*(tempOld(km)-Tr)+thetashift)
     & /(fr+CTEV*(tempOld(km)-Tr)+thetashift))


C     reduced time increment
dtr=dt/aTtheta


C     compute S
      S11 = S110
      S12 = S120
      S13 = S130
      S22 = S220
      S23 = S230
      S66 = S660
      do j = 1, nProny
        S11=S11+S11j(j)-S11j(j)*(1.0d0-dexp(-dtr/tauj(j)))/
     & (dtr/tauj(j))
        S12=S12+S12j(j)-S12j(j)*(1.0d0-dexp(-dtr/tauj(j)))/
     & (dtr/tauj(j))
        S13=S13+S13j(j)-S13j(j)*(1.0d0-dexp(-dtr/tauj(j)))/
     & (dtr/tauj(j))
        S22=S22+S22j(j)-S22j(j)*(1.0d0-dexp(-dtr/tauj(j)))/
     & (dtr/tauj(j))
        S23=S23+S23j(j)-S23j(j)*(1.0d0-dexp(-dtr/tauj(j)))/
     & (dtr/tauj(j))
        S66=S66+S66j(j)-S66j(j)*(1.0d0-dexp(-dtr/tauj(j)))/
     & (dtr/tauj(j))
       end do
```

```
C       compute f
f11=0.0d0
        f12=0.0d0
        f13=0.0d0
        f21=0.0d0
        f22=0.0d0
        f23=0.0d0
        f66=0.0d0
        do j = 1, nProny
           f11=f11+S11j(j)*(dexp(-dtr/tauj(j))*q11old(j)-
     & (1.0d0-dexp(-dtr/tauj(j)))*PK2pold(1)/(dtr/tauj(j)))
           f12=f12+S12j(j)*(dexp(-dtr/tauj(j))*q12old(j)-
     & (1.0d0-dexp(-dtr/tauj(j)))*PK2pold(1)/(dtr/tauj(j)))
           f13=f13+S13j(j)*(dexp(-dtr/tauj(j))*q13old(j)-
     & (1.0d0-dexp(-dtr/tauj(j)))*PK2pold(1)/(dtr/tauj(j)))
           f21=f21+S12j(j)*(dexp(-dtr/tauj(j))*q21old(j)-
     & (1.0d0-dexp(-dtr/tauj(j)))*PK2pold(2)/(dtr/tauj(j)))
           f22=f22+S22j(j)*(dexp(-dtr/tauj(j))*q22old(j)-
     & (1.0d0-dexp(-dtr/tauj(j)))*PK2pold(2)/(dtr/tauj(j)))
           f23=f23+S23j(j)*(dexp(-dtr/tauj(j))*q23old(j)-
     & (1.0d0-dexp(-dtr/tauj(j)))*PK2pold(2)/(dtr/tauj(j)))
           f66=f66+S66j(j)*(dexp(-dtr/tauj(j))*q66old(j)-
     & (1.0d0-dexp(-dtr/tauj(j)))*PK2pold(3)/(dtr/tauj(j)))
        end do


C    Green strains at the end of increment
        do m=1,3
          do n=1,3
            U(m,n)=0.0d0
            I(m,n)=0.0d0
          end do
        end do
        U(1,1)=stretchNew(km,1)
        U(2,2)=stretchNew(km,2)
        U(3,3)=stretchNew(km,3)
        U(1,2)=stretchNew(km,4)
```

```
      U(2,1)=stretchNew(km,4)
      I(1,1)=1.0d0
      I(2,2)=1.0d0
      I(3,3)=1.0d0
      UT=transpose(U)
      U2=matmul(UT,U)
      E=(U2-I)/2.0d0


C     PK2 stresses at the end of increment
      detS=S11*S22-S12*S12
      PK2(1,1)=(S22*(E(1,1)+f11+f21)
     & -S12*(E(2,2)+f12+f22))/detS
      PK2(2,2)=(-S12*(E(1,1)+f11+f21)
     & +S11*(E(2,2)+f12+f22))/detS
      PK2(3,3)=0.0d0
      PK2(1,2)=(E(1,2)+f66)/S66
PK2(1,3)=0.0d0
PK2(2,1)=(E(1,2)+f66)/S66
PK2(2,3)=0.0d0
PK2(3,1)=0.0d0
PK2(3,2)=0.0d0


C     principal Green strains at the end of increment
      Ep(1)=E(1,1)
      Ep(2)=E(2,2)
      Ep(3)=E(1,2)
      Eppr(1)=(Ep(1)+Ep(2))/2.0d0
     & +dsqrt(((Ep(1)-Ep(2))/2.0d0)**2.0d0+Ep(3)**2.0d0)
      Eppr(2)=(Ep(1)+Ep(2))/2.0d0
     & -dsqrt(((Ep(1)-Ep(2))/2.0d0)**2.0d0+Ep(3)**2.0d0)


C     principal PK2 stresses at the end of increment
      PK2p(1)=PK2(1,1)
      PK2p(2)=PK2(2,2)
      PK2p(3)=PK2(1,2)
      PK2ppr(1)=(PK2p(1)+PK2p(2))/2.0d0
```

```
     & +dsqrt(((PK2p(1)-PK2p(2))/2.0d0)**2.0d0+PK2p(3)**2.0d0)
      PK2ppr(2)=(PK2p(1)+PK2p(2))/2.0d0
     & -dsqrt(((PK2p(1)-PK2p(2))/2.0d0)**2.0d0+PK2p(3)**2.0d0)


C     element state (1:slack, 2:wrinkled, 3: taut)
      state=0
      if (Eppr(1)<=0.0d0) then
        state=1
      else if (PK2ppr(2)<0.0d0) then
          state=2
      else
          state=3
      endif


C----------slack element-------------C

      if (state==1) then


C        write(1,'(a)'), 'slack'


C        PK2 stresses
          PK2(1,1)=0.0d0
          PK2(2,2)=0.0d0
          PK2(3,3)=0.0d0
    PK2(1,2)=0.0d0
    PK2(1,3)=0.0d0
          PK2(2,1)=0.0d0
          PK2(2,3)=0.0d0
    PK2(3,1)=0.0d0
    PK2(3,2)=0.0d0


C        Green strains
          E(1,1)=S11*PK2(1,1)-f11+S12*PK2(2,2)-f21
          E(2,2)=S12*PK2(1,1)-f12+S22*PK2(2,2)-f22
          E(3,3)=S13*PK2(1,1)-f13+S23*PK2(2,2)-f23
          E(1,2)=S66*PK2(1,2)-f66
```

```
      E(1,3)=0.0d0
      E(2,1)=S66*PK2(1,2)-f66
      E(2,3)=0.0d0
      E(3,1)=0.0d0
      E(3,2)=0.0d0


C     right stretch tensor
      Ep(1)=E(1,1)
      Ep(2)=E(2,2)
      Ep(3)=E(1,2)
      Eppr(1)=(Ep(1)+Ep(2))/2.0d0
   & +dsqrt(((Ep(1)-Ep(2))/2.0d0)**2.0d0+Ep(3)**2.0d0)
      Eppr(2)=(Ep(1)+Ep(2))/2.0d0
   & -dsqrt(((Ep(1)-Ep(2))/2.0d0)**2.0d0+Ep(3)**2.0d0)
      Uppr(1)=dsqrt(Eppr(1)*2.0d0+1.0d0)
      Uppr(2)=dsqrt(Eppr(2)*2.0d0+1.0d0)
      detUp=Uppr(1)*Uppr(2)

      if (E(1,2)>=0.0d0) then
        U(1,2)=dsqrt(2.0d0*E(1,2)**2.0d0/(E(1,1)+E(2,2)+1.0d0+detUp))
      endif
      if (E(1,2)<0.0d0) then
        U(1,2)=-dsqrt(2.0d0*E(1,2)**2.0d0/(E(1,1)+E(2,2)+1.0d0+detUp))
      endif
      U(1,1)=dsqrt(2.0d0*E(1,1)+1.0d0-U(1,2)**2.0d0)
      U(2,2)=dsqrt(2.0d0*E(2,2)+1.0d0-U(1,2)**2.0d0)
      U(3,3)=dsqrt(E(3,3)*2.0d0+1.0d0)
      U(1,3)=0.0d0
      U(2,1)=U(1,2)
      U(2,3)=0.0d0
      U(3,1)=0.0d0
      U(3,2)=0.0d0
      UT=transpose(U)
      detU=detUp*U(3,3)


C     material volumetric strain
```

```
      theta=detU-1


      endif


C----------wrinkled element-------------C


      if (state==2) then

C        write(1,'(a)'), 'wrinkled'


C        S in material directions
         Sp(1,1)=S11
         Sp(1,2)=S12
         Sp(1,3)=0.0d0
         Sp(2,1)=S12
         Sp(2,2)=S22
         Sp(2,3)=0.0d0
         Sp(3,1)=0.0d0
         Sp(3,2)=0.0d0
         Sp(3,3)=S66


C        f in material directions
         fp(1)=f11+f21
         fp(2)=f12+f22
         fp(3)=f66


C        compute strains at initial sampled angles
         nalpha=11
         do j=1,nalpha


C          initial sampled angles
           alpha(j)=pi*(j-1)/(nalpha-1)


C          transformation matrix
           T(1,1)=dcos(alpha(j))**2.0d0
           T(2,1)=dsin(alpha(j))**2.0d0
```

```fortran
        T(3,1)=-dcos(alpha(j))*dsin(alpha(j))
        T(1,2)=dsin(alpha(j))**2.0d0
        T(2,2)=dcos(alpha(j))**2.0d0
        T(3,2)=dcos(alpha(j))*dsin(alpha(j))
        T(1,3)=2.0d0*dcos(alpha(j))*dsin(alpha(j))
        T(2,3)=-2.0d0*dcos(alpha(j))*dsin(alpha(j))
        T(3,3)=dcos(alpha(j))**2.0d0-dsin(alpha(j))**2.0d0

C       inverse transformation matrix
        Tinv(1,1)=dcos(alpha(j))**2.0d0
        Tinv(2,1)=dsin(alpha(j))**2.0d0
        Tinv(3,1)=dcos(alpha(j))*dsin(alpha(j))
        Tinv(1,2)=dsin(alpha(j))**2.0d0
        Tinv(2,2)=dcos(alpha(j))**2.0d0
        Tinv(3,2)=-dcos(alpha(j))*dsin(alpha(j))
        Tinv(1,3)=-2.0d0*dcos(alpha(j))*dsin(alpha(j))
        Tinv(2,3)=2.0d0*dcos(alpha(j))*dsin(alpha(j))
        Tinv(3,3)=dcos(alpha(j))**2.0d0-dsin(alpha(j))**2.0d0

C       transform Green strains
        Ep_rot=matmul(T,Ep)

C       transform S
        temp1=matmul(T,Sp)
        Sp_rot=matmul(temp1,Tinv)

C       transform f
        fp_rot=matmul(T,fp)

C       Green strains at uniaxial state
        Ep_u(2)=Sp_rot(2,1)*(Ep_rot(1)+fp_rot(1))/Sp_rot(1,1)
     &    -fp_rot(2)
        Ep_u(3)=Sp_rot(3,1)*(Ep_rot(1)+fp_rot(1))/Sp_rot(1,1)
     &    -fp_rot(3)

C       Green strains for wrinkling angle criteria
```

```
      Ep1_a(j)=Ep_rot(1)

      deltaEp2_a(j)=Ep_u(2)-Ep_rot(2)

      deltaEp3_a(j)=Ep_u(3)-Ep_rot(3)

    end do


C       check shear strain wrinkling angle criterion
      nbeta=0

      do j=1,nalpha-1

        if (abs(deltaEp3_a(j))<=tol) then

          nbeta=nbeta+1

          beta(nbeta)=alpha(j)

          Ep1_b(nbeta)=Ep1_a(j)

          deltaEp2_b(nbeta)=deltaEp2_a(j)

    else if (deltaEp3_a(j)*deltaEp3_a(j+1)<0.0d0) then

    angle_l=alpha(j)

    angle_r=alpha(j+1)

          f_l=deltaEp3_a(j)

          f_r=deltaEp3_a(j+1)

          f_new=1


          nloop=0

          do while (abs(f_new)>tol)


            if (nloop>=100) then

C             write(1,'(a, e20.10)'), 'f_new', f_new

              exit

            end if


            angle_new=(f_r*angle_l-f_l*angle_r)/(f_r-f_l)


C             transformation matrix
            T(1,1)=dcos(angle_new)**2.0d0

            T(2,1)=dsin(angle_new)**2.0d0

            T(3,1)=-dcos(angle_new)*dsin(angle_new)

            T(1,2)=dsin(angle_new)**2.0d0

            T(2,2)=dcos(angle_new)**2.0d0
```

```fortran
            T(3,2)=dcos(angle_new)*dsin(angle_new)
            T(1,3)=2.0d0*dcos(angle_new)*dsin(angle_new)
            T(2,3)=-2.0d0*dcos(angle_new)*dsin(angle_new)
            T(3,3)=dcos(angle_new)**2.0d0-dsin(angle_new)**2.0d0

C           inverse transformation matrix
            Tinv(1,1)=dcos(angle_new)**2.0d0
            Tinv(2,1)=dsin(angle_new)**2.0d0
            Tinv(3,1)=dcos(angle_new)*sin(angle_new)
            Tinv(1,2)=dsin(angle_new)**2.0d0
            Tinv(2,2)=dcos(angle_new)**2.0d0
            Tinv(3,2)=-dcos(angle_new)*dsin(angle_new)
            Tinv(1,3)=-2.0d0*dcos(angle_new)*dsin(angle_new)
            Tinv(2,3)=2.0d0*dcos(angle_new)*dsin(angle_new)
            Tinv(3,3)=dcos(angle_new)**2.0d0-dsin(angle_new)**2.0d0

C           transform Green strains
            Ep_rot=matmul(T,Ep)

C           transform S
            temp1=matmul(T,Sp)
            Sp_rot=matmul(temp1,Tinv)

C           transform f
            fp_rot=matmul(T,fp)

C           Green strains at uniaxial state
            Ep_u(2)=(Sp_rot(2,1)/Sp_rot(1,1))*(Ep_rot(1)+fp_rot(1))
     &        -fp_rot(2)
            Ep_u(3)=(Sp_rot(3,1)/Sp_rot(1,1))*(Ep_rot(1)+fp_rot(1))
     &        -fp_rot(3)

            f_new=Ep_u(3)-Ep_rot(3)

            if (f_new*fl<0.0d0) then
              angle_r=angle_new
```

```
          f_r=f_new
        else if (f_new*fl>0.0d0) then
          angle_l=angle_new
          f_l=f_new
        end if
        nloop=nloop+1
      end do
      nbeta=nbeta+1
      beta(nbeta)=angle_new
      Ep1_b(nbeta)=Ep_rot(1)
      deltaEp2_b(nbeta)=Ep_u(2)-Ep_rot(2)
    end if
  end do


C     check uniaxial and transverse strain wrinkling criteria
      ngamma=0
      do j=1,nbeta
C        write(1,'(a, i2, e20.10)'), 'beta', j, beta(j)
        if (Ep1_b(j)>0.0d0 .and. deltaEp2_b(j)>0.0d0) then
          ngamma=ngamma+1
          gamma(ngamma)=beta(j)
C          write(1,'(a, i2, e20.10)'), 'gamma', ngamma, gamma(ngamma)
        end if
      end do


C     final wrinkling angle
      angle_w=gamma(1)
C      write(1,'(a, e20.10)'), 'angle_w', angle_w


C     transformation matrix
      T(1,1)=dcos(angle_w)**2.0d0
      T(2,1)=dsin(angle_w)**2.0d0
      T(3,1)=-dcos(angle_w)*dsin(angle_w)
      T(1,2)=dsin(angle_w)**2.0d0
      T(2,2)=dcos(angle_w)**2.0d0
      T(3,2)=dcos(angle_w)*dsin(angle_w)
```

```
        T(1,3)=2.0d0*dcos(angle_w)*dsin(angle_w)

        T(2,3)=-2.0d0*dcos(angle_w)*dsin(angle_w)

        T(3,3)=dcos(angle_w)**2.0d0-dsin(angle_w)**2.0d0


C       inverse transformation matrix
        Tinv(1,1)=dcos(angle_w)**2.0d0

        Tinv(2,1)=dsin(angle_w)**2.0d0

        Tinv(3,1)=dcos(angle_w)*dsin(angle_w)

        Tinv(1,2)=dsin(angle_w)**2.0d0

        Tinv(2,2)=dcos(angle_w)**2.0d0

        Tinv(3,2)=-dcos(angle_w)*dsin(angle_w)

        Tinv(1,3)=-2.0d0*dcos(angle_w)*dsin(angle_w)

        Tinv(2,3)=2.0d0*dcos(angle_w)*dsin(angle_w)

        Tinv(3,3)=dcos(angle_w)**2.0d0-dsin(angle_w)**2.0d0


C       Green strains in wrinkling directions
        Ep_w=matmul(T,Ep)


C        write(1,'(e20.10, e20.10, e20.10)'),Ep_w(1),Ep_w(2),Ep_w(3)


C       S at wrinkling directions
        temp1=matmul(T,Sp)
        Sp_w=matmul(temp1,Tinv)


C       f at wrinkling directions
        fp_w=matmul(T,fp)


C       PK2 stresses at wrinkling directions
        PK2p_w(1)=(Ep_w(1)+fp_w(1))/Sp_w(1,1)
        PK2p_w(2)=0.0d0
        PK2p_w(3)=0.0d0


C       corrected PK2 stresses in material directions
        PK2p_c=matmul(Tinv, PK2p_w)
        PK2(1,1)=PK2p_c(1)
        PK2(2,2)=PK2p_c(2)
```

```
      PK2(3,3)=0.0d0
  PK2(1,2)=PK2p_c(3)
  PK2(1,3)=0.0d0
      PK2(2,1)=PK2p_c(3)
      PK2(2,3)=0.0d0
  PK2(3,1)=0.0d0
  PK2(3,2)=0.0d0


C       write(1,'(e20.10, e20.10)'),PK2p_w(1)
C        write(1,'(e20.10, e20.10, e20.10)'),PK2(1,1),PK2(2,2),PK2(1,2)


C       Green strains in wrinkling directions at uniaxial state
      Ep_w(2)=Sp_w(2,1)*PK2p_w(1)-fp_w(2)
      Ep_w(3)=Sp_w(3,1)*PK2p_w(1)-fp_w(3)


C       corrected Green strains in material directions
      Ep_c=matmul(Tinv, Ep_w)
      E(1,1)=Ep_c(1)
      E(2,2)=Ep_c(2)
      E(3,3)=S13*PK2(1,1)-f13+S23*PK2(2,2)-f23
      E(1,2)=Ep_c(3)
      E(1,3)=0.0d0
      E(2,1)=Ep_c(3)
      E(2,3)=0.0d0
      E(3,1)=0.0d0
      E(3,2)=0.0d0


C       right stretch tensor
      Ep(1)=E(1,1)
      Ep(2)=E(2,2)
      Ep(3)=E(1,2)
      Eppr(1)=(Ep(1)+Ep(2))/2.0d0
   &   +dsqrt(((Ep(1)-Ep(2))/2.0d0)**2.0d0+Ep(3)**2.0d0)
      Eppr(2)=(Ep(1)+Ep(2))/2.0d0
   &   -dsqrt(((Ep(1)-Ep(2))/2.0d0)**2.0d0+Ep(3)**2.0d0)
      Uppr(1)=dsqrt(Eppr(1)*2.0d0+1.0d0)
```

```fortran
      Uppr(2)=dsqrt(Eppr(2)*2.0d0+1.0d0)
      detUp=Uppr(1)*Uppr(2)


      if (E(1,2)>=0.0d0) then
        U(1,2)=dsqrt(2.0d0*E(1,2)**2.0d0/(E(1,1)+E(2,2)+1.0d0+detUp))
      endif
      if (E(1,2)<0.0d0) then
        U(1,2)=-dsqrt(2.0d0*E(1,2)**2.0d0/(E(1,1)+E(2,2)+1.0d0+detUp))
      endif
      U(1,1)=dsqrt(2.0d0*E(1,1)+1.0d0-U(1,2)**2.0d0)
      U(2,2)=dsqrt(2.0d0*E(2,2)+1.0d0-U(1,2)**2.0d0)
      U(3,3)=dsqrt(E(3,3)*2.0d0+1.0d0)
      U(1,3)=0.0d0
      U(2,1)=U(1,2)
      U(2,3)=0.0d0
      U(3,1)=0.0d0
      U(3,2)=0.0d0
      UT=transpose(U)
      detU=detUp*U(3,3)


C     material volumetric strain
      theta=detU-1


    endif


C----------taut element-------------C


    if (state==3) then


C     write(1,'(a)'), 'taut'


C     PK2 stresses
      detS=S11*S22-S12*S12
      PK2(1,1)=(S22*(E(1,1)+f11+f21)
   &    -S12*(E(2,2)+f12+f22))/detS
      PK2(2,2)=(-S12*(E(1,1)+f11+f21)
```

```fortran
     &    +S11*(E(2,2)+f12+f22))/detS
          PK2(3,3)=0.0d0
    PK2(1,2)=(E(1,2)+f66)/S66
    PK2(1,3)=0.0d0
    PK2(2,1)=(E(1,2)+f66)/S66
    PK2(2,3)=0.0d0
    PK2(3,1)=0.0d0
    PK2(3,2)=0.0d0


C        Green strains
         E(3,3)=S13*PK2(1,1)-f13+S23*PK2(2,2)-f23


C        right stretch tensor
         U(3,3)=dsqrt(E(3,3)*2.0d0+1.0d0)
         UT=transpose(U)
         detU=(U(1,1)*U(2,2)-U(1,2)*U(2,1))*U(3,3)


C        material volumetric strain at the end of increment
         theta=detU-1


      endif


C----------update stress--------------C


C     convert PK2 to Cauchy
      temp1=matmul(U,PK2)
      temp2=matmul(temp1,UT)
      sigma=temp2/detU

      stressNew(km,1) = sigma(1,1)
      stressNew(km,2) = sigma(2,2)
      stressNew(km,3) = sigma(3,3)
      stressNew(km,4) = sigma(1,2)


C-----update solution-dependent variables-----C
```

```fortran
C     update PK2 stresses at the end of increment
      stateNew(km,1) = PK2(1,1)
      stateNew(km,2) = PK2(2,2)
      stateNew(km,3) = PK2(1,2)


C     update hereditary integrals at the end of increment
      counter = 4
      do j = 1, nProny
        stateNew(km,counter)=dexp(-dtr/tauj(j))*q11old(j)
     & +(PK2(1,1)-PK2pold(1))*(1.0d0-dexp(-dtr/tauj(j)))/(dtr/tauj(j))
        stateNew(km,counter+nProny)=dexp(-dtr/tauj(j))*q12old(j)
     & +(PK2(1,1)-PK2pold(1))*(1.0d0-dexp(-dtr/tauj(j)))/(dtr/tauj(j))
        stateNew(km,counter+2*nProny)=dexp(-dtr/tauj(j))*q13old(j)
     & +(PK2(1,1)-PK2pold(1))*(1.0d0-dexp(-dtr/tauj(j)))/(dtr/tauj(j))
        stateNew(km,counter+3*nProny)=dexp(-dtr/tauj(j))*q21old(j)
     & +(PK2(2,2)-PK2pold(2))*(1.0d0-dexp(-dtr/tauj(j)))/(dtr/tauj(j))
        stateNew(km,counter+4*nProny)=dexp(-dtr/tauj(j))*q22old(j)
     & +(PK2(2,2)-PK2pold(2))*(1.0d0-dexp(-dtr/tauj(j)))/(dtr/tauj(j))
        stateNew(km,counter+5*nProny)=dexp(-dtr/tauj(j))*q23old(j)
     & +(PK2(2,2)-PK2pold(2))*(1.0d0-dexp(-dtr/tauj(j)))/(dtr/tauj(j))
        stateNew(km,counter+6*nProny)=dexp(-dtr/tauj(j))*q66old(j)
     & +(PK2(1,2)-PK2pold(3))*(1.0d0-dexp(-dtr/tauj(j)))/(dtr/tauj(j))
        counter=counter+1
       end do


C     update Green strain at the end of increment
      stateNew(km,109)= E(1,1)
      stateNew(km,110)= E(2,2)
      stateNew(km,111)= E(3,3)
      stateNew(km,112)= E(1,2)


C     update volumetric strain at the end of increment
      stateNew(km,113)=theta


C     update volumetric strain at the end of previous increment
      stateNew(km,114)= thetaold
```

```fortran
C     update volumetric strain used for shift factor
      stateNew(km,115)= thetashift


C     update shift factor at the beginning of increment
      stateNew(km,116)= aTtheta


C----------update energy----------C


C     update internal energy
      enerInternNew(km)=0.0d0


C     update dissipated inelastic energy
      enerInelasNew(km)=0.0d0


      end do


      end if


      return
      end
C**********************************************************************
```